THE ASTROPHYSICAL JOURNAL SUPPLEMENT SERIES, 99:67–106, 1995 July

STELLAR AND GASEOUS KINEMATICS OF SEYFERT GALAXIES. I. SPECTROSCOPIC DATA

CHARLES H. NELSON[1,2] AND MARK WHITTLE[2,3,4]
Astronomy Department, University of Virginia, Box 3818, University Station, Charlottesville, VA 22903
Received 1993 November 3; accepted 1994 December 13

ABSTRACT

In order to study the relationship between the gravitational potential and the properties of active galaxies, we have measured nuclear stellar and gaseous kinematics for a large sample of Seyfert galaxies. In this paper we present moderate-resolution data (80–230 km s^{-1} FWHM) from two spectral regions, one in the near-infrared containing the Ca II triplet absorption features at ~8550 Å and the [S III] 9069 Å emission line, and the other in the visual including the Mg *b* absorption lines at ~5175 Å and the [O III] 5007 Å emission line. Nuclear stellar velocities, V_*, and velocity dispersions, σ_*, were measured using the cross-correlation method. Complications for the kinematic analysis associated with the featureless continua and strong emission lines in Seyfert galaxies are briefly discussed. Emission-line velocities and widths were also measured from our spectra. The final sample contains 85 objects (22 type 1 Seyfert galaxies, 51 type 2 Seyferts, nine LINERs, and three normal galaxies). We provide a supplement to the database of narrow-line region and host galaxy properties compiled by Whittle (1992a) for 20 Seyfert galaxies not originally included. We plan to use our measurements in conjunction with this database to investigate the relationship between the nuclear gravitational potential and other properties of Seyfert galaxies.

Subject headings: galaxies: kinematics and dynamics — galaxies: Seyfert

1. INTRODUCTION

One of the remarkable facts about the occurrence of activity in galaxies is its location: always at the center of the galaxy. The reason for this preferred location, of course, is the presence of a deep gravitational potential well. Whether we consider the standard black hole scenario or a starburst scenario, the presence of the potential well plays a crucial role in the onset, evolution, and manifestation of activity. Relaxation within the potential causes both gas and stars to settle inward, first forming, then feeding an active nucleus. Furthermore, the energetic particles and radiation released from the active center emerge to encounter gas whose properties may also depend on its location in a deep potential. Thus, it would seem that to gain a clear understanding of the phenomenon of activity in galaxies, it is important to study nuclear potentials. Our aim is to provide such a study for Seyfert galaxies.

Most previous studies of active galaxies have focused on the active properties, rather than the properties of the host galaxy, and have provided a relatively clear picture of several nested regions spanning a wide range of length scales. On the smallest scales, $\sim 10^{-4}$ to 10^{-5} pc, energy is released as gas accretes through the potential of a massive black hole. On scales ~0.1–1 pc the nuclear radiation field ionizes high-density clouds which move through the broad-line region (BLR) at speeds $\sim 10^4$ km s^{-1}, while farther out, on scales ~10–10^3 pc, lower density ionized clouds in the narrow-line region (NLR) travel at speeds $\sim 10^2$–10^3 km s^{-1}. In addition to this line-emitting component, there can also be a radio synchrotron-emitting component of relativistic particles and magnetic fields, spanning a similar range in length scales, from subparsec to kiloparsec, often including a jetlike component.

Despite a relatively detailed understanding of these "active" components, there is still very little known about the form of the gravitational potential in which they all reside. For example, although in principle the innermost potential might be probed using emission from the central accretion disk, in practice the observational signatures of such an accretion disk are not well understood. Indeed, even their existence has yet to be demonstrated conclusively. Extracting the subparsec potential from the BLR velocity field is more promising, but it is still unclear whether gravity or other forces, such as radiation or wind pressure, dominate the cloud motion in this region. Even at the resolution of the *Hubble Space Telescope,* the light from stars on BLR scales is too faint to use as an effective tracer of gravitational velocities. To measure the nuclear potential with any certainty, one must look to much larger scales, ~10–10^3 pc, and use components which are known to be gravitationally supported. Although measurements on this scale lie far outside the innermost regions, they are nevertheless well matched to the scale of the NLR. A natural first study, therefore, is to look for the relationship between the properties of the kiloparsec-scale gravitational field and the properties of the NLR and its associated radio source. If the nuclear potential acts as a coherent whole, it may also be possible to find links between the kiloparsec-scale potential and properties of nuclear activity and the nuclear potential on much smaller scales.

[1] Current address: Space Telescope Science Institute, 3700 San Martin Drive, Baltimore, MD 21218.
[2] Visiting Astronomer, Kitt Peak National Observatory. KPNO is operated by AURA, Inc., under cooperative agreement with the National Science Foundation.
[3] Visiting Astronomer, Anglo-Australian Observatory, Epping, NSW, Australia.
[4] Visiting Astronomer, Rocque de Los Muchachos Observatory, La Palma, Spain.

There are a number of ways to measure the near-nuclear gravitational field in galaxies. Direct probes include rotation and dispersion velocities of stars and some gaseous components, while indirect probes include stellar luminosity distributions and more global galaxy kinematics. Whittle (1992a, b, c, hereafter W92a, W92b, W92c) compiled and studied the indirect nuclear gravitational parameters of galaxy rotation amplitude, $\Delta V_{\rm rot}$, and galaxy bulge magnitude, $M_{\rm bul}$, for a sample of 140 Seyfert galaxies. In fact, these indirect gravitational parameters were found to correlate quite well with kiloparsec-scale radio luminosity and NLR emission-line width, confirming the importance of the nuclear potential in understanding the properties of the NLR. Clearly, it is important to extend this type of study to include more direct measurements of the gravitational field. Such measurements allow two lines of study. First, they allow a cleaner investigation of the relation between properties of nuclear activity and the depth of the nuclear potential. Second, by combining the direct and indirect gravitational parameters, it is possible to compare the dynamical properties of Seyfert galaxies with those of normal galaxies—for example, to search for evidence that the Seyferts have been put together differently from normal galaxies.

In this paper we present new measurements of stellar velocity dispersion for a large sample of Seyfert galaxy nuclei. In a companion paper we use these data to explore (1) the gravitational component of the NLR velocity field, (2) similarities and differences between Seyfert and normal galaxy bulge kinematics, and (3) links between the bulge potential and other aspects of nuclear activity. Our data comprise spectroscopic observations in two wavelength regions, one centered on the Ca II triplet absorption lines at ~8600 Å, and the other centered on the Mg *b* absorption lines at ~5200 Å. These wavelength ranges also include the two important emission lines [S III] λ9069 and [O III] λ5007, and so we provide profile measurements for these lines. Since our subsequent analysis makes use of the database of host galaxy and NLR properties presented in W92a, we provide additions to this database for those new Seyferts not in the original sample but for which we now have stellar and gaseous velocity measurements.

The rest of the paper is organized in the following manner. In § 2 the sample selection is discussed. We describe the observations and spectroscopic reductions in § 3. In § 4 we present spectra of the stellar absorption features and discuss measurement of the velocity dispersions using the cross-correlation method. In § 5 we describe the emission-line profiles and present measurements of the profile parameters. Redshifts of both stars and gas are presented in § 6. The supplement to the W92a compilation is presented in § 7, and the general properties of the sample are discussed in § 8.

2. SAMPLE SELECTION

In trying to study absorption lines in active galaxies, one is faced with the problem that in many cases these absorption lines are either weak or corrupted by emission from the active nucleus, making their measurement very difficult. It is not practical, therefore, to obtain stellar kinematic measurements for a sample that is complete in the usual sense. We have instead chosen a more pragmatic approach. Our strategy has been to select active galaxies which span as wide a range of properties as possible, while maximizing the chance that a reliable value for the stellar kinematics can be obtained. We have drawn heavily on the sample of 140 Seyfert galaxies in W92a, since their kinematic, active, and host galaxy properties have already been investigated in some detail (W92b, W92c). To expand this sample, however, we have included additional galaxies from the lists of Véron-Cetty & Véron (1987) and Kaneko (1986). Wherever possible, we looked at low-dispersion spectra to guide selection (e.g., the spectral plots of Morris & Ward 1988 were very helpful in assessing the Ca II triplet region). Characteristics which weighed against selection include the invisibility of Mg *b* and Ca II triplet features, the Ca II triplet in emission, strong Fe II in emission (which not only confuses Mg *b* but is also correlated with Ca II triplet in emission), and a host galaxy which is fainter than about 15 mag in the *B* band (see § 3 for further discussion of these problems). Usually, objects were considered for observation unless both spectral regions were known to be highly problematic. Finally, we observed a small number of normal galaxies with previously measured velocity dispersions (to test our methods), and added three Seyferts with published velocity dispersions which we did not observe ourselves (NGC 1566, NGC 1667, and NGC 3516).

The final sample of 85 objects includes 22 type 1 Seyfert galaxies, 51 type 2 Seyferts, nine LINERs, and three normal galaxies; of these, 78 have usable stellar velocity dispersion measurements. The sample is similar to that in W92a (51 objects in common), but with somewhat lower mean redshift, brighter apparent magnitude distribution, and a smaller fraction of type 1 Seyfert galaxies. Section 8 describes the sample properties in more detail.

As with the W92a sample, our stellar dispersion sample is not complete in any well defined sense. It is, however, a representative sample, lacking only the more luminous type 1 Seyfert galaxies. It contains active galaxies with a wide range of both active and host properties, allowing investigation of the relationship between these properties and the nuclear stellar kinematics. More important for a dynamical study, the selection of galaxies has not explicitly considered emission- or absorption-line *width*. Nevertheless, indirect effects may still bias the sample somewhat. For example, selection of nearby galaxies may favor those of lower luminosity and hence narrower lines. Although these selection effects will not severely undermine studies of correlations between sample properties, one should nevertheless be cautious when considering or comparing distributions of sample properties.

3. OBSERVATIONS AND REDUCTION

We present data taken from three observatories (see Table 1). The Image Photon Counting System (IPCS; Boksenberg et al. 1975) was used with the 25 cm camera of the Royal Greenwich Observatory spectrograph on the 3.9 m Anglo-Australian Telescope (AAT; three nights); a GEC CCD was used with the 23.5 cm camera of the Intermediate Dispersion Spectrograph on the 2.5 m Isaac Newton Telescope in La Palma (INT; four nights); TI and FORD CCDs were used with the Goldcam spectrograph of the 2.1 m telescope at Kitt Peak (13 nights). Spectral resolutions vary for the different observing runs, but all lie in the range 80–230 km s^{-1} (FWHM), which is adequate for basic stellar and gaseous kinematic work.

We chose to work with two spectral regions, each containing

TABLE 1

SPECTROSCOPIC OBSERVATIONS

Run	Dates	Telescope Spectrograph	Detector Format	Spectral Range Å	Grating/ Order 1 mm^{-1}	Dispersion Å pix^{-1}	Resolution (FWHM) km s^{-1}	Spatial Scale " pix^{-1}
1	9/29/84 – 10/1/84	AAT 3.9 m	IPCS	4700 – 5700	1200 I	0.48	80	1.2
		RGO 35 cm	1066 × 36					
2	2/21/86 – 2/24/86	INT 2.5 m	GEC CCD	8265 – 9160	600 I	1.55	123	0.69
		IDS 23.5 cm	400 × 580					
3	9/6/90 – 9/10/90	KPNO 2.1 m	TI CCD	8370 – 9420	600 I	1.29	156	0.78
		Goldcam	512 × 800	4670 – 5700	600 I	1.29	173	
4	3/24/91 – 3/27/91	KPNO 2.1 m	TI CCD	4675 – 5700	600 I	1.29	173	0.78
		Goldcam	512 × 800					
5	5/1/92 – 5/4/92	KPNO 2.1 m	Ford CCD	8370 – 9420	600 I	1.29	156	0.78
		Goldcam	1024 × 2048	4670 – 5700	600 I	1.29	230	0.78

strong stellar absorption and gaseous emission features. The visual spectral region (~4700–5700 Å) contains the magnesium *b* triplet at 5167.5, 5172.7, and 5183.6 Å and the Fe I blends at 5269.6 and 5326.6 Å, as well as the strong emission lines Hβ λ4861.3 and [O III] $\lambda\lambda$4958.9 and 5006.9. Figure 1*a* shows a sample spectrum in the Mg *b* region for the Seyfert 1.5 galaxy NGC 3786. Several features can complicate the kinematic analysis and were carefully monitored. The strong [O III] and narrow Hβ were simply cut, as was the [N I] doublet at 5197.4 + 5200.4 Å which lies just to the red of the Mg *b* triplet. In the few cases in which the [N I] lines are unusually broad (e.g., Mrk 78) we subtracted a scaled and shifted [O III] λ5007 profile. In some type 1 Seyferts the permitted Fe II blends at ~5190 and ~5320 Å can introduce considerable irregularity near the Mg *b* triplet. However, since the blend features are usually quite smooth (originating in the BLR), careful continuum fitting and low-frequency filtering (see § 4.3) can usually remove them quite effectively. The [Fe VII] and [Fe VI] lines at 5158.3, and 5177.0 Å, found in some high-ionization Seyfert 1 and Seyfert 2 galaxies (e.g., Malkan & Filippenko 1983) are a more serious contamination problem. These fall in the midst of the Mg *b* triplet and, if strong, can thoroughly confuse the kinematic analysis. These lines appeared in only a few of our spectra, and we were able to recover the stellar kinematics of these objects (NGC 4051, NGC 3227, NGC 4593) using the Ca II triplet.

The near-infrared spectral region (~8300–9400 Å) contains the Ca II triplet absorption features at 8498.0, 8542.1, and 8662.1 Å, as well as the permitted O I 8446.4 Å and forbidden [S III] 9068.9 Å emission lines. The lines [S III] λ9069 and [O III] λ4959 have similar ionization potential and critical density, and so we expect them to have similar emission distributions within the NLR and hence similar line profiles. Figure 1*b* shows a sample spectrum of the Ca II triplet region for the Seyfert type 1.5 galaxy NGC 4051.

As with the visual spectral region, a number of potential problems can complicate the kinematic analysis. For example, the Ca II triplet features can actually appear in emission. Since the Ca II emission strength correlates with the optical Fe II emission strength (Persson 1988), we tried to avoid observing Seyferts with strong optical Fe II in the Ca II triplet spectral region. In only two objects (Mrk 6, and NGC 4051) was the Ca II triplet clearly seen in emission. Another difficulty with the Ca II triplet spectral region is the numerous OH emission lines which require careful sky subtraction (Fig. 2 shows the KPNO night-sky spectrum). In addition, the strong atmospheric absorption bands above 8900 Å complicate the measurement of the Ca II triplet in galaxies with redshifts greater than ~8000 km s^{-1}. Between 9175 and 9265 Å the atmospheric absorption is noticeably smoother and provides a window for the [S III] line for galaxies with redshifts in the range 3500–6500 km s^{-1}. The [Fe II] λ8617 emission feature lies between the Ca II triplet lines and is quite strong in a number of objects (e.g., Mrk 3, Mrk 1, NGC 4151), making continuum placement quite difficult, particularly if broad O I λ8446 is also present. Finally, the higher members of the Paschen series are a potential concern, since Pa13, Pa15, and Pa16 lie in the cores of the three Ca II triplet lines. Usually their importance can be assessed from the visibility of Pa12 and Pa14, which lie in a cleaner part of the spectrum. Fortunately, only one galaxy, NGC 3227, seemed to show Paschen lines, and the identification was in any case uncertain.

Although the AAT and INT observations were restricted to the Mg *b* and Ca II triplet regions, respectively, for the KPNO observations the most suitable spectral region was chosen for each object, based on the potential problems outlined above. Additional considerations were the difference in velocity resolution (favoring the Ca II triplet region for lower luminosity galaxies with low expected dispersions), the difference in CCD efficiencies (favoring the Mg *b* region for the fainter galaxies), and the influence of power-law dilution and/or a young stellar population (favoring the Ca II triplet region, which is affected less than the Mg *b* region). This last preference for the Ca II triplet region in active galactic nuclei (AGNs) was first stressed by Dressler (1984) using spectra of NGC 1068, in which the absorption lines in the visual are washed out but the Ca II triplet lines are quite strong. Our experience shows, however, that the problem is not as severe as expected, and that for many Seyfert galaxies the Mg *b* lines are still sufficiently strong for kinematic work.

In addition to the galaxy observations, spectra were obtained of velocity template stars for use in the kinematic analysis. These were primarily K giants for the near-infrared spectra, and G0–K5 giants for the visual spectra, providing sufficient range to help match the galaxy spectral type. Short exposures of bright stars near each galaxy were also obtained, giving a direct record of the spatial profile (seeing/telescope focus/instrument). This was particularly important for the KPNO

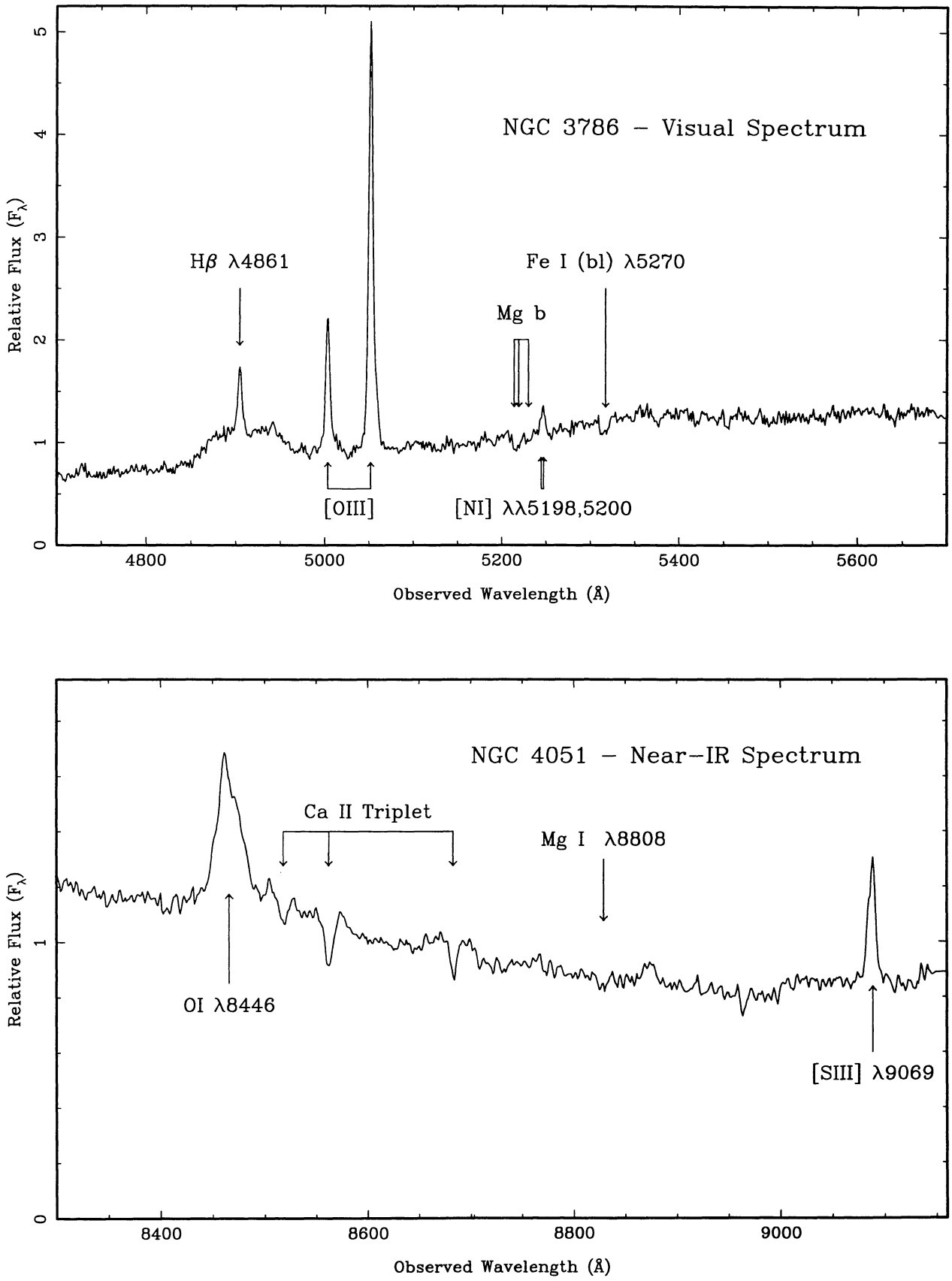

FIG. 1.—Spectra of NGC 3786 in the visual (*top*) and NGC 4051 in the near-infrared (*bottom*) are displayed as examples. Emission and absorption features are indicated, and the spectra are plotted as relative flux per unit wavelength.

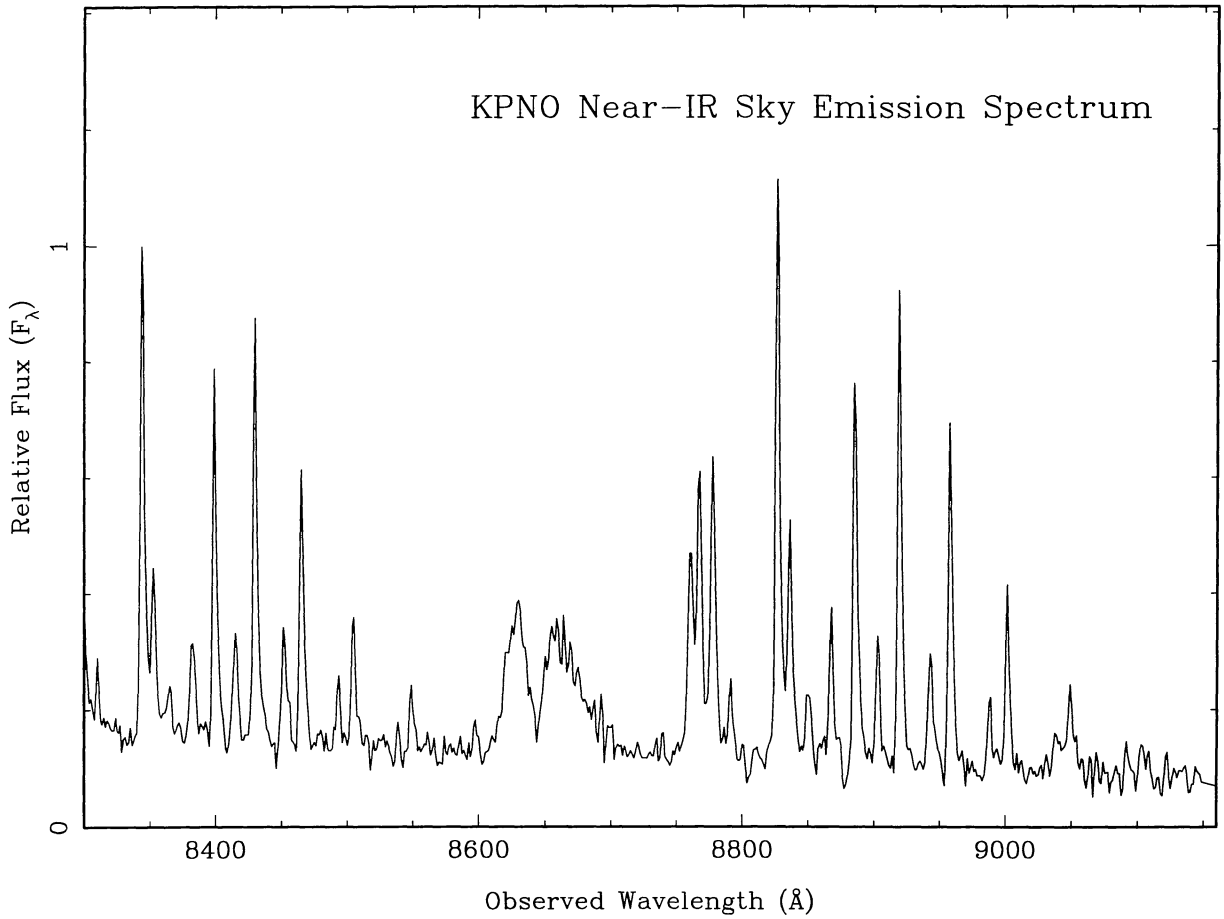

FIG. 2.—Night-sky emission lines in the near-infrared are plotted as relative flux per unit wavelength. Most lines are rotation-vibration bands of the OH molecule. The broad band between 8600 and 8700 Å is due to O_2.

2.1 m observations, since the spectrograph is somewhat astigmatic and the telescope focus was unstable. To help remove the strong atmospheric absorption bands in the near-infrared, exposures of featureless stars were obtained at a range of air masses; some of these were also used as flux standards. Because wavelength integrity is important, He/Ne/Ar calibration exposures were taken before and after each observation.

The AAT data were reduced using SPICA on the Starlink VAX at Cambridge, and the INT and KPNO data were reduced using IRAF on the Suns at Virginia. Initial data reduction followed standard practice, including bias subtraction (for the CCD data), flat-fielding, correction for slit response (INT and KPNO data only), sky subtraction, and wavelength calibration. Typical wavelength fits used 15–20 lines in the visual and 10–15 lines in the near-infrared, giving rms residuals ~0.1 pixel and ~0.2 pixel, respectively, using third- to fifth-order polynomials. These fits were done at 20–30 locations along the slit. In two objects (NGC 2273 and NGC 4941) the [S III] λ9069 line was located sufficiently close to the edge of the chip that a reliable wavelength scale could not be defined.

The atmospheric absorption features were removed from the near-infrared spectra by dividing by the scaled spectrum of a star whose only features were atmospheric. In most cases this proved to be a satisfactory technique, though perhaps not perfect. For a few objects (e.g., NGC 513, NGC 3031, Akn 79), the reconstructed [S III] λ9069 profiles could not be considered reliable, although plots of the profiles appear in Figure 9.

An additional complication in the INT data became apparent during sky subtraction; the extended sky lines were shifted by ~0.4 pixels (~0.6 Å, ~20 km s^{-1}) with respect to those over the galaxy. Despite the use of significant preflash, this effect is caused by residual charge transfer inefficiency during readout of the GEC CCD along the spectral direction. To correct for this, a rough correlation was found between the number of counts per pixel and the amount of shift. For each data frame, the counts per pixel near the Ca II triplet feature defined a series of shifts which were applied to bring the entire frame onto a common wavelength scale. The subsequent sky subtraction was noticeably improved, and the good agreement between the INT and KPNO velocities suggests that this correction method was effective, at least for the Ca II triplet lines.

Specific problems encountered with particular objects, similar to those described above, are noted in the Appendix.

4. ANALYSIS OF STELLAR KINEMATICS

4.1. *Absorption-Line Spectra*

In Figure 3 we display portions of the reduced spectra near the Ca II triplet and Mg *b* features. Each spectrum has been corrected to its rest frame and is plotted as normalized flux per

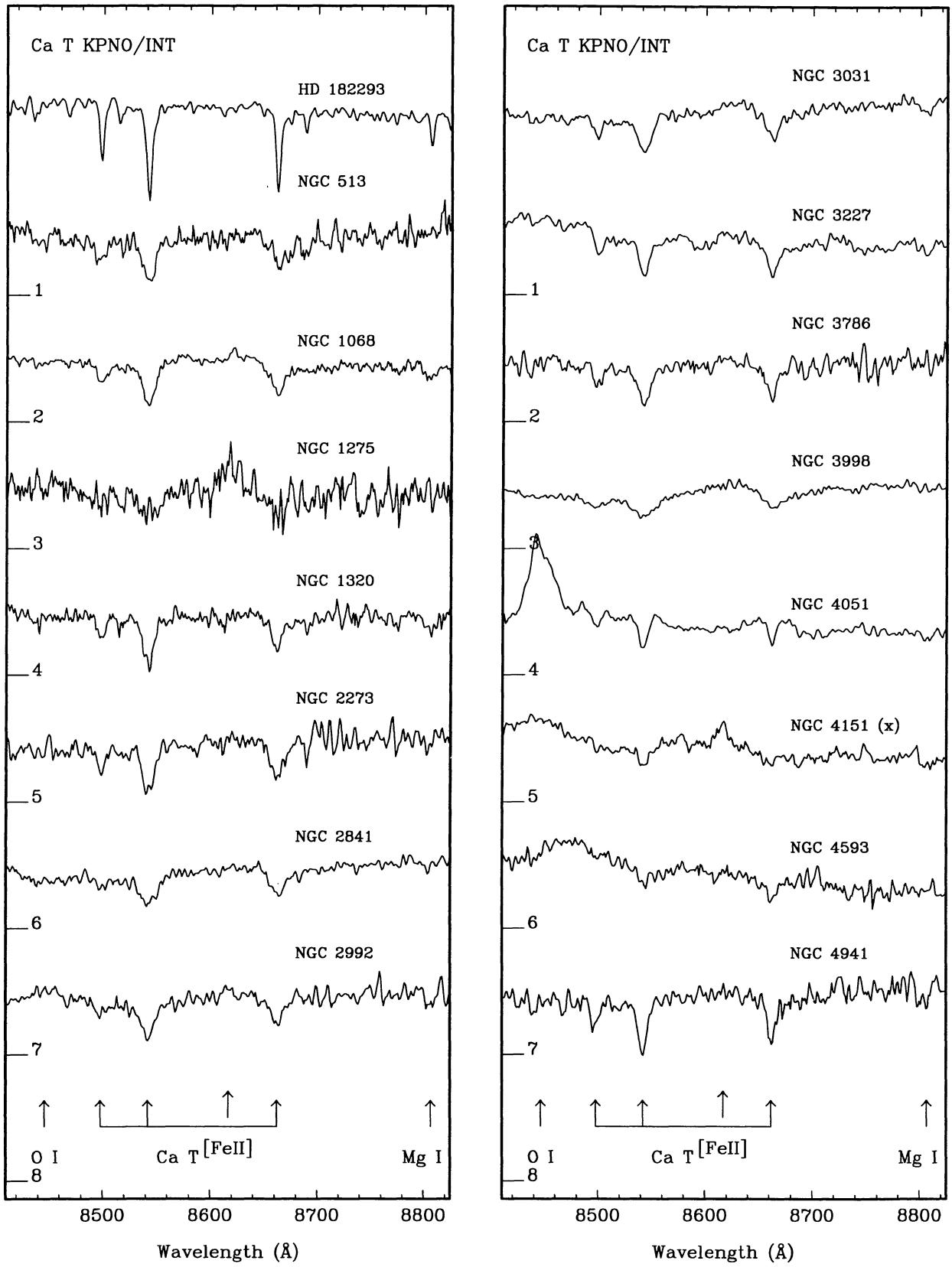

FIG. 3a

FIG. 3.—Absorption-line spectra are presented (*a*) in the near-infrared and (*b*) in the visual. To allow comparison of the width and strength of the stellar features, all spectra are de-redshifted and are plotted as relative flux per unit wavelength with the zero point for each object marked on the left-hand side of each panel. The wavelengths of the most prominent features are indicated at the bottom. Stellar template spectra are included as the first object in each spectral range to show the intrinsic width and instrumental resolution. The AAT spectra are displayed separately, since the resolution was higher on this observing run.

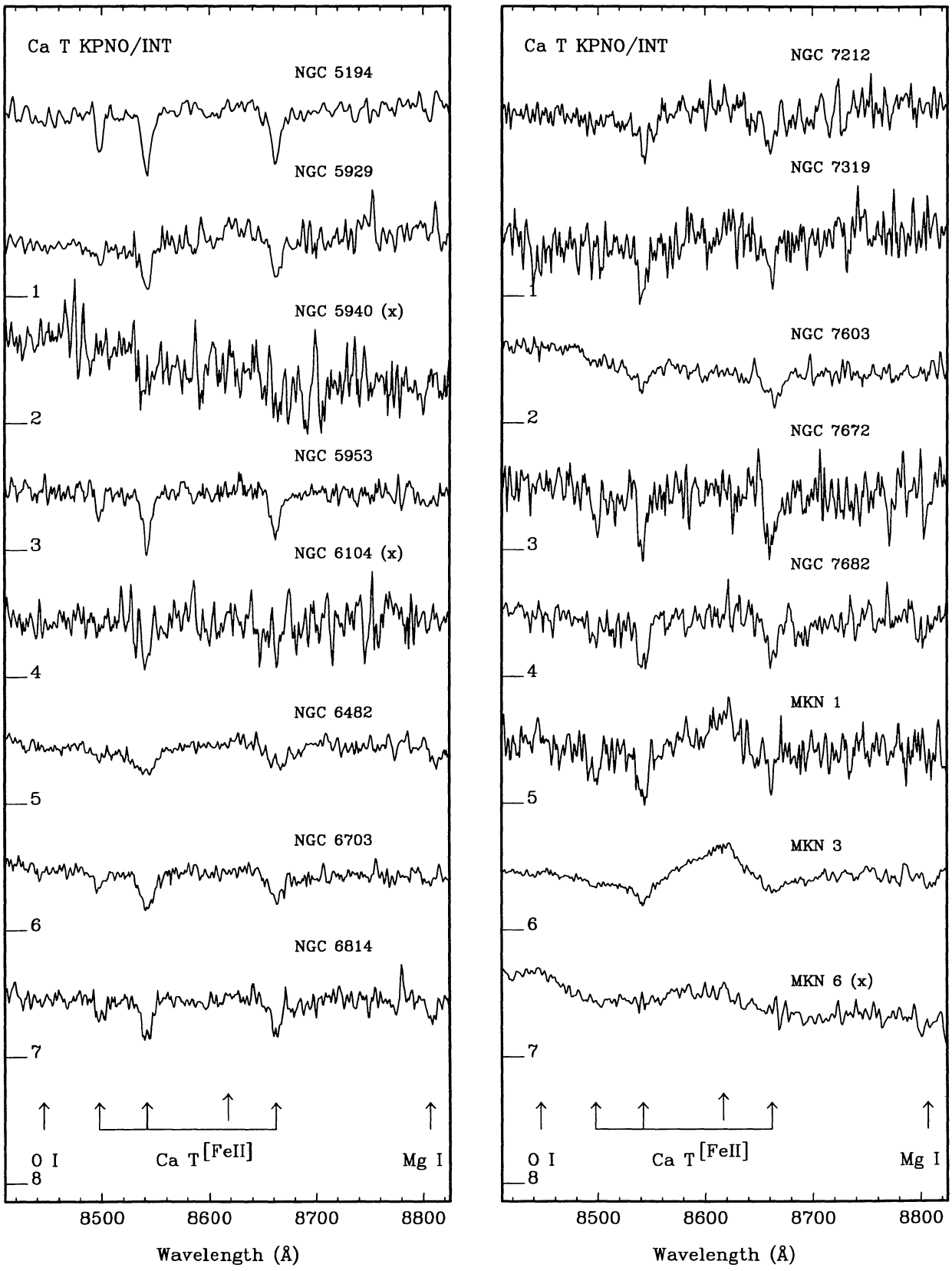

FIG. 3*a*—*Continued*

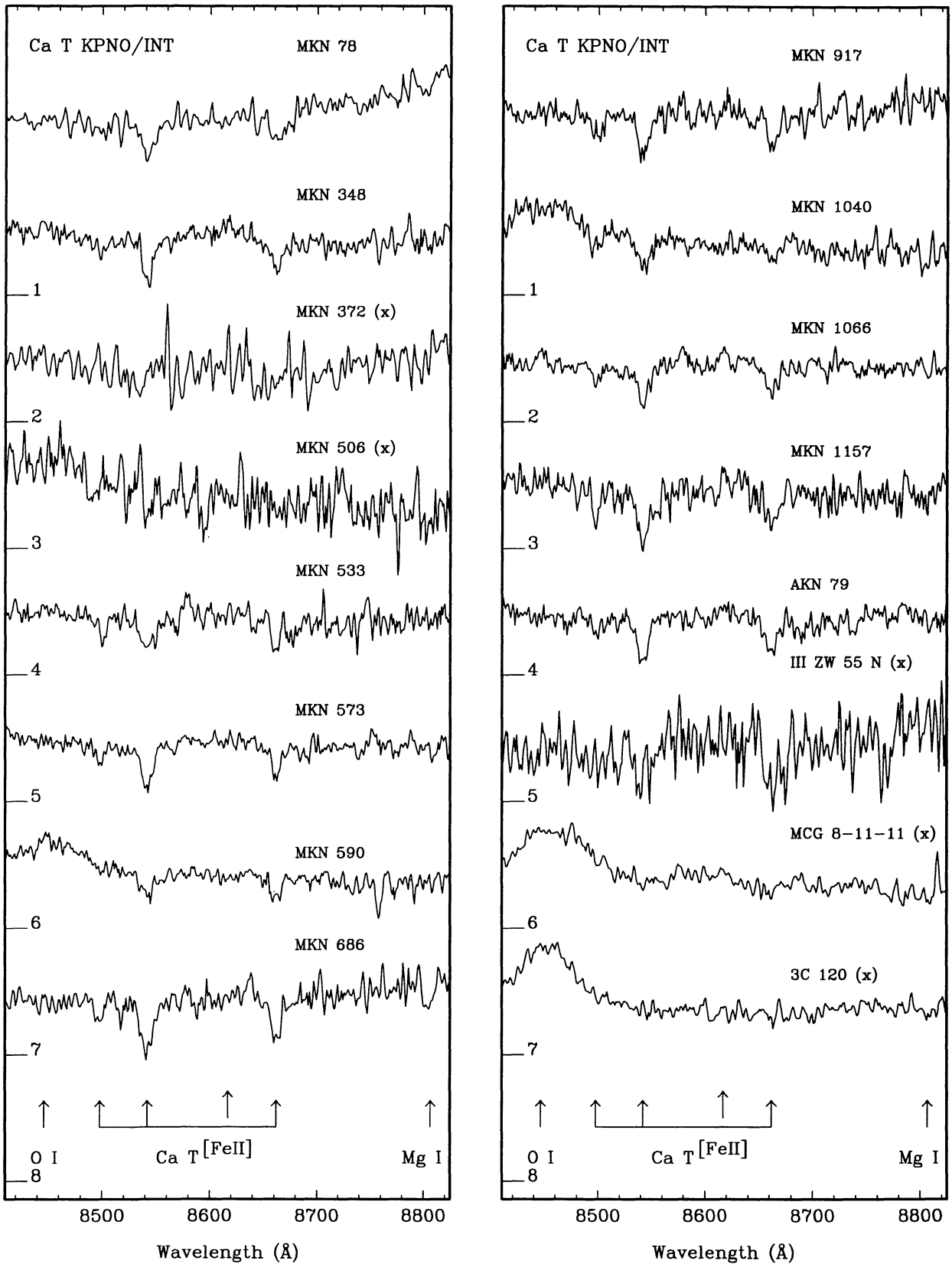

FIG. 3*a*—*Continued*

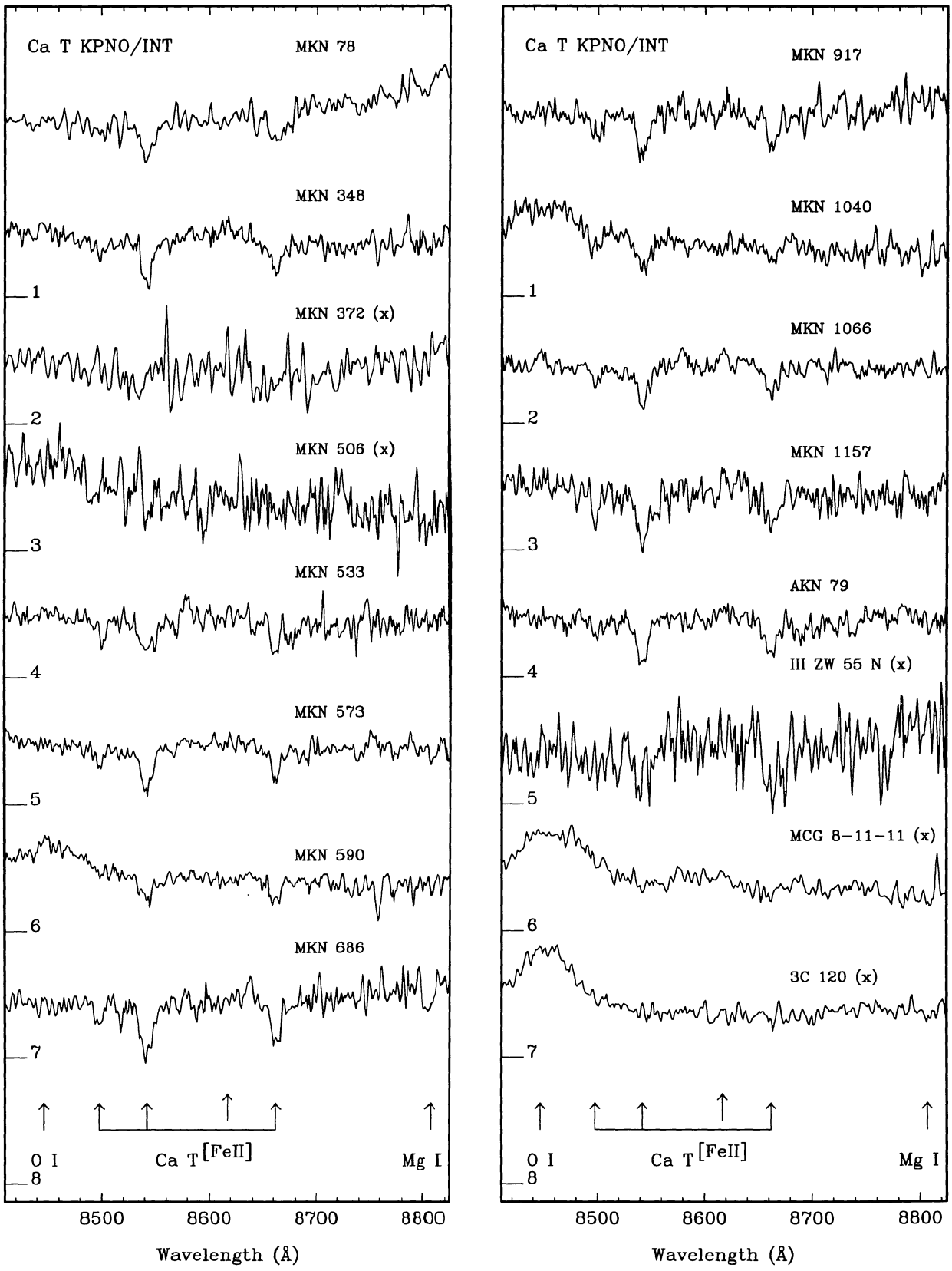

FIG. 3*a*—*Continued*

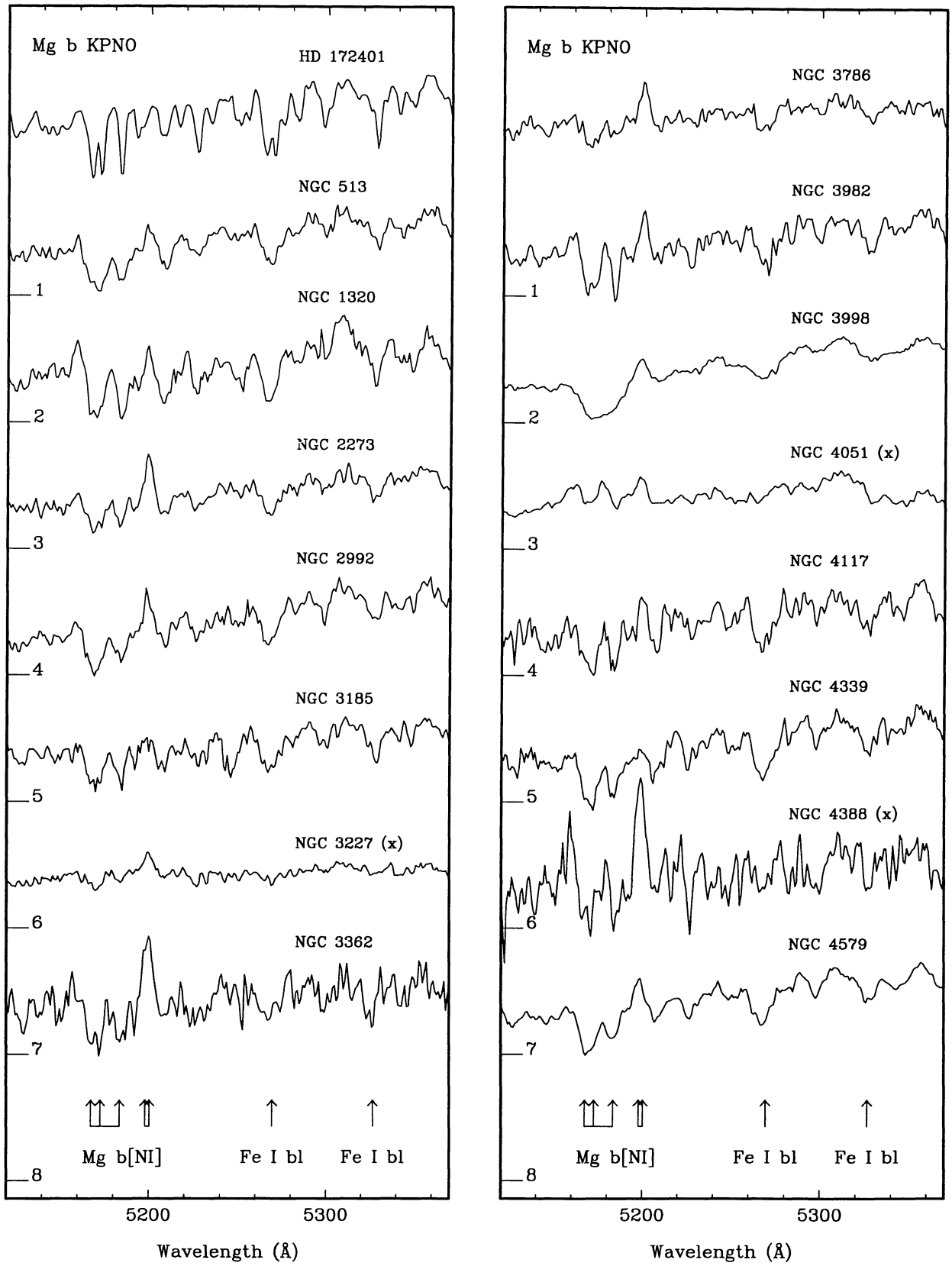

FIG. 3*b*

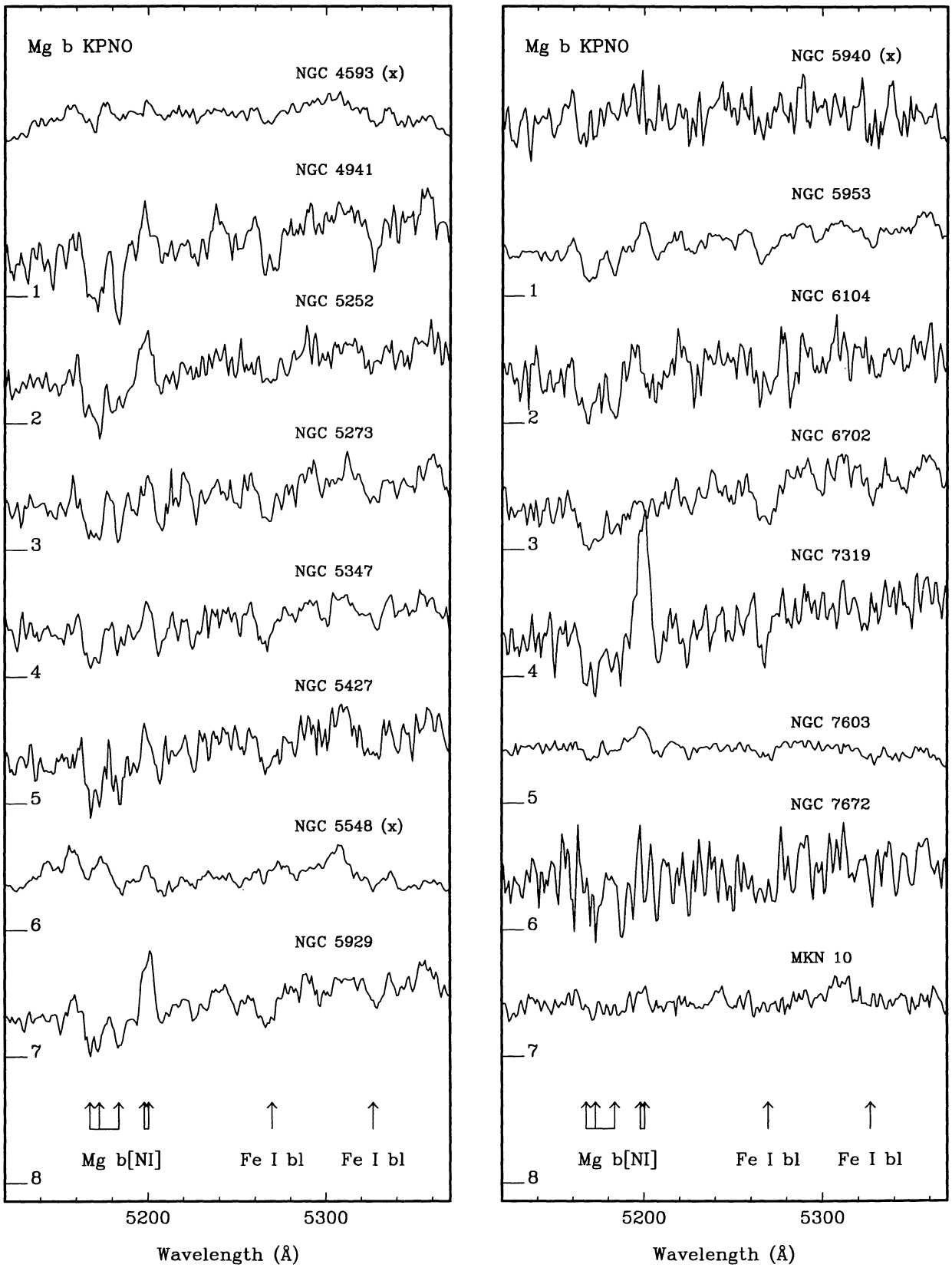

FIG. 3*b*—*Continued*

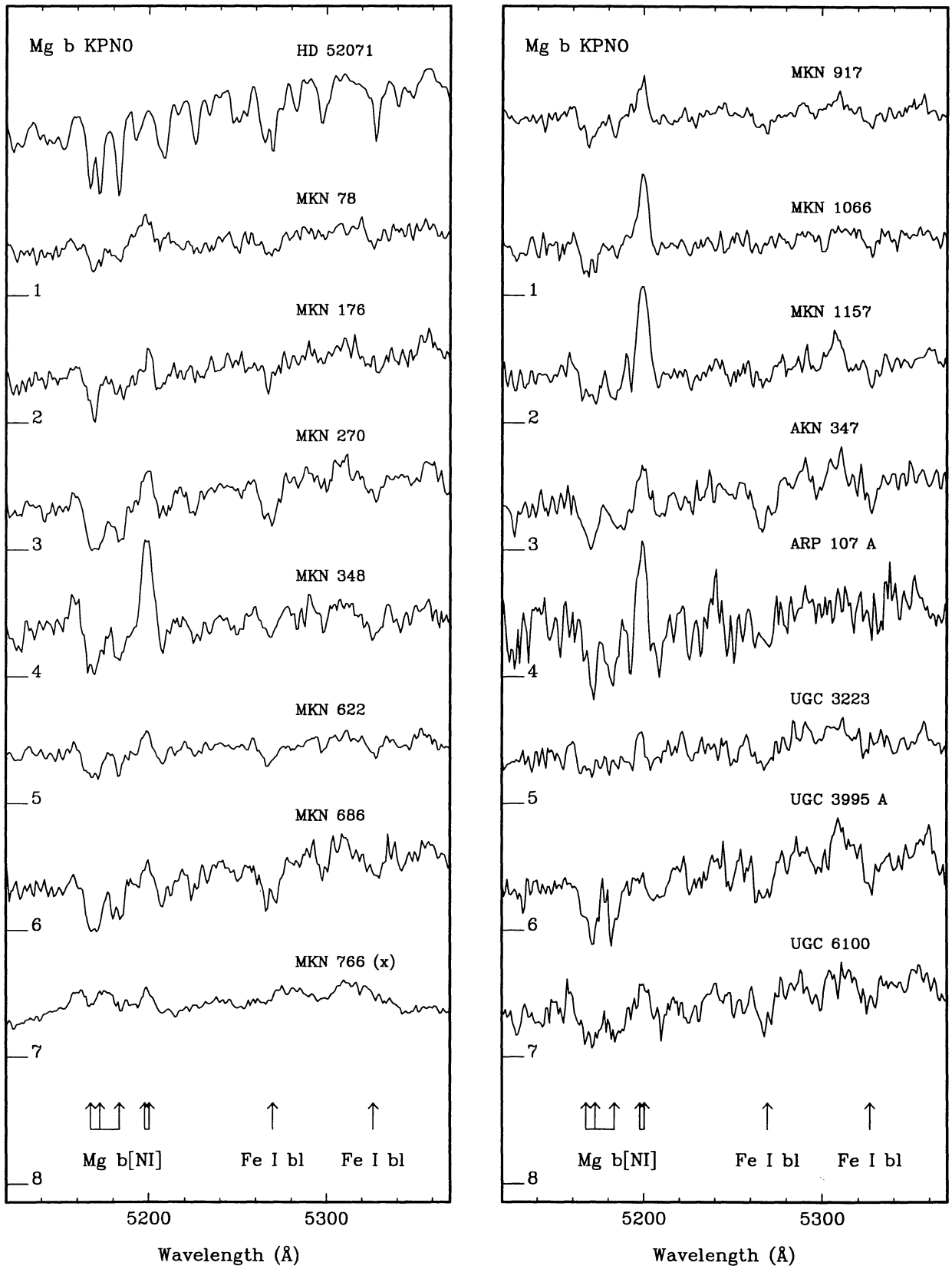

FIG. 3*b*—*Continued*

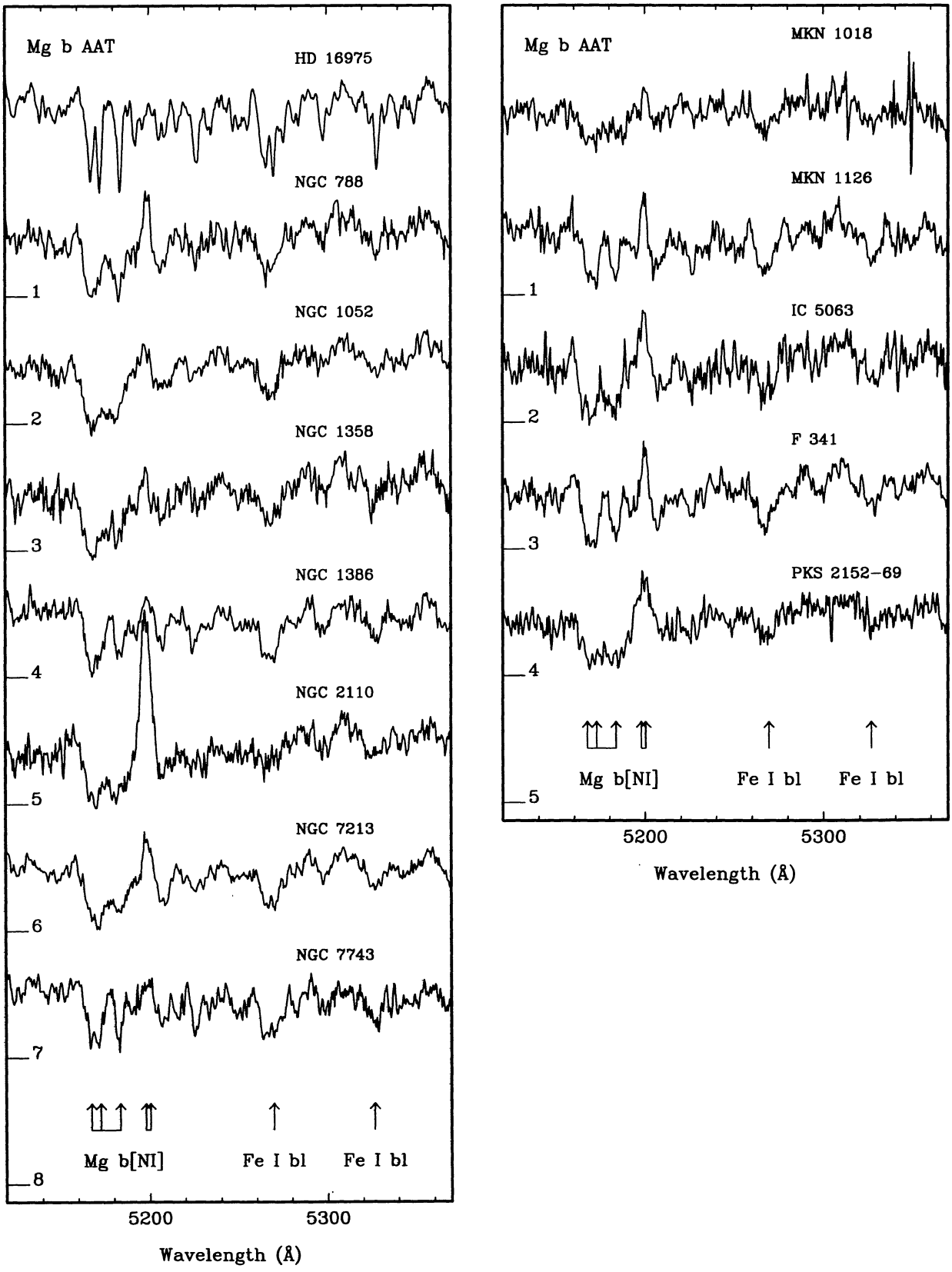

FIG. 3*b*—*Continued*

unit wavelength. The zero points are indicated as tick marks on the left border, and the locations of the strongest features are indicated at the bottom. To show the instrumental resolution, a stellar template is plotted at the beginning of the plot for each spectral region. The AAT spectra are shown separately, since they have significantly higher spectral resolution.

These spectra span a wide range of signal-to-noise ratio and absorption-line strength. Because the cross-correlation method makes use of the entire spectrum, even some of the poorest looking spectra can yield reasonably reliable redshifts and dispersions, giving repeatable results for independent observations. Nevertheless, reliable redshifts and/or dispersions could not be ascertained in a number of cases, either because of corrupting emission lines, strong sky absorption, low signal-to-noise ratio, or the weakness of the absorption lines. These objects are identified with a cross in Figure 3.

4.2. *The Cross-Correlation Method*

Stellar redshifts, V_*, and velocity dispersions, σ_*, were measured using the cross-correlation method described in detail by Tonry & Davis (1979), with some modifications. Briefly, the cross-correlation, $c(n)$, between a galaxy spectrum, $g(n)$, and a single-star template spectrum, $t(n)$, yields a function with a peak whose location and width are related to the redshift and velocity dispersion of the stars in the galaxy. Here, the spectral bins, n, evenly sample ln λ, so that velocity shifts correspond to uniform shifts in n, and symmetric velocity distributions are symmetric functions in n. The method also assumes that the galaxy spectrum is well represented by a single-star spectrum convolved with a Gaussian broadening function, b, offset from zero velocity by an amount δ. Thus, we have

$$c(n) = t(n) \times g(n) = \int_{-\infty}^{+\infty} t(m) g(m+n)\, dm\,, \qquad (1)$$

$$g(n) \simeq b(n-\delta) * t(n) = \int_{-\infty}^{+\infty} b(x-\delta) t(n-x)\, dx\,, \qquad (2)$$

where $\times$ and $*$ denote cross-correlation and convolution, respectively. Combining equations (1) and (2), we have

$$c(n) \simeq t(n) \times \{ b(n-\delta) * t(n) \} = \int_{-\infty}^{+\infty} t(m) \int_{-\infty}^{+\infty} b(x-\delta) t(m+n-x)\, dx\, dm\,. \qquad (3)$$

Upon changing the order of integration, this becomes

$$c(n) \simeq \int_{-\infty}^{+\infty} b(x-\delta) \int_{-\infty}^{+\infty} t(m) t(m+n-x)\, dm\, dx\,. \qquad (4)$$

Note that the inner integral is just the autocorrelation function $a(n-x) = t \times t$, and substitution yields a convolution integral,

$$c(n) \simeq \int_{-\infty}^{+\infty} b(x-\delta) a(n-x)\, dx = b(n-\delta) * \{ t(n) \times t(n) \}\,. \qquad (5)$$

Thus, the cross-correlation function of the galaxy and template spectra is approximated by the autocorrelation of the template spectrum convolved with the broadening function. The redshift, V_*, is obtained from the displacement of the cross-correlation peak from zero. In principle, the width of the broadening function, σ_*, can be derived from the width of the cross-correlation peak, after correcting for instrumental resolution by subtracting the width of the autocorrelation peak in quadrature. In practice, a more empirical approach is adopted by defining a relation between the σ of the Gaussian broadening function and the width, w_p, of the cross-correlation peak, the so-called "σ-width relation." Measuring the width of the peak of the actual cross-correlation function then gives σ_* directly from the σ-width relation. An initial set of FORTRAN routines, which served as the basis for our analysis package, was kindly provided by M. Colless and G. Efstathiou.

4.3. *Procedure*

There are a number of steps to the analysis. First, we extracted the nuclear region by summing along the slit. Usually three spatial channels were combined, resulting in a typical effective aperture of $\sim 1\farcs5 \times 2\farcs2$ (slit width $\times$ slit length). In most cases this was comparable to the FWHM of the seeing/instrument profile, as measured directly from adjacent star exposures. Occasionally it was necessary to include extra spatial channels to improve the signal-to-noise ratio. This was done only if the dispersion value was not significantly altered by including more channels.

Second, each spectrum was rebinned onto a logarithmic wavelength scale,

$$n = \frac{c}{\Delta V} \ln \frac{\lambda}{\lambda_0}\,, \qquad (6)$$

where λ_0 is the starting wavelength, ΔV is the logarithmic bin size in km s^{-1} bin^{-1} and n is the new bin number. To exclude relatively barren spectral regions (which lower the net signal-to-noise ratio), we chose to work with windows at 4675–5545 Å in the visual and 8440–8733 Å in the near-infrared. Because these windows are redshifted for the galaxies, we used an initial guess at the redshift for each galaxy to select a starting wavelength for the logarithmic rebinning. For computational convenience (see below) we chose 2048 logarithmic bins, giving $\sim$25 km s^{-1} bin^{-1} for the Mg b region and $\sim$5 km s^{-1} bin^{-1} for the Ca II triplet region.

Next, gross trends in the continuum shape were removed by subtracting a third-order polynomial fit to each spectrum. Note that this removes the influence of dilution by a featureless (AGN-like) continuum. Such a continuum component only adds noise to the absorption lines but does not otherwise affect them. Narrow emission lines, poorly subtracted sky lines, and unwanted intrinsically broad stellar absorption lines (primarily Hβ), were removed by simple interpolation. Broad emission lines (O I λ8446 and Hβ in Seyfert 1 galaxies) were fitted with Gaussians and subtracted, preserving the superposed stellar absorption lines. Failing to remove these emission lines, particularly the strong narrow lines, causes serious problems with the analysis. The ends of each spectrum (100 logarithmic bins on each side) were multiplied by a cosine bell function to bring each end smoothly to zero. Finally, to avoid wraparound effects, each spectrum was padded with zeros at one end, making a total of 4096 bins (see Simkin 1974).

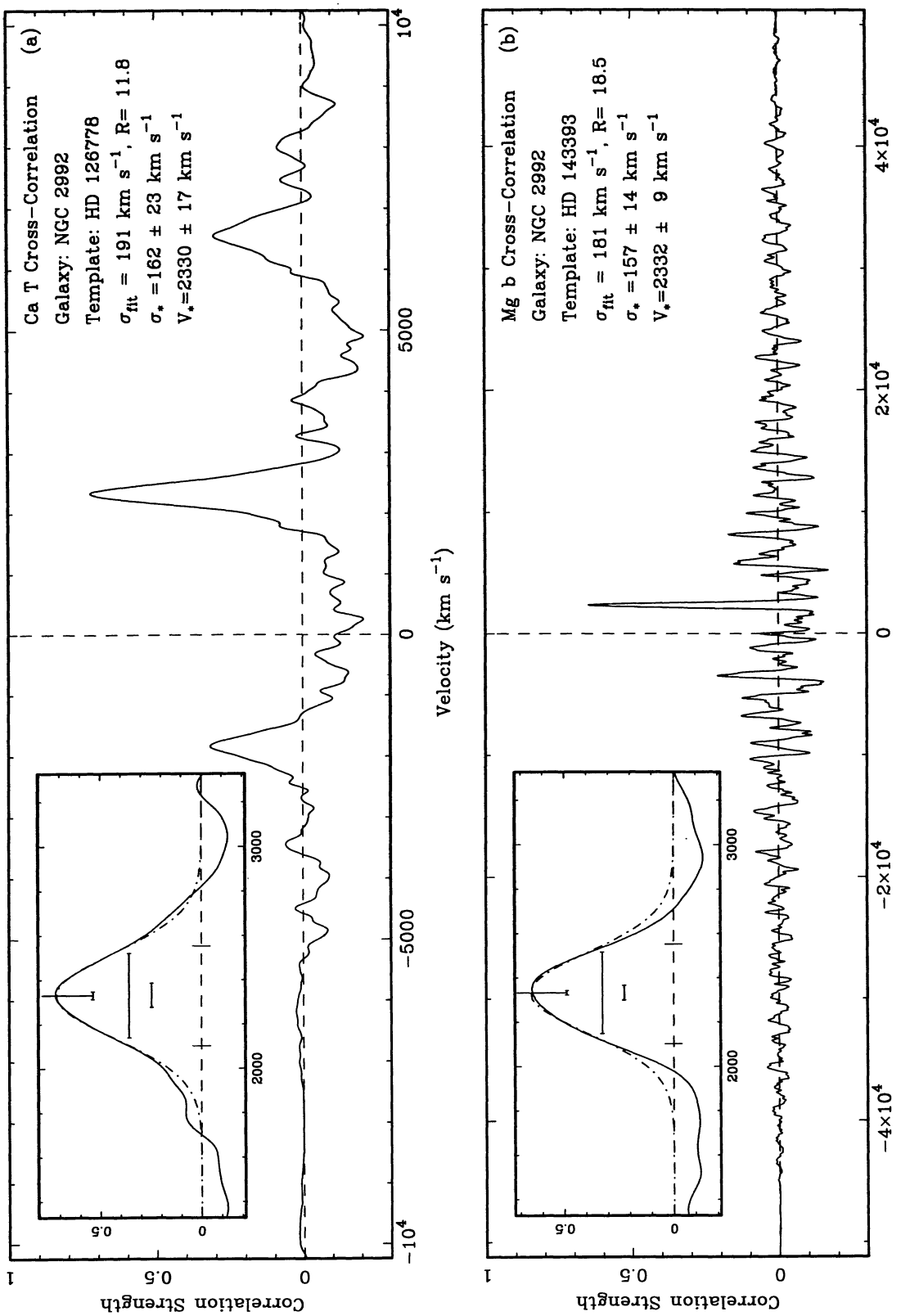

FIG. 4.—Cross-correlation functions for NGC 2992 are displayed in each spectral range to show differences in the two spectral regions. The insets show expansion of the area near the peak. The dash-dot line is the Gaussian fit, with the peak center and error marked as the vertical line and error bar. Below this, two horizontal bars are drawn to represent the resolution-corrected velocity width and its error. The tick marks on the dashed $Y = 0$ line show the region fitted.

Stellar template spectra were treated in the same way as the object spectra except that they were all shifted to zero velocity. The shifts were determined by cross-correlation with a spectrum of the twilight sky, which served as a zero-velocity reference. Comparison of the measured radial velocities for the templates with published values showed good agreement, with mean difference 0.3 km s^{-1} and rms difference 13 km s^{-1}.

For computational convenience, the cross-correlations were performed using fast Fourier transforms, since the Fourier transform of equation (1) gives $C(k) = G(k)T^*(k)$, where capitals denote Fourier transforms, k is frequency, and $T^*(k)$ is the complex conjugate of $T(k)$. These have the added advantage of allowing a simple ramp filter to be applied to $C(k)$ before transforming back to $c(n)$. The filter removes low-frequency fluctuations, arising from unwanted residual broad emission or absorption features, and high-frequency noise. To minimize the influence of the filter on the absorption lines of interest, we carefully avoided filtering frequencies associated with Gaussians of $\sigma_* \sim 50$–300 km s^{-1} in the spectral domain (i.e., Gaussians of $\sigma_k = N/2\pi\sigma_*$ in the frequency domain, where N is the total number of bins).

After returning to the spectral domain, the main peak of the cross-correlation function is identified and fitted with a Gaussian whose base is at the zero level. Only points above the half-maximum height are included in the fit. In principle, ideal galaxy and template spectra would give a Gaussian cross-cor-

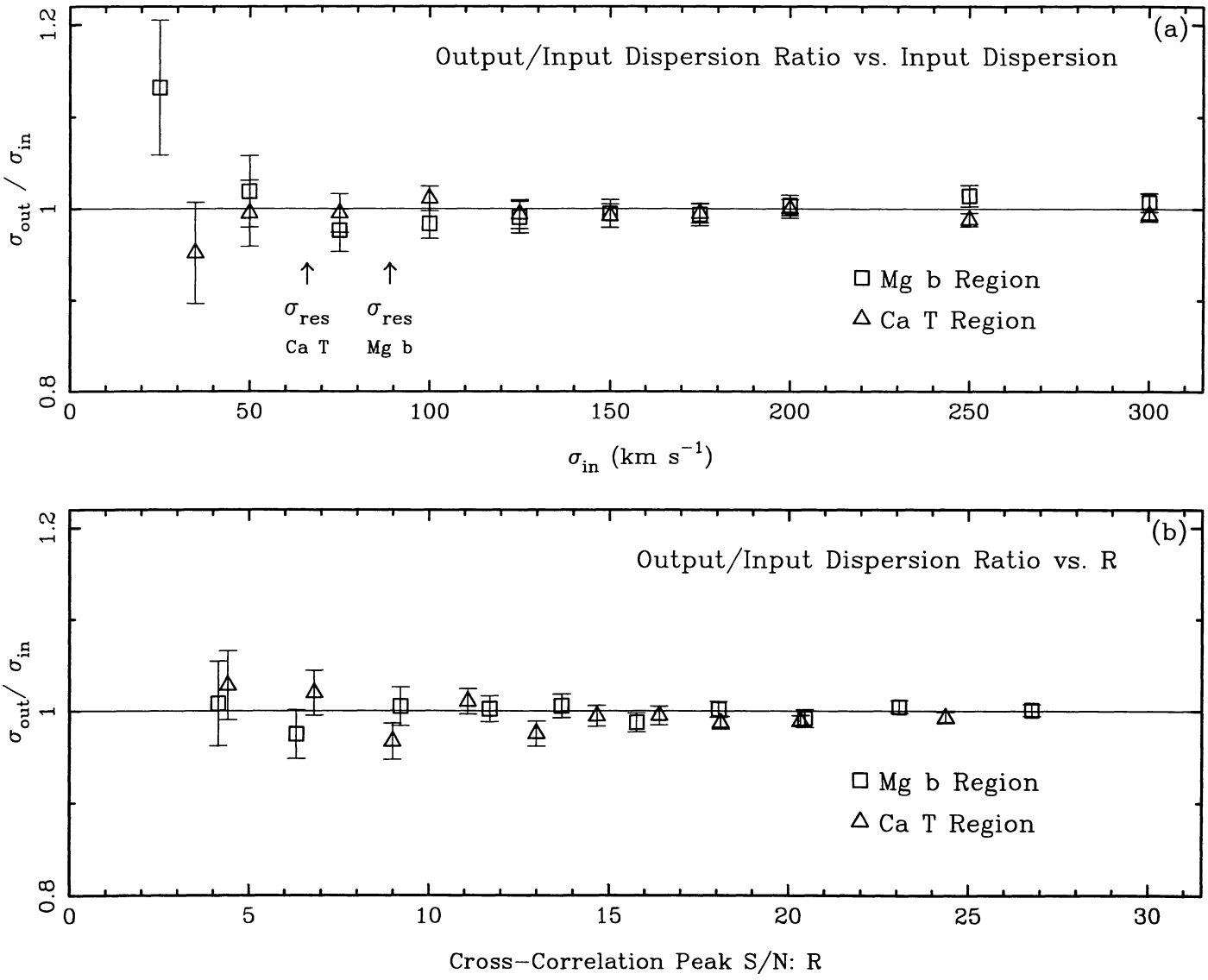

FIG. 5.—Results of testing the cross-correlation method using our artificial data set (see § 4.6), shown for each spectral region. Stellar templates from our KPNO data were broadened by a range of σ_{in} and degraded by adding noise in varying amounts to simulate galaxy spectra. Each point represents the mean of 250 spectra, and the error bar is the error on the mean. In (*a*) the ratio σ_{out}/σ_{in} is plotted against σ_{in}. Note that there are no significant deviations from $\sigma_{out}/\sigma_{in} = 1$ for input values above 50% of the instrumental resolution. In (*b*) the same ratio is plotted against R, the signal-to-noise ratio of the cross-correlation peak (see § 4.4). Although the error bars are larger and the scatter increases for lower R, no significant systematic deviations are present. (Spectra with σ_{in} below 50% of the instrumental resolution are excluded from this plot.)

relation peak whose width, after subtracting the instrumental contribution, would yield σ_*. In practice, cross-correlation functions differ from Gaussians due to template mismatch, blended features, filtering, non-Gaussian absorption lines, and non-Gaussian velocity distributions. In order to recover the value of σ_*, therefore, a relationship is defined between the σ of a Gaussian broadening function and the width of its associated cross-correlation peak. This relation is generated by convolving a template star spectrum by a Gaussian of known width, σ, and cross-correlating this with a second template star of the same spectral type (i.e., using eq. [3] to simulate the cross-correlation of a galaxy with a template). Fitting to the peak of this cross-correlation gives a width, associated with the input σ. Repeating this for a sequence of σ defines the σ-width relation, which is fitted using a polynomial. For each galaxy, the width of the cross-correlation peak is measured and the corresponding value of σ_* found using the σ-width relation. Note that different σ-width relations must be defined for each spectral region, each filter, and each template used in the cross-correlation.

4.4. *Error Analysis*

In the absence of noise, perfectly matched galaxy and template spectra give perfectly symmetric cross-correlation functions. In practice, noise and differences between galaxy and template spectra introduce distortions to the cross-correlation function, which can be used to estimate errors in V_* and σ_*. We follow the method described by Tonry & Davis (1979), with slight modification.

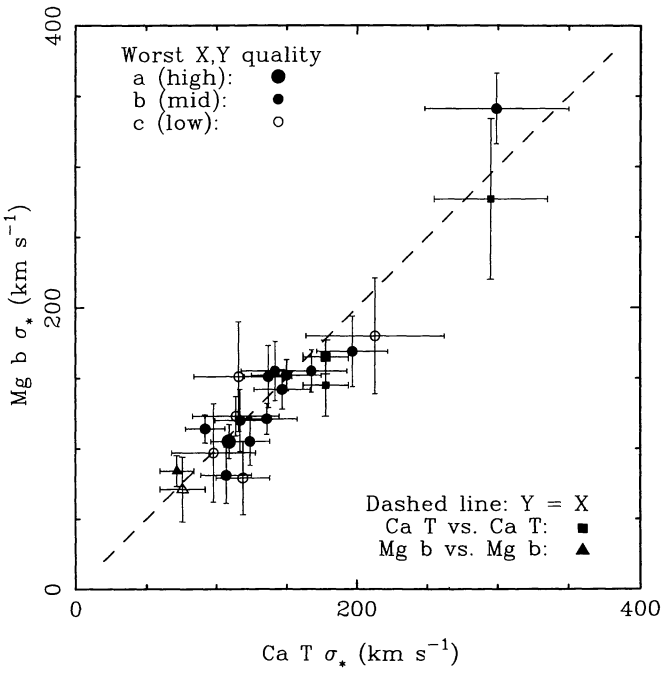

FIG. 6.—Velocity dispersions, σ_*, are compared for objects observed in both spectral regions. The type of symbol indicates the lowest data-quality rating: large = a, small = b, open = c. The squares and triangles represent multiple observations for objects in the same wavelength region (NGC 1068, Mrk 3, NGC 5427, and NGC 5273). We note that the scatter is largely within the error bars.

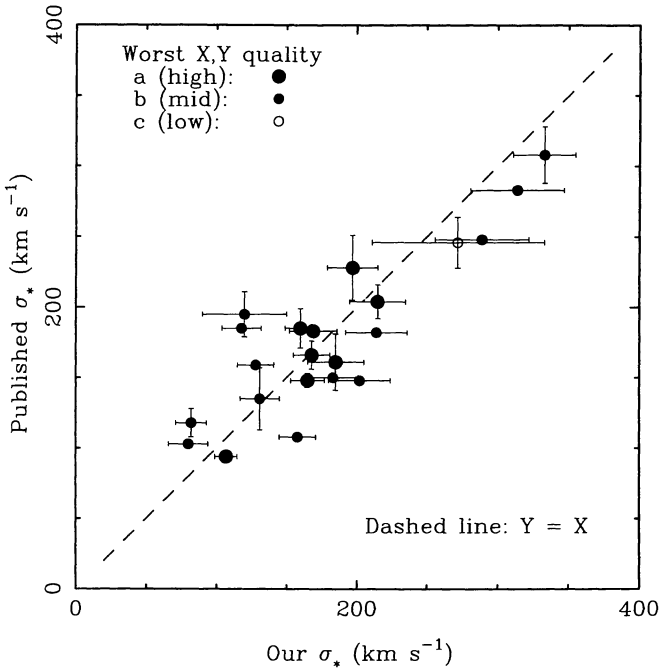

FIG. 7.—Our combined Mg *b* and Ca II triplet velocity dispersions σ_* are compared with published values for the same objects. The lowest data-quality rating is indicated by the kind of point plotted. There is good overall agreement; however, a few discrepant points appear and are noted in the Appendix.

The rms of the antisymmetric component, σ_a, is given by

$$\sigma_a^2 = \frac{1}{2N}\sum_n [c(n+\delta) - c(\delta - n)]^2 . \quad (7)$$

It is assumed that noise and template mismatch introduce both symmetric and antisymmetric components to the cross-correlation function in approximately equal amounts. The amplitude of a typical "error bump" in the cross-correlation is therefore $\sim 2^{1/2}\sigma_a$. An effective signal-to-noise ratio for the cross-correlation peak is therefore

$$R = \frac{h}{2^{1/2}\sigma_a}, \quad (8)$$

where h is the peak height. Tonry & Davis use this to estimate the effect of an error bump on the measured location, V_*, and width, w_p, of the cross-correlation peak. They find these effects to be approximately the same,

$$\epsilon = \Delta V_* = \Delta w_p \simeq \frac{f_w N}{8B}\frac{1}{1+R}, \quad (9)$$

where N is the number of ln λ bins and B is the most likely separation between the main peak and a perturbing bump. In practice, B is evaluated from simulated data, as described below in § 4.6. We have introduced the additional factor $f_w = w_p/w_t$, where w_t is the width of the cross-correlation peak of two template stars. This factor accounts for the proportionately

TABLE 2

SEYFERT GALAXY NUCLEAR VELOCITY DISPERSIONS

	Name	adopted $\sigma_* \pm \epsilon_*$ km s^{-1}	Ca T $\sigma_* \pm \epsilon_*$ km s^{-1}	Run	Exp. sec	Aper. "×"	P.A. deg	seeing "	Mg b $\sigma_* \pm \epsilon_*$ km s^{-1}	Run	Exp. sec	Aper. "×"	P.A. deg	seeing "	Combined $\sigma_* \pm \epsilon_*$ km s^{-1}	Published $\sigma_* \pm \epsilon_*$ km s^{-1}	Refs.
	(1)	(2)	(3)	(4)	(5)	(6)	(7)	(8)	(9)	(10)	(11)	(12)	(13)	(14)	(15)	(16)	(17)
1	NGC 513	152 ± 10a	150 ± 25	3	3600	1.5×2.3	75	3.7	152 ± 11	3	2400	1.5×2.3	90	1.7	152 ± 10a	...	...
2	NGC 788	140 ± 20a	...	...	...	...	...	...	140 ± 20	1	4400	2.2×3.6	115	3.0	140 ± 20a	...	...
3	NGC 1052	207 ± 10a	...	...	...	...	...	...	215 ± 20	1	1400	2.2×3.6	120	4.0	215 ± 20a	204 ± 12a	5
4	NGC 1068	151 ± 12b	165 ± 12	3	1200	1.5×2.3	75	3.8	...	...	...	...	...	...	165 ± 12a	148 ± 5a	7,3
5	NGC 1275	248 ± 17a	272 ± 61	3	1800	1.5×3.1	75	4.3	...	...	...	...	...	...	272 ± 61c	246 ± 18a	5
6	NGC 1320	116 ± 11a	124 ± 14	3	2400	1.5×2.3	140	1.7	105 ± 17	3	1500	1.5×2.3	140	1.6	116 ± 11a	...	...
7	NGC 1358	173 ± 14a	...	...	...	...	...	...	185 ± 20	1	2000	2.2×3.6	125	2.5	185 ± 20a	161 ± 20a	4
8	NGC 1386	120 ± 30b	...	...	...	...	...	...	120 ± 30	1	2400	2.2×3.6	25	2.0	120 ± 30b	195 ± 16a	2
9	NGC 1566	100 ± 10a	...	...	...	...	...	...	...	...	...	...	...	...	...	100 ± 10a	9
10	NGC 1667	173 b	...	...	...	...	...	...	...	...	...	...	...	...	...	173 b?	7
11	NGC 2110	220 ± 25a	...	...	...	...	...	...	220 ± 25	1	3500	2.2×3.6	160	2.5	220 ± 25a	...	...
12	NGC 2273	124 ± 10a	136 ± 22	2	2500	1.5×1.4	90	1.7	121 ± 11	4	1960	1.5×2.3	90	2.7	124 ± 10a	...	...
13	NGC 2841	209 ± 14a	197 ± 18	2	1000	1.5×2.1	90	1.4	...	...	...	...	...	...	197 ± 18a	228 ± 23a	10
14	NGC 2992	158 ± 13a	168 ± 25	2	3000	1.5×2.1	20	1.9	155 ± 15	4	1800	1.5×2.3	15	2.4	158 ± 13a	108 a	7,6
15	NGC 3031	167 ± 8a	168 ± 13	2	1000	1.5×2.1	90	1.4	...	...	...	...	...	...	168 ± 13a	166 ± 10a	10
16	NGC 3185	61 ± 20c	...	...	...	...	...	...	61 ± 20	5	1800	1.5×2.3	110	2.3	61 ± 20c	...	...
17	NGC 3227	144 ± 22b	128 ± 13	2	2000	1.5×2.1	155	1.9	97 ± 23r	5	2400	1.5×2.3	90	4.3	128 ± 13a	159 a	7,6
18	NGC 3362	92 ± 28c	...	...	...	...	...	...	92 ± 28	5	3600	1.5×2.3	90	2.9	92 ± 28c	...	...
19	NGC 3516	235 a	...	...	...	...	...	...	...	...	...	...	...	...	...	235 a	7
20	NGC 3786	142 ± 13a	137 ± 17	2	3000	1.5×2.8	77	1.9	151 ± 22	4	2700	1.5×2.3	90	3.8	142 ± 13a	...	...
21	NGC 3982	62 ± 12b	...	...	...	...	...	...	62 ± 12	4	3250	1.5×2.3	90	2.5	62 ± 12b	...	...
22	NGC 3998	319 ± 15a	299 ± 51	2	2000	1.5×2.1	90	1.4	341 ± 25	5	1200	1.5×2.3	90	2.4	333 ± 22b	308 ± 20a	8
23	NGC 4051	88 ± 13b	88 ± 13	2	2500	1.5×2.1	90	1.4	84 ± 22r	5	1200	1.5×2.3	90	2.3	88 ± 13b	...	...
24	NGC 4117	95 ± 15b	...	...	...	...	...	...	95 ± 15	4	1800	1.5×2.3	15	2.4	95 ± 15b	...	...
25	NGC 4151	178 c	119 ± 26r	2	1000	1.5×3.5	0	1.7	...	...	...	...	...	...	119 ± 26r	178 c	7,6
26	NGC 4339	132 ± 12a	...	...	...	...	...	...	131 ± 14	5	2650	1.5×16.	90	2.0	131 ± 14a	135 ± 22b	8
27	NGC 4388	119 b	...	...	...	...	...	...	74 ± 34r	4	1800	1.5×7.0	90	2.3	74 ± 34r	119 b	7,6
28	NGC 4579	170 ± 18b	...	...	...	...	...	...	160 ± 11	4	1200	1.5×2.3	90	2.2	160 ± 11a	185 ± 14a	10
29	NGC 4593	124 ± 29c	124 ± 29	2	2500	1.5×3.5	0	1.4	109 ± 25r	5	1800	1.5×2.3	90	2.5	124 ± 29c	...	...
30	NGC 4941	107 ± 9a	109 ± 13	2	2000	1.5×2.1	15	2.1	105 ± 12	4	1800	1.5×2.3	15	2.4	107 ± 9a	...	...
31	NGC 5194	102 ± 25b	82 ± 11	2	1200	1.5×2.1	90	1.4	...	...	...	...	...	...	82 ± 11a	118 ± 10b	10
32	NGC 5252	190 ± 27b	...	...	...	...	...	...	190 ± 27	4	3900	1.5×2.3	15	2.6	190 ± 27b	...	...
33	NGC 5273	79 ± 8a	...	...	...	...	...	...	79 ± 8	4	1800	1.5×2.3	15	2.9	79 ± 8a	...	...
34	NGC 5347	93 ± 21b	...	...	...	...	...	...	73 ± 14	4	1800	1.5×2.3	90	1.9	73 ± 14b	103 a	7
35	NGC 5427	74 ± 13b	...	...	...	...	...	...	74 ± 13	5	1800	1.5×2.3	90	2.6	74 ± 13b	...	...
36	NGC 5548	–	...	...	...	...	...	...	47 ± 67r	5	3000	1.5×2.3	90	3.3	47 ± 67r	...	...
37	NGC 5929	121 ± 13a	114 ± 31	2	2800	1.5×2.1	47	1.3	123 ± 14	5	3000	1.5×2.3	46	3.4	121 ± 13a	...	...
38	NGC 5940	–	204 ± 95r	3	2400	1.5×3.9	90	2.2	159 ± 49r	3	600	1.5×3.9	90	2.3	159 ± 49r	...	...
39	NGC 5953	101 ± 9b	92 ± 14	3	1200	1.5×2.3	48	3.6	114 ± 10	3	1800	1.5×2.3	90	1.9	107 ± 8a	94 a	7
40	NGC 6104	148 ± 35c	75 ± 50r	3	3600	1.5×5.5	90	2.0	148 ± 35	3	1200	1.5×3.9	90	1.9	148 ± 35c	...	...
41	NGC 6482	293 ± 33a	314 ± 33	3	1800	1.5×8.6	48	3.7	...	...	...	...	...	...	314 ± 33b	283 a	1
42	NGC 6702	193 ± 23b	...	...	...	...	...	...	214 ± 22	5	1200	1.5×7.0	15	2.0	214 ± 22b	182 a	1
43	NGC 6703	177 ± 17a	171 ± 17	3	1200	1.5×2.3	90	2.9	...	...	...	...	...	...	171 ± 17a	183 a	10,1
44	NGC 6814	115 ± 18b	115 ± 18	3	2400	1.5×2.3	0	3.7	...	...	...	...	...	...	115 ± 18b	...	...
45	NGC 7212	137 ± 30c	137 ± 30	3	4800	1.5×3.9	0	4.7	...	...	...	...	...	...	137 ± 30c	...	...
46	NGC 7213	185 ± 20a	...	...	...	...	...	...	185 ± 20	1	2600	2.2×3.6	115	1.8	185 ± 20a	...	...
47	NGC 7319	130 ± 25c	116 ± 32	3	3600	1.5×1.6	140	3.8	151 ± 39	3	1200	1.5×1.6	140	1.4	130 ± 25c	...	...
48	NGC 7603	194 ± 31c	213 ± 49	3	3600	1.5×2.3	160	2.3	180 ± 41	3	1200	1.5×2.3	90	1.7	194 ± 31c	...	...
49	NGC 7672	98 ± 23c	98 ± 30	3	3600	1.5×2.3	90	2.2	97 ± 35	3	1200	1.5×3.9	90	2.0	98 ± 23c	...	...
50	NGC 7682	123 ± 17a	123 ± 17	3	3600	1.5×2.3	160	2.4	...	...	...	...	...	...	123 ± 17a	...	...
51	NGC 7743	83 ± 20b	...	...	...	...	...	...	83 ± 20	1	2200	2.2×3.6	95	2.5	83 ± 20b	...	...
52	MKN 1	115 ± 26b	115 ± 26	3	4800	1.5×2.3	75	4.3	...	...	...	...	...	...	115 ± 26b	...	...
53	MKN 3	269 ± 33b	289 ± 33	3	4800	1.5×2.3	85	2.0	...	...	...	...	...	...	289 ± 33b	248 b?	7
54	MKN 6	–	–	2	2000	1.5×2.1	0	1.8	...	...	...	...	...	...	–	...	...
55	MKN 10	137 ± 38c	...	...	...	...	...	...	137 ± 38	5	2400	1.5×3.1	90	2.8	137 ± 38c	...	...
56	MKN 78	172 ± 18b	197 ± 25	2	4000	1.5×2.1	90	2.1	169 ± 25	5	3600	1.5×2.3	90	2.7	183 ± 18b	150 c	7,6
57	MKN 176	202 ± 22b	...	...	...	...	...	...	202 ± 22	5	3000	1.5×2.3	55	3.0	202 ± 22b	148 r	7,6
58	MKN 270	148 ± 14a	...	...	...	...	...	...	148 ± 14	5	1200	1.5×2.3	90	2.2	148 ± 14a	...	...
59	MKN 348	118 ± 14b	117 ± 18	3	3600	1.5×2.3	95	2.0	120 ± 22	3	1800	1.5×2.3	90	2.0	118 ± 14b	185 b?	7
60	MKN 372	–	–	2	2000	1.5×2.1	0	1.8	...	...	...	...	...	...	–	...	...
61	MKN 506	–	–	3	3600	1.5×2.3	90	2.1	...	...	...	...	...	...	–	...	...
62	MKN 533	144 ± 32c	144 ± 32	3	3600	1.5×2.3	90	1.9	...	...	...	...	...	...	144 ± 32c	...	...
63	MKN 573	123 ± 16a	123 ± 16	3	3600	1.5×2.3	125	2.2	...	...	...	...	...	...	123 ± 16a	...	...
64	MKN 590	169 ± 28b	169 ± 28	3	3600	1.5×2.3	75	3.0	...	...	...	...	...	...	169 ± 28b	...	...
65	MKN 622	100 ± 15a	...	...	...	...	...	...	100 ± 15	4	2400	1.5×2.3	90	2.4	100 ± 15a	...	...
66	MKN 686	144 ± 11a	147 ± 20	2	2500	1.5×2.1	15	2.1	142 ± 14	5	1800	1.5×2.3	15	2.2	144 ± 11a	...	...
67	MKN 766	–	...	...	...	...	...	...	–	4	2700	1.5×2.3	90	2.1	–	...	...
68	MKN 917	149 ± 16b	142 ± 24	3	3600	1.5×2.3	140	3.3	155 ± 21	3	1800	1.5×2.3	140	1.7	149 ± 16b	...	...
69	MKN 1018	195 ± 25b	...	...	...	...	...	...	195 ± 25	1	4900	2.2×4.8	176	2.0	195 ± 25b	...	...
70	MKN 1040	151 ± 32c	151 ± 32	3	3600	1.5×2.3	75	3.0	...	...	...	...	...	...	151 ± 32c	...	...

TABLE 2—*Continued*

	Name	adopted $\sigma_* \pm \epsilon_*$ km s^{-1}	Ca T $\sigma_* \pm \epsilon_*$ km s^{-1}	Run	Exp. sec	Aper. "×"	P.A. deg	seeing "	Mg b $\sigma_* \pm \epsilon_*$ km s^{-1}	Run	Exp. sec	Aper. "×"	P.A. deg	seeing "	Combined $\sigma_* \pm \epsilon_*$ km s^{-1}	Published $\sigma_* \pm \epsilon_*$ km s^{-1}	Refs.
	(1)	(2)	(3)	(4)	(5)	(6)	(7)	(8)	(9)	(10)	(11)	(12)	(13)	(14)	(15)	(16)	(17)
71	MKN 1066	105 ± 15 b	119 ± 19	3	1800	1.5×2.3	140	1.9	79 ± 26	3	1200	1.5×2.3	140	1.8	105 ± 15 b	...	...
72	MKN 1126	85 ± 25 b	...	...	...	...	...	...	85 ± 25	1	4550	2.2×4.8	30	1.8	85 ± 25 b	...	...
73	MKN 1157	95 ± 13 b	107 ± 18	3	3600	1.5×1.6	95	2.3	81 ± 20	4	1200	1.5×1.6	90	1.7	95 ± 13 b	...	...
74	AKN 79	143 ± 20 b	143 ± 20	3	2400	1.5×1.6	95	2.0	...	...	...	...	...	...	143 ± 20 b	...	...
75	AKN 347	186 ± 26 b	...	...	...	...	...	...	186 ± 26	4	1800	1.5×2.3	90	2.3	186 ± 26 b	...	...
76	IC 5063	160 ± 25 a	...	...	...	...	...	...	160 ± 25	1	2700	2.2×3.6	115	2.2	160 ± 25 a	...	...
77	III ZW 55 N	212 a	–	2	1800	1.5×2.1	20	1.6	...	...	...	...	...	...	–	212 a	7,6
78	MCG 8-11-11	–	71 ± 51 r	2	2000	1.5×2.1	0	1.5	...	...	...	...	...	...	71 ± 51 r	...	...
79	F 341	114 ± 25 b	...	...	...	...	...	...	114 ± 25	1	4350	2.2×3.6	140	1.8	114 ± 25 b	...	...
80	ARP 107 A	93 ± 23 b	...	...	...	...	...	...	93 ± 23	4	2400	1.5×3.1	15	2.6	93 ± 23 b	...	...
81	UGC 3223	106 ± 28 c	...	...	...	...	...	...	106 ± 28	4	3600	1.5×2.3	90	2.2	106 ± 28 c	...	...
82	UGC 3995 A	155 ± 17 a	...	...	...	...	...	...	155 ± 17	5	1800	1.5×2.3	90	3.2	155 ± 17 a	...	...
83	UGC 6100	156 ± 25 b	...	...	...	...	...	...	156 ± 25	4	1800	1.5×2.3	15	2.5	156 ± 25 b	...	...
84	3C 120	162 ± 20 a	–	2	3500	1.5×2.1	90	1.4	...	...	...	...	...	...	–	162 ± 20 a	5
85	PKS 2152-69	245 ± 25 a	...	...	...	...	...	...	245 ± 25	1	4500	2.2×3.6	130	1.8	245 ± 25 a	...	...

Col. (1): Name. Col. (2): Adopted stellar velocity dispersion and error. Col. (3): Ca II triplet velocity dispersion and error. Cols. (4)–(8): Observing run number from Table 1 for Ca II triplet observations, exposure time, aperture (slit width × slit length), position angle in degrees, and FWHM of spatial profile in arcseconds (as estimated from short exposures of stars near the galaxy). Col. (9): Mg *b* velocity dispersion and error. Cols. (10)–(14): Observing run number from Table 1 for Mg *b* observations, exposure time, aperture (slit width × slit length), position angle in degrees, and FWHM of spatial profile in arcseconds (as estimated from short exposures of stars near the galaxy). Col. (15): Combined velocity dispersion and error. This is the weighted mean of both the Ca II triplet and the Mg *b* values if both are considered reliable. Col. (16): Published velocity dispersion and error. Col. (17): Reference to published velocity dispersion.

REFERENCES.— (1) Davies et al. 1987; (2) Dressler & Sandage 1983; (3) Dressler 1984; (4) Schechter 1983; (5) Smith, Heckman, & Illingworth 1990; (6) Terlevich 1994; (7) Terlevich, Diaz, & Terlevich 1990; (8) Tonry & Davis 1981; (9) van der Kruit & Freeman 1984; (10) Whitmore, McElroy, & Tonry 1985.

greater probability that a bump will affect a broad peak than a narrow one (apart from this factor, eq. [9] is the same as eq. [24] in Tonry & Davis). To obtain the error on σ_* from the error on w_p, we follow Tonry & Davis, who use an analytic form of the σ-width relation to propagate the errors (their eq. [28]):

$$(\Delta\sigma_*)^2 = 2(w_p^2\Delta w_p^2 + 4w_t^2\Delta w_t^2 + \sigma_*^4)^{1/2} - 2\sigma_*^2 , \quad (10)$$

where Δw_p and Δw_t are evaluated using equation (9).

4.5. *Examples of Cross-Correlation Functions*

Figure 4 presents two examples of cross-correlation functions for NGC 2992, one for the Mg *b* region and one for the Ca II triplet region. Gaussian fits to the peak are shown inset, including lines to mark the peak velocity, its error, the FWHM of the velocity broadening function ($2.35 \times \sigma_*$), and its error. Some differences between the two spectral regions are worth noting.

The Ca II triplet region includes only the three triplet lines. Since the lines always have the same relative strength, the cross-correlation function is relatively insensitive to the spectral type of the template star. Strong secondary peaks are produced where a line in the galaxy spectrum is aligned with a different line in the template spectrum. These secondary peaks can affect the shape of the main peak near its base, particularly for larger line widths, leading to curvature in the σ-width relation.

Because the Mg *b* range includes many spectral features, the secondary peaks are considerably weaker relative to the main peak. However, because there are more lines, the potential for spectral mismatch between galaxy and template is greater. To find the best match, each galaxy spectrum was cross-correlated with all of the available stellar templates, covering a range of spectral types from G0 through K5. The template which gave the highest value of the parameter R was selected for the analysis.

4.6. *Testing the Cross-Correlation Results*

We performed a series of tests to check the reliability of our method, its error estimates, its performance close to the instrument resolution, and its performance with noisy data.

In each spectral range and for each observational setup, 2500 artificial galaxy spectra were constructed by broadening a stellar template spectrum by a Gaussian of width 25 km s^{-1} < σ_{in} < 300 km s^{-1}. These were then degraded by adding varying amounts of noise. The spectra were analyzed using the methods described above, giving σ_{out}.

Figure 5*a* shows the ratio σ_{out}/σ_{in} as a function of σ_{in} for spectra constructed from templates observed on our 1990 September KPNO observing run. Each plotted point represents the mean of about 250 trials, and the error bar is the error on the mean. Clearly, there are no systematic errors even down to quite low velocity dispersions $\sigma_{in} \sim \frac{1}{2}\sigma_{res}$, where σ_{res} is the instrumental resolution. All our sample galaxies have measured dispersions above this limit. Figure 5*b* shows the ratio σ_{out}/σ_{in} as a function of R, the signal-to-noise ratio of the cross-correlation peak (see § 4.4). Again, there are no systematic errors which depend on the noise level of the data, although the random errors clearly increase for lower R, as expected (we excluded trials with $\sigma_{in} < \frac{1}{2}\sigma_{res}$ from this test). Similar results (not shown) were found for measurements of the redshift, V_*.

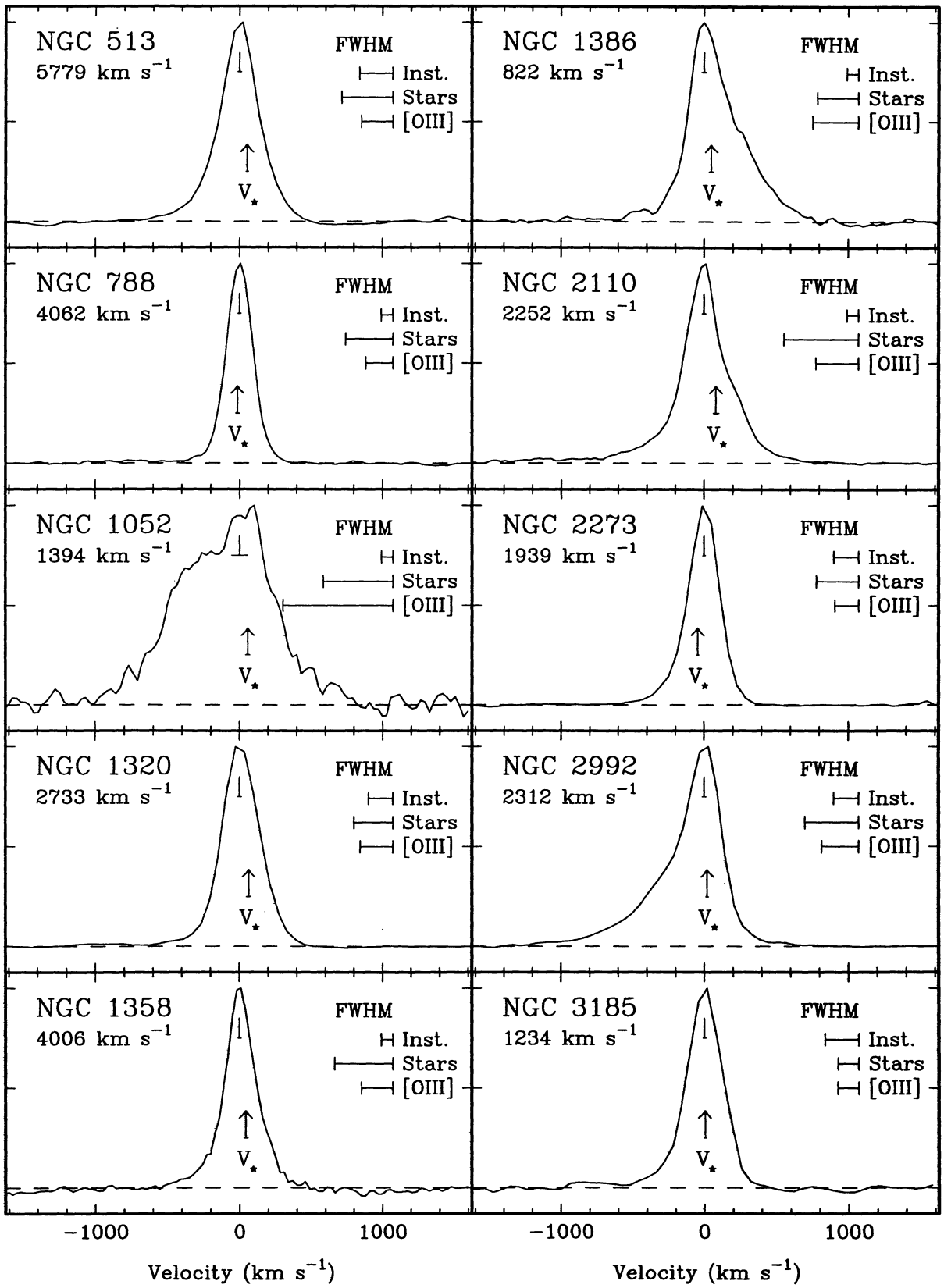

FIG. 8.—Emission-line profiles are displayed for [O III] λ5007. In each case the C80 parameter is taken as the line center. The vertical line shows its position and error, and its heliocentric value is given below the object name. The redshift of the stellar features is indicated by an arrow, and its error is drawn at its base. Three bars on the right indicate the FWHM values of for the instrument, the stellar velocity field, and the [O III] profile.

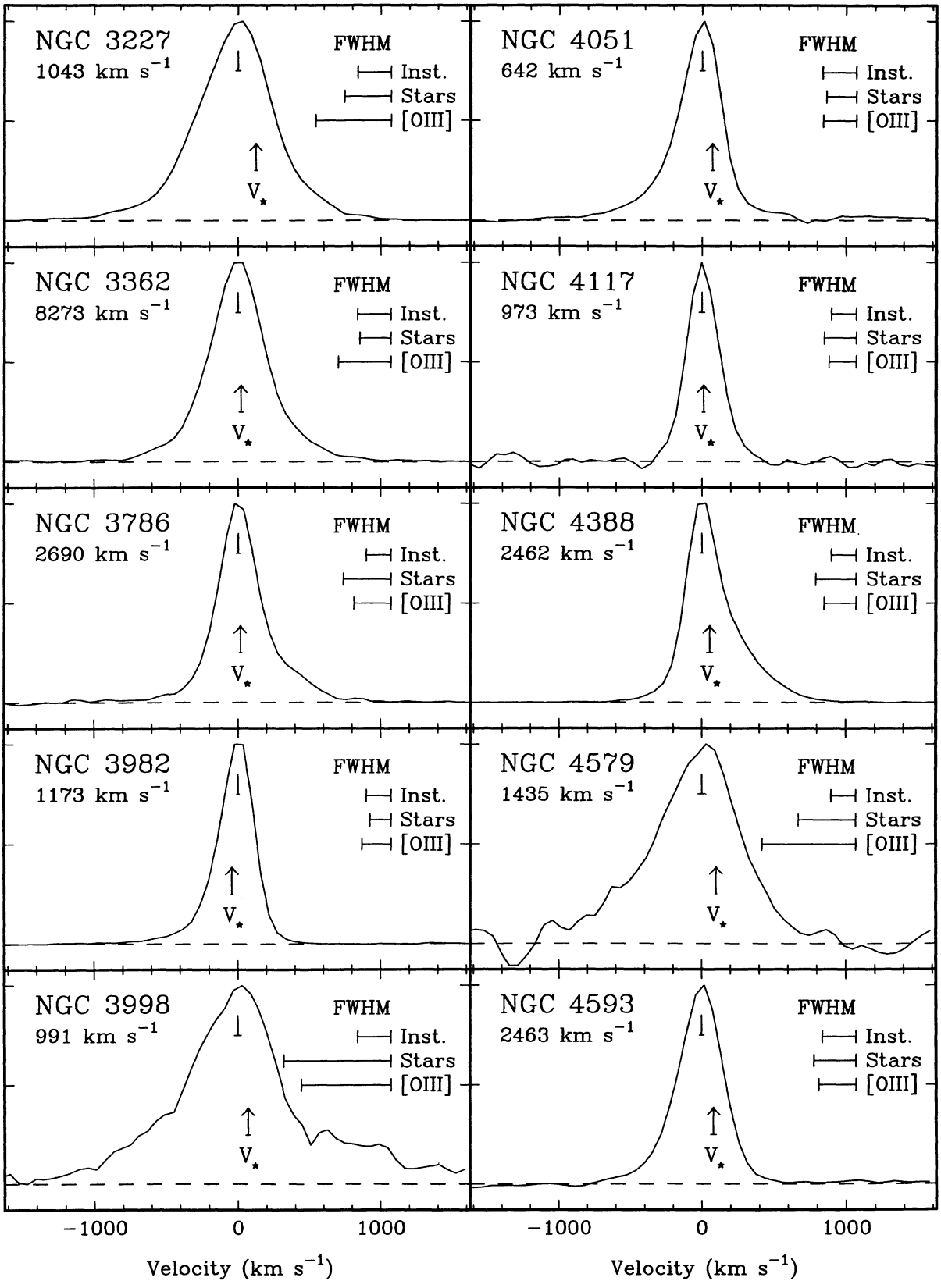

FIG. 8—*Continued*

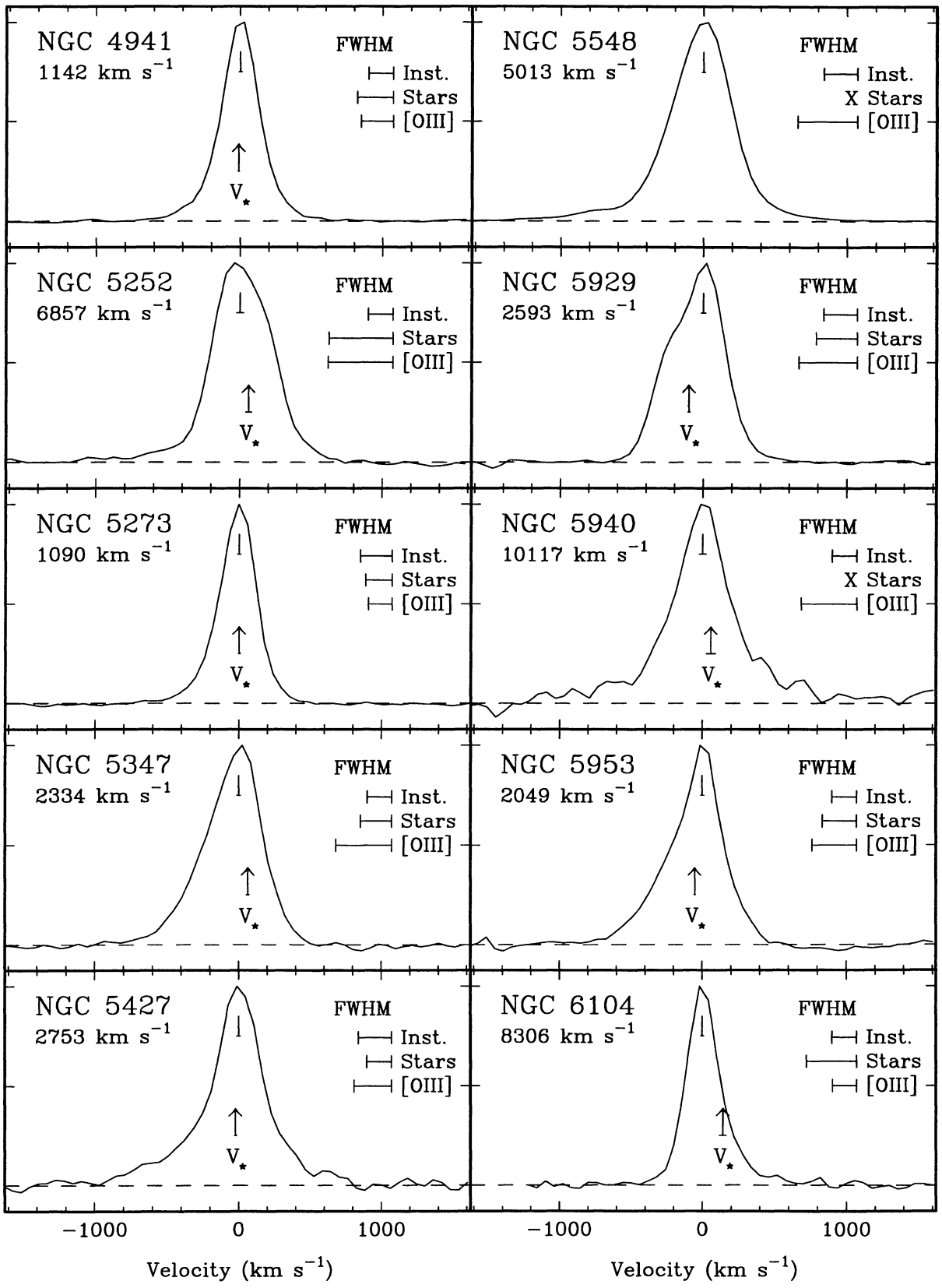

FIG. 8—*Continued*

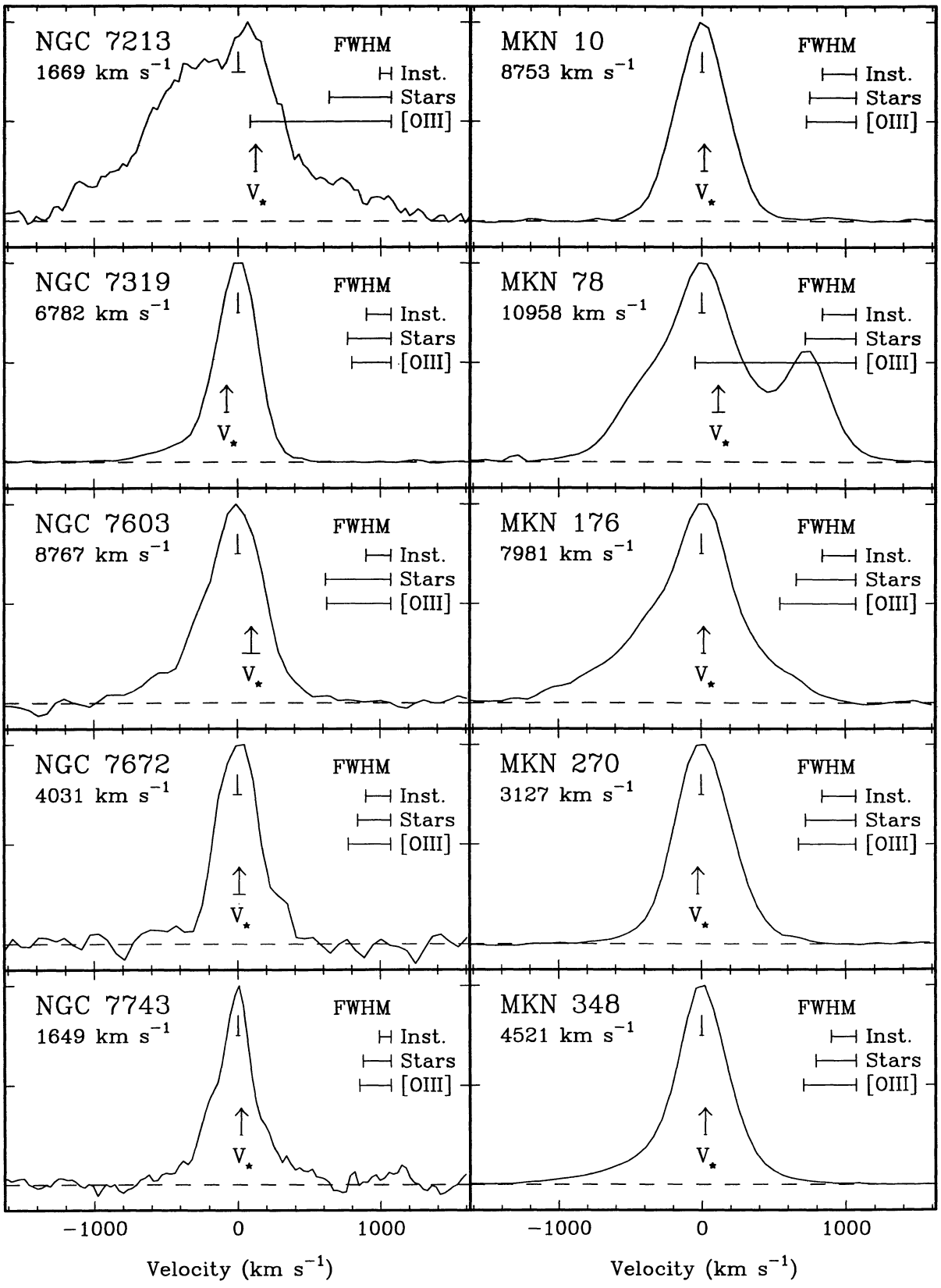

FIG. 8—*Continued*

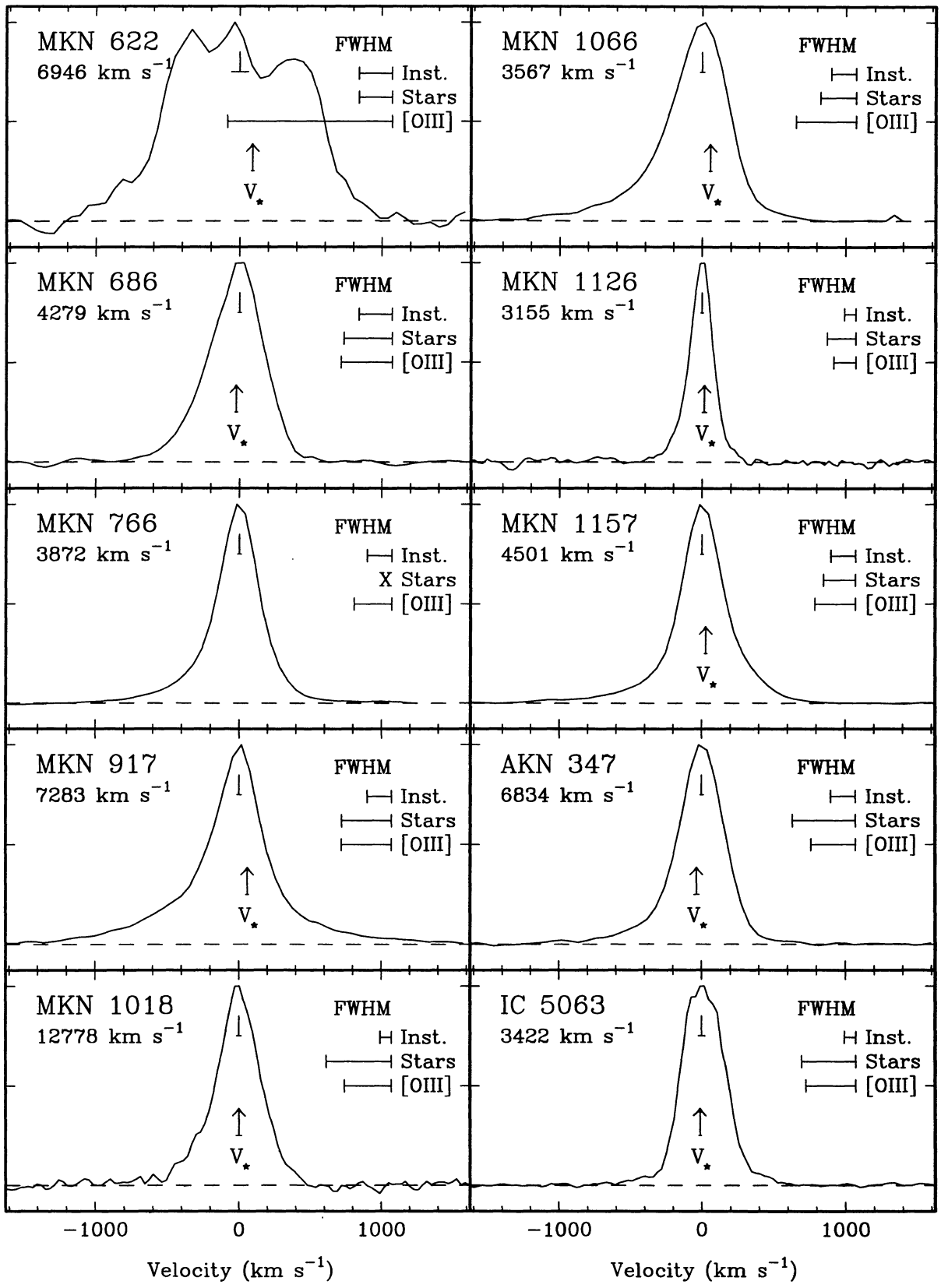

FIG. 8—*Continued*

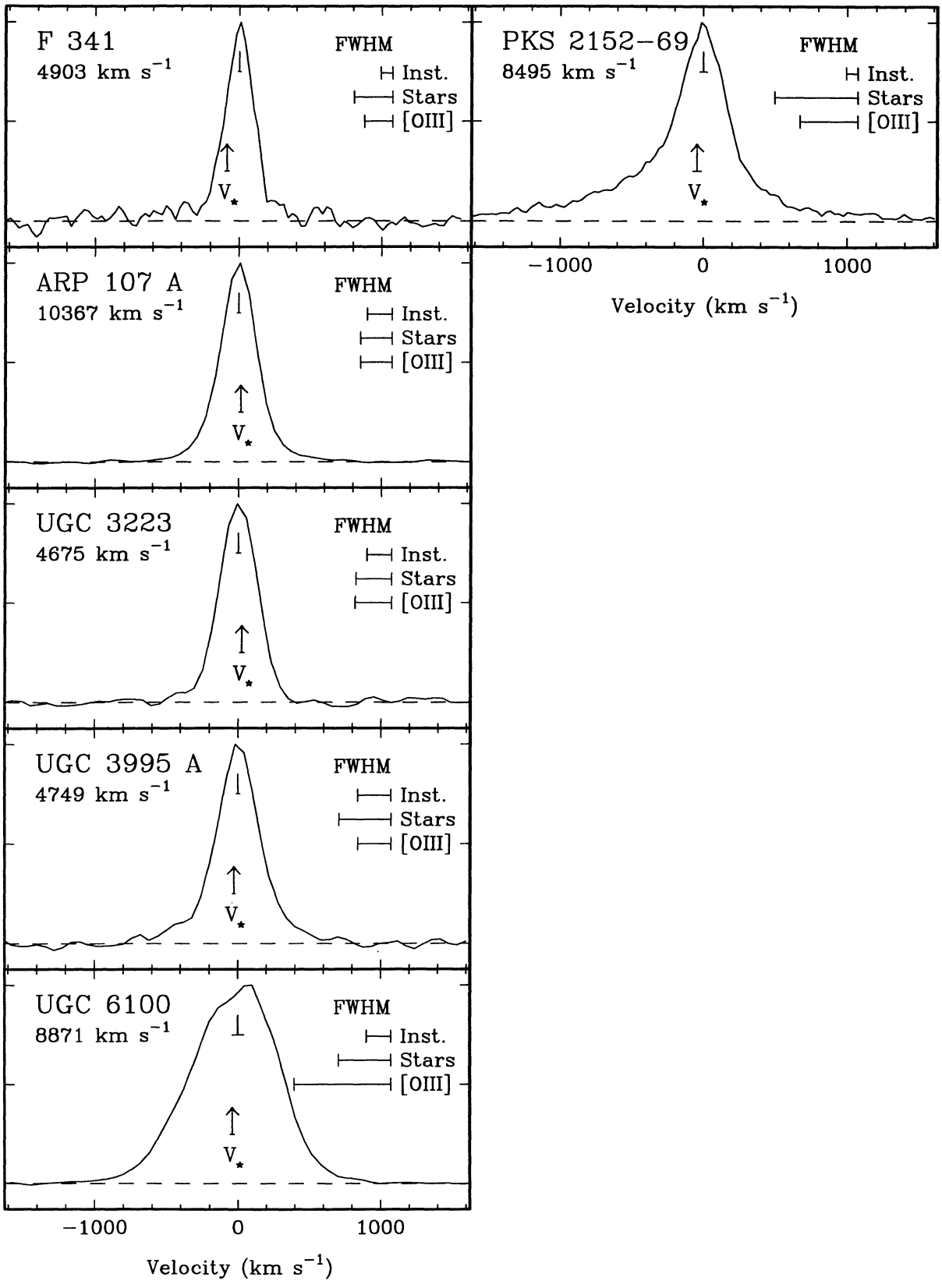

FIG. 8—*Continued*

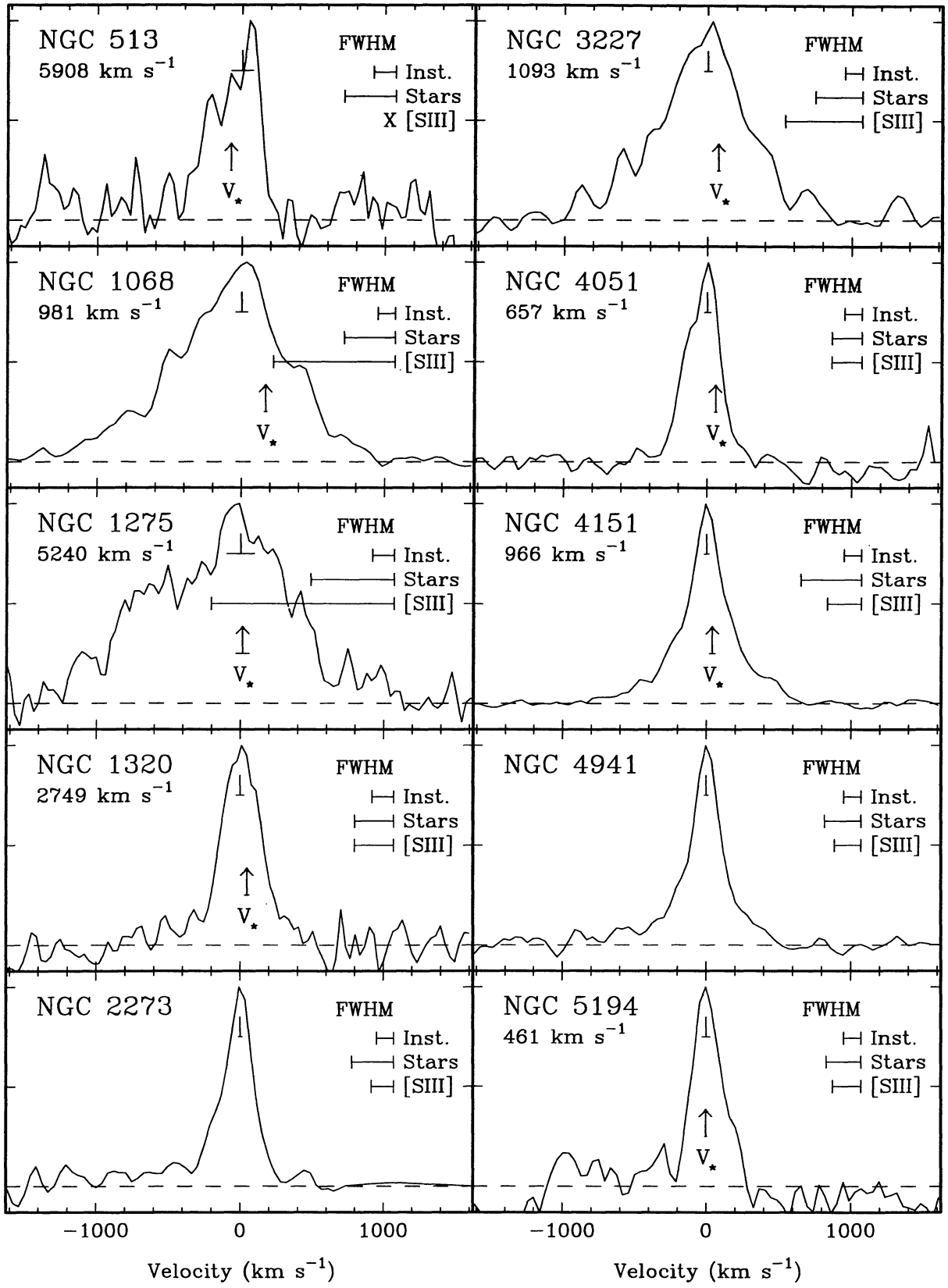

FIG. 9.—[S III] λ9069 emission-line profiles (see Fig. 8 for a description of the layout)

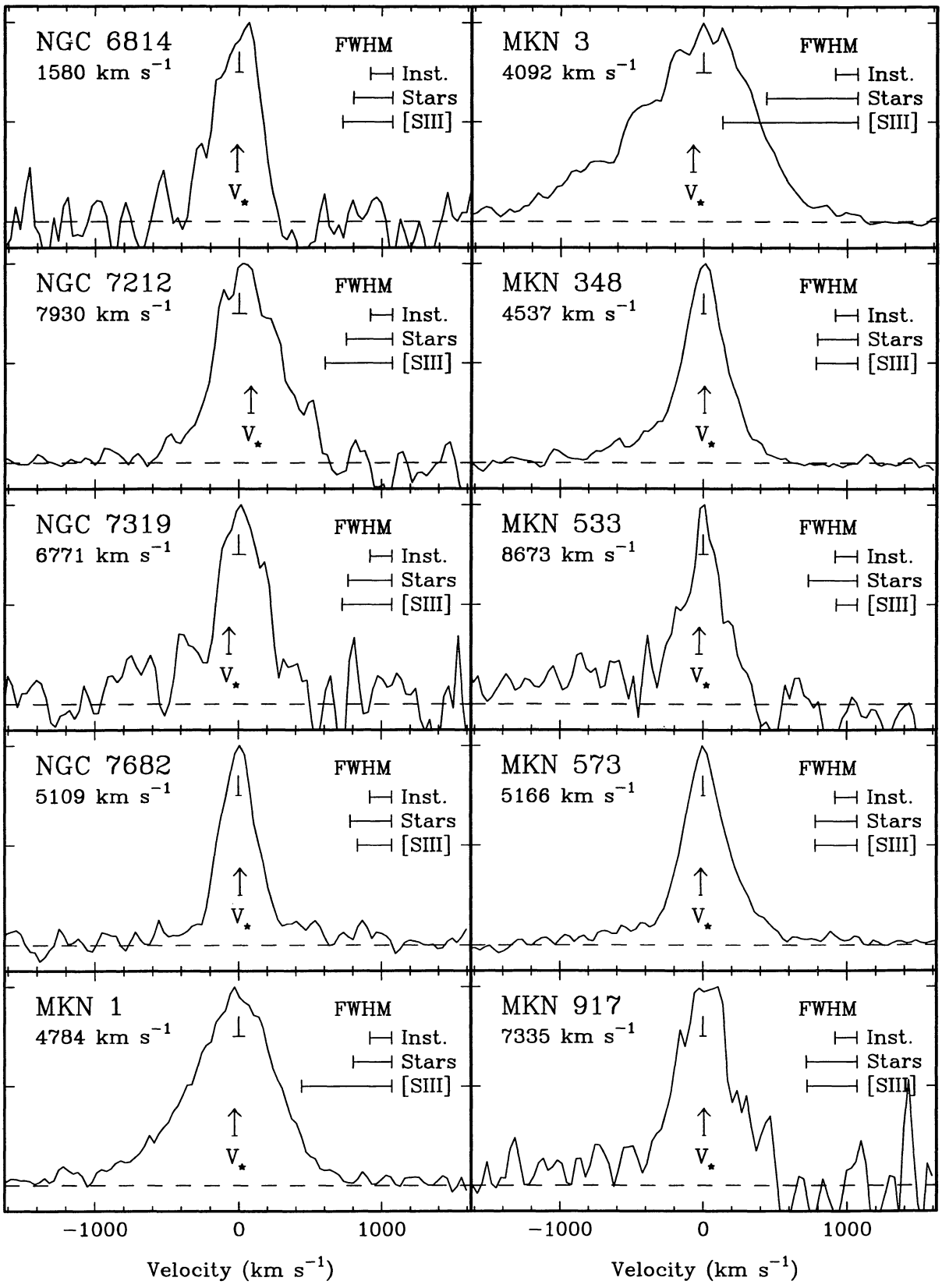

FIG. 9—*Continued*

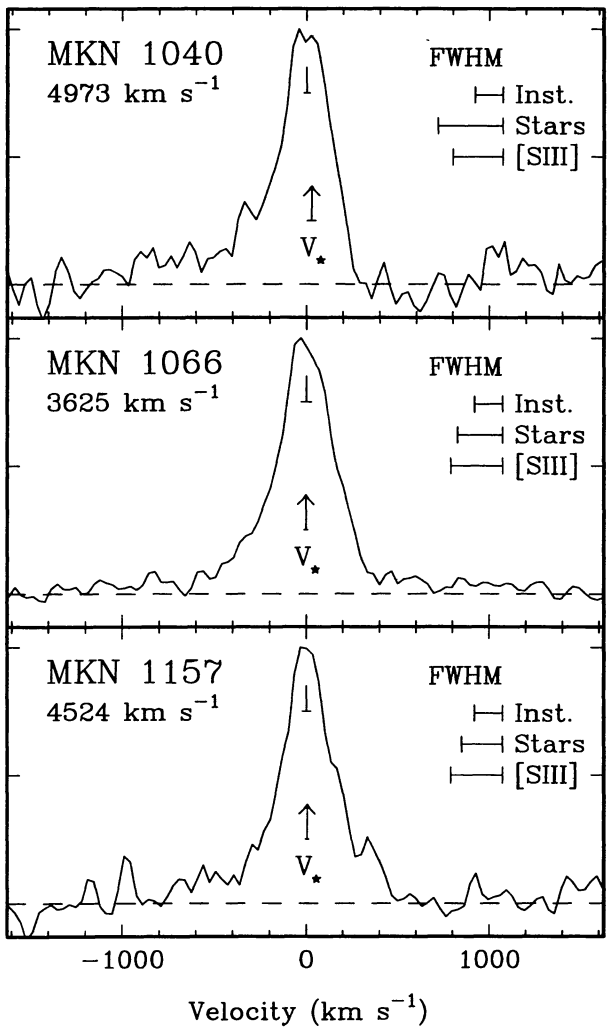

FIG. 9—*Continued*

These artificial spectra were also used to calibrate our error analysis by fixing the value of B in equation (9) for each spectral region and observing setup. This was done by requiring, at a given value of R, the standard deviations of $V_{out} - V_{in}$ and $\sigma_{out} - \sigma_{in}$ to match the estimated value of ΔV_* and $\Delta\sigma_*$ in equations (9) and (10). We also note that including the factor f_w gave a better match between the estimated errors and the distribution of residuals in the simulated data sets, for both redshift and velocity dispersion.

We made several independent checks that the derived values of V_* and σ_* give good fits to the data. A broadened and shifted cross-correlation of two templates was fitted to the galaxy-template cross-correlation. The minimum χ^2 gave values of V_* and σ_* in excellent agreement with our basic method. We also find good agreement in V_* and σ_* for a subset of our sample measured using the IRAF tasks FXCOR in the RV package and XCOR in STSDAS. The AAT spectra were also measured using a Fourier quotient method, again giving good agreement.

We have also compared independent observations of the same objects. Figure 6 shows the Ca II triplet velocity dispersion plotted against the Mg b velocity dispersion for galaxies observed in both spectral regions. Although there are a few disagreements for the lower quality data, (e.g., "c"; see below), overall the values agree to within their estimated errors. Figure 7 shows our adopted velocity dispersion (see below) plotted against previously published values for the same objects. We find overall agreement with a few differences. These may be caused by differences in aperture placement, particularly for the large elliptical galaxies where published work can often sum more than 10″ along the slit. Despite overall agreement with the results of Terlevich, Diaz, & Terlevich (1990), there are a few puzzling differences which we note in the Appendix.

4.7. *Final Values*

Table 2 presents the results of our velocity dispersion analysis. Column (2) gives our finally adopted σ_*, its error, and data quality rating (see below). In each spectral region we give our measured velocity dispersion and error (cols. [3] and [9]), the observing run number from Table 2 (cols. [4] and [10]), the rectangular aperture size (cols. [5] and [11]), the slit position angle (cols. [6] and [12]), and an estimate of the seeing (cols. [8] and [13]; see § 3). The combined velocity dispersions, errors and quality ratings given in column (15) were calculated either by taking a weighted average of our Ca II triplet and Mg b values when both data qualities were acceptable, or by simply taking the better quality result. In column (16) we have included previously published velocity dispersions and errors from the literature and, if possible, a quality rating. The primary sources of published σ_* are Whitmore, McElroy, & Tonry (1985) and Terlevich et al. (1990).

The quality ratings assigned are an indicator of the relative reliability of the dispersion values: "a" for reliable values, "b" for less reliable though probably adequate values, "c" for values of poor quality and of dubious usefulness, and "r" for rejected, highly unreliable values. For single observations, the initial quality ratings are based on the signal-to-noise parameter R and fractional errors $e = \Delta\sigma_*/\sigma_*$. These are then adjusted depending on data problems not reflected in the R- and e-values, such as strong emission-line contamination, suspected Ca II triplet emission, and bad cosmic-ray or sky-subtraction features at critical wavelengths. We have attempted to assess the data quality for dispersions taken from the literature, on the basis of published spectra and errors. A quality of "b?" is given if neither an error estimate nor a spectrum is available. When independent values are combined (e.g., Ca II triplet and Mg b regions, or ours and published values), a weighted average has been taken and the better quality rating has been adopted unless the values differ by more than $2^{1/2}$ times the largest error. In this case the quality rating is reduced by one step and the error is taken to be $2^{-1/2}$ times the difference between the two values. The finally adopted values listed in Table 2 are our best estimate for the nuclear velocity dispersion based on the available data.

5. MEASUREMENT OF GASEOUS KINEMATICS

5.1. *Emission-Line Profiles*

In addition to providing measurements of stellar kinematics from absorption lines, our spectra also contain emission lines

TABLE 3

SEYFERT [O III] and [S III] LINE WIDTHS

	Name	Adopted [OIII] FWHM	Adopted [OIII] FW20	Adopted [OIII] IPV20	Adopted [OIII] IPV10	Our [OIII] FWHM	Our [OIII] FW20	Our [OIII] IPV20	Our [OIII] IPV10	[SIII] FWHM	[SIII] FW20	[SIII] IPV20	[SIII] IPV10	[OIII] Ref.
		km s^{-1}				km s^{-1}				km s^{-1}				
	(1)	(2)	(3)	(4)	(5)	(6)	(7)	(8)	(9)	(10)	(11)	(12)	(13)	(14)
1	NGC 513	220 b	430 b	357 b	498 b	220 b	430 b	357 b	498 b	–	–	–	–	...
2	NGC 788	190 a	295 a	225 a	305 a	190 a	295 a	225 a	305 a	...	...	...	...	25
3	NGC 1052	770 a	1085 a	810 a	1075 a	770 a	1085 a	810 a	1075 a	...	...	...	...	...
4	NGC 1068	1060 b	1860 a	1485 a	1980 a	...	...	...	...	851 b	1508 b	1123 b	1427 b	10,22
5	NGC 1275	1360 a	2400 a	...	...	...	...	...	...	1275 b	1539 b	1086 b	1293 c	12
6	NGC 1320	229 b	387 b	301 b	413 b	229 b	387 b	301 b	413 b	274 b	395 b	282 c	369 c	4
7	NGC 1358	220 a	410 a	355 a	505 a	220 a	410 a	355 a	505 a	...	...	...	...	25,17
8	NGC 1386	325 b	625 b	510 a	695 a	315 b	625 b	510 a	695 a	...	...	...	...	25,17
9	NGC 1566	280 a	440 a	450 a	720 b	...	...	...	...	...	...	...	...	25
10	NGC 1667	275 c	410 c	365 b	525 c	...	...	...	...	...	...	...	...	25,17,8
11	NGC 2110	420 b	710 b	655 a	950 a	295 b	645 b	655 a	950 a	...	...	...	...	25,22
12	NGC 2273	110 a	210 a	260 a	370 a	165 b	288 b	250 b	355 b	158 b	348 b	254 b	325 b	25,27
13	NGC 2841	509 c	...	...	...	...	...	...	...	–	–	–	–	11
14	NGC 2992	245 b	470 b	565 b	790 b	257 b	608 b	592 b	814 b	...	...	...	...	24,25,12,2
15	NGC 3031	335 b	...	...	...	...	...	...	...	–	–	–	–	7
16	NGC 3185	146 b	258 b	232 b	333 b	146 b	258 b	232 b	333 b	...	...	...	...	8,14
17	NGC 3227	485 a	830 a	700 a	987 b	529 b	879 b	707 b	984 b	536 b	1151 b	775 b	994 b	24,23,22
18	NGC 3362	369 b	658 b	546 b	770 b	369 b	658 b	546 b	770 b	...	...	...	...	...
19	NGC 3516	250 a	550 a	490 a	665 b	...	...	...	...	...	...	...	...	25,23
20	NGC 3786	185 a	475 a	464 b	663 b	260 b	503 b	463 b	651 b	...	...	...	...	25
21	NGC 3982	203 b	358 b	315 b	452 b	203 b	358 b	315 b	452 b	...	...	...	...	...
22	NGC 3998	630 b	1498 b	1166 c	1535 c	630 b	1498 b	1166 c	1535 c	...	...	...	...	1,13,11
23	NGC 4051	190 a	315 a	395 b	630 b	230 b	442 b	454 b	741 b	208 b	353 b	293 c	405 c	25,22
24	NGC 4117	189 b	301 b	223 b	289 b	189 b	301 b	223 b	289 b	...	...	...	...	...
25	NGC 4151	425 b	700 b	610 b	940 b	...	...	...	...	233 b	575 b	536 c	774 c	12,23,3,22
26	NGC 4339	...	...	...	...	...	...	...	...	...	...	...	...	...
27	NGC 4388	205 b	405 b	400 a	580 a	224 b	506 b	474 b	648 b	...	...	...	...	12,22
28	NGC 4579	653 b	1278 b	920 c	1143 c	653 b	1278 b	920 c	1143 c	...	...	...	...	13
29	NGC 4593	255 a	440 a	363 b	511 b	260 b	448 b	367 b	507 b	...	...	...	...	25
30	NGC 4941	226 b	411 b	347 b	493 b	226 b	411 b	347 b	493 b	183 b	405 b	358 b	501 b	20
31	NGC 5194	190 b	310 b	...	...	...	...	...	...	195 c	364 c	–	–	9
32	NGC 5252	510 b	725 b	620 a	890 a	454 b	638 b	496 b	692 b	...	...	...	...	25
33	NGC 5273	130 a	265 a	295 a	455 a	165 c	301 b	253 b	356 b	...	...	...	...	25
34	NGC 5347	392 b	677 b	513 a	679 a	392 b	677 b	513 a	679 a	...	...	...	...	...
35	NGC 5427	264 b	620 b	659 a	956 a	264 b	620 b	659 a	956 a	...	...	...	...	14
36	NGC 5548	410 a	665 a	525 a	730 a	415 b	672 b	571 b	835 b	...	...	...	...	24,25,23,22
37	NGC 5929	415 a	510 a	410 a	485 a	405 b	576 b	412 b	514 b	...	...	...	...	25,26
38	NGC 5940	386 b	733 b	680 b	1001 b	386 b	733 b	680 b	1001 b	–	–	–	–	...
39	NGC 5953	310 b	638 b	511 b	679 b	310 b	638 b	511 b	679 b	–	–	–	–	14,18
40	NGC 6104	169 c	346 b	305 b	427 b	169 c	346 b	305 b	427 b	–	–	–	–	...
41	NGC 6482	...	...	...	...	...	...	...	...	–	–	–	–	...
42	NGC 6702	...	...	...	...	...	...	...	...	...	...	...	...	...
43	NGC 6703	...	...	...	...	...	...	...	...	–	–	–	–	...
44	NGC 6814	125 a	315 a	275 b	400 b	...	...	...	...	350 c	506 c	–	–	24,23,2
45	NGC 7212	435 a	660 a	520 a	735 a	...	...	...	...	471 c	817 c	555 c	741 c	25
46	NGC 7213	990 a	1550 a	1155 a	1570 b	990 a	1550 a	1155 a	1570 b	...	...	...	...	...
47	NGC 7319	276 b	435 b	384 b	570 b	276 b	435 b	384 b	570 b	348 c	–	–	–	5
48	NGC 7603	448 b	709 b	666 b	931 b	448 b	709 b	666 b	931 b	–	–	–	–	25
49	NGC 7672	297 b	535 b	354 b	477 c	297 b	535 b	354 b	477 c	–	–	–	–	...
50	NGC 7682	255 a	410 a	390 a	640 a	...	...	...	...	239 b	363 b	266 c	330 c	25
51	NGC 7743	220 b	480 b	345 a	435 a	220 b	480 b	345 a	435 a	...	...	...	...	...
52	MKN 1	520 a	995 a	820 a	1080 a	...	...	...	...	633 b	1025 b	750 c	972 c	23
53	MKN 3	850 a	1370 a	1050 a	1385 a	...	...	...	...	940 b	1535 b	1111 b	1410 b	25,12,23,22
54	MKN 6	475 b	1170 a	1140 a	1565 a	...	...	...	...	...	...	...	...	25,12,23,27
55	MKN 10	360 a	520 a	391 b	501 b	345 b	540 b	391 b	501 b	...	...	...	...	12
56	MKN 78	1075 a	1485 a	1155 a	1370 a	1120 b	1539 b	1169 b	1389 b	...	...	...	...	25,12,27
57	MKN 176	490 a	1112 a	938 a	1276 a	528 b	1124 a	938 a	1276 a	...	...	...	...	12
58	MKN 270	370 a	580 a	530 a	790 b	396 b	620 b	472 b	637 b	...	...	...	...	12,23,27,25
59	MKN 348	365 b	630 b	649 a	960 a	363 b	660 b	649 a	960 a	288 b	571 b	543 b	770 c	25,6,5
60	MKN 372	400 c	...	...	...	...	...	...	...	...	...	...	...	15
61	MKN 506	430 b	...	...	...	...	...	...	...	–	–	–	–	6
62	MKN 533	350 a	960 a	1255 a	1640 a	...	...	...	...	146 c	449 c	–	–	25,22,21
63	MKN 573	190 a	480 a	450 a	630 a	...	...	...	...	290 b	540 b	423 b	572 b	25,27
64	MKN 590	400 a	670 a	555 b	765 b	...	...	...	...	–	–	–	–	23
65	MKN 622	1158 b	1555 b	1039 b	1275 b	1158 b	1555 b	1039 b	1275 b	...	...	...	...	19
66	MKN 686	359 b	609 b	454 b	593 b	359 b	609 b	454 b	593 b	...	...	...	...	...
67	MKN 766	180 a	425 a	455 a	660 a	266 b	517 b	482 b	703 b	...	...	...	...	22
68	MKN 917	352 b	801 b	888 a	1333 a	352 b	801 b	888 a	1333 a	349 c	–	–	–	...
69	MKN 1018	330 a	585 a	490 a	670 a	330 a	585 a	490 a	670 a	...	...	...	...	25
70	MKN 1040	305 b	470 b	395 a	540 a	...	...	...	...	274 b	558 b	373 c	463 c	23

TABLE 3—*Continued*

	Name	Adopted [OIII] FWHM	FW20	IPV20	IPV10	Our [OIII] FWHM	FW20	IPV20	IPV10	[SIII] FWHM	FW20	IPV20	IPV10	[OIII] Ref.
		km s^{-1}				km s^{-1}				km s^{-1}				
	(1)	(2)	(3)	(4)	(5)	(6)	(7)	(8)	(9)	(10)	(11)	(12)	(13)	(14)
71	MKN 1066	405 a	720 a	660 a	915 a	417 b	714 b	640 b	902 b	283 c	542 c	–	–	22
72	MKN 1126	190 b	300 b	285 a	485 b	155 b	290 b	285 a	485 b	...	...	...	...	25,3
73	MKN 1157	235 a	450 a	505 a	790 a	283 b	551 b	542 b	826 b	282 b	475 b	366 b	519 c	22
74	AKN 79	355 a	800 c	650 b	860 b	...	...	...	...	–	–	–	–	23
75	AKN 347	310 b	519 b	448 b	648 b	310 b	519 b	448 b	648 b	...	...	...	...	6
76	IC 5063	335 b	510 b	425 b	610 b	345 b	485 b	370 b	505 b	...	...	...	...	24,25,2
77	III ZW 55 N	595 b	1220 b	...	...	...	...	...	...	...	...	...	...	16
78	MCG 8-11-11	605 a	1005 a	885 a	1340 a	...	...	...	...	...	...	...	...	25,27
79	F 341	195 a	330 a	260 a	360 a	195 a	330 a	260 a	360 a	...	...	...	...	25
80	ARP 107 A	219 b	377 b	320 b	459 b	219 b	377 b	320 b	459 b	...	...	...	...	...
81	UGC 3223	255 b	383 b	279 b	367 b	255 b	383 b	279 b	367 b	...	...	...	...	...
82	UGC 3995 A	232 b	424 b	380 b	569 b	232 b	424 b	380 b	569 b	...	...	...	...	...
83	UGC 6100	679 c	1029 c	742 c	953 c	679 c	1029 c	742 c	953 c	...	...	...	...	...
84	3C 120	230 b	380 b	475 a	780 a	...	...	...	...	...	...	...	...	25,12,23
85	PKS 2152-69	400 a	950 a	1230 a	1920 a	400 a	950 a	1230 a	1920 a	...	...	...	...	...

Col. (1): Name. Cols. (2)–(5): Adopted [O III] λ5007 line width for the core (FWHM), the base (FW20, IPV20), and the wings (IPV10). Cols. (6)–(9): Line width parameters for the [O III] profiles presented in this paper. Cols. (10)–(13): Line width parameters for the [O III] profiles presented in this paper. Col. (14): Reference for published [O III] profile data used in obtaining the adopted values in cols. (2)–(5); usually these are the same as given in W92a.

REFERENCES.—(1) Bertola et al. 1984; (2) Busko & Steiner 1988; (3) De Robertis & Osterbrock 1984; (4) De Robertis & Osterbrock 1986a; (5) De Robertis & Osterbrock 1986b; (6) Feldman et al. 1982; (7) Filippenko & Sargent 1988; (8) Filippenko & Sargent 1985; (9) Ford et al. 1985; (10) Glaspey et al. 1976; (11) Heckman, Balick, & Crane 1980; (12) Heckman, Miley, & Green 1984; (13) Keel 1983; (14) Keel et al. 1985; (15) Koski 1978; (16) Laurikainen & Moles 1988; (17) Phillips, Charles, & Baldwin 1983; (18) Rafanelli, Osterbrock, & Pogge 1990; (19) Shuder & Osterbrock 1981; (20) Stauffer 1982; (21) Unger et al. 1988; (22) Veilleux 1991b; (23) Vrtilek & Carleton 1985; (24) Whittle 1985; (25) Whittle 1992a; (26) Whittle et al. 1986; (27) Whittle et al. 1988.

which provide measurements of ionized gas kinematics. Figure 8 displays the continuum-subtracted [O III] λ5007 emission-line profiles. To allow direct comparison with the stellar velocities, we have extracted the same nuclear spatial channels as used in the absorption-line analysis (see Table 2). To correct for underlying stellar contribution, a high-quality spectrum of the elliptical galaxy NGC 4339 was shifted, scaled, broadened to match the stellar dispersion, and subtracted. The velocity scale zero point is taken to be the line-center parameter C80 (see below). Its heliocentric value is given on each plot and its position at the top of the profile is marked as a line with a base of width equal to its error. Similarly, the velocity of the stellar component, V_*, is marked as a vertical arrow with base width corresponding to its error. The three horizontal bars to the right of each profile show the FWHM of the instrumental profile, the resolution-corrected emission-line width (FWHM), and the (resolution-corrected) stellar velocity width from the cross-correlation analysis (FWHM = $2.35 \times \sigma_*$).

Most of the [O III] emission lines are of high signal-to-noise ratio, since our exposure times were determined by the need for adequate absorption-line data. Unfortunately, for those objects observed in runs 3–5 (KPNO 2.1 m; see Table 1) the resolution in the [O III] region is rather low for detailed profile work (FWHM ~ 170–230 km s^{-1}). Nevertheless, where higher resolution data exist (e.g., Vrtilek & Carleton 1985; Veilleux 1991a) there is good correspondence between features seen in our data and the higher resolution data.

Figure 9 displays the [S III] λ9069 emission-line profiles, using the same layout as for the [O III] lines in Figure 8. The atmospheric absorption bands have been removed as described in § 3. The [S III] profiles are generally of poorer quality than the [O III] profiles because of their weaker line strength, the effects of atmospheric absorption, and the lower efficiency of the telescope/detector system. Note that there is good qualitative agreement between the better [S III] profiles and the corresponding [O III] profiles from the same objects (e.g., NGC 1320, Mrk 348, Mrk 1157).

5.2. *Line Profile Parameters*

The [O III] and [S III] profile velocities and widths were measured using parameter schemes described in Heckman et al. (1981) and Whittle (1985). Profile velocities include C80, the center of a cut across the profile at 80% of the peak height, and C_{med}, the center of the profile area (i.e., the profile median). C80 is close to the peak velocity, although it is less sensitive to noise, while C_{med} gives the center of flux. Because of the poor continuum definition around ~9000 Å, C_{med} could not be measured reliably for [S III]. Errors on C80 and C_{med} were estimated following the methods described in Whittle (1985). Profile width parameters include FWHM and FW20, which are simple cuts across the profile at 50% and 20% of the peak height, and IPV10 and IPV20, which exclude 10% and 20% of the profile area from the blue and red wings. These width parameters yield measures of the core, base, wing, and base widths, respectively. The effects of finite instrument resolution have been corrected by subtracting the corresponding instrument profile parameter in quadrature. Although this works well for IPV10 and IPV20, it is somewhat less exact for FWHM and FW20 (Whittle 1985; see also below). Following the criteria given in W92a, we assign quality ratings to each line-width measurement. Except for the AAT data, our modest resolution usually requires quality ratings of "b" or worse.

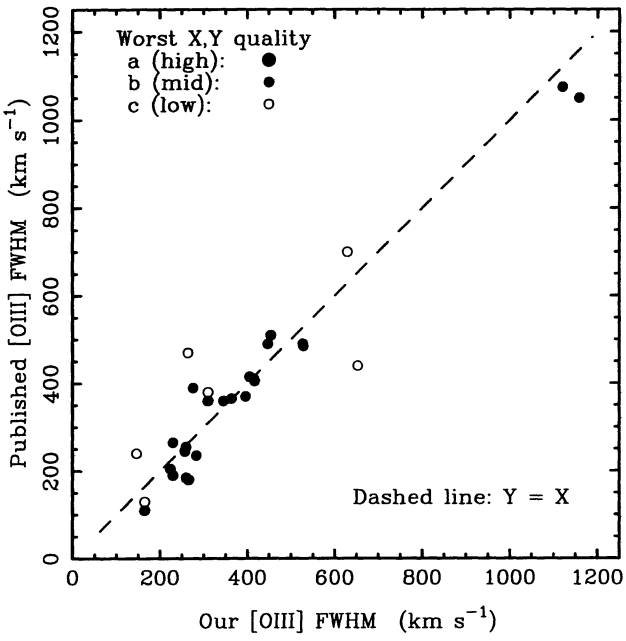

FIG. 10*a*

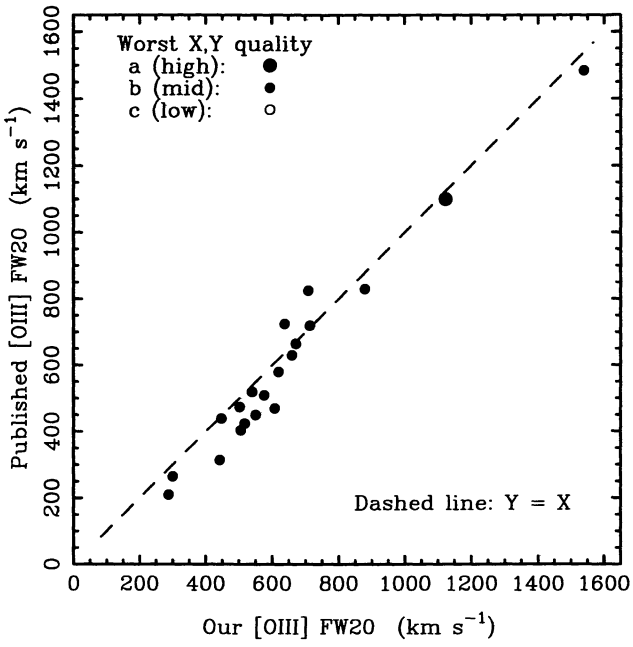

FIG. 10*b*

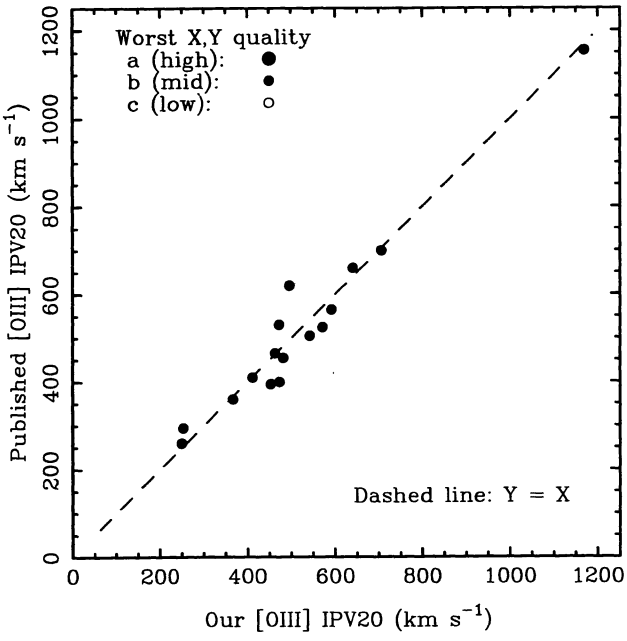

FIG. 10*c*

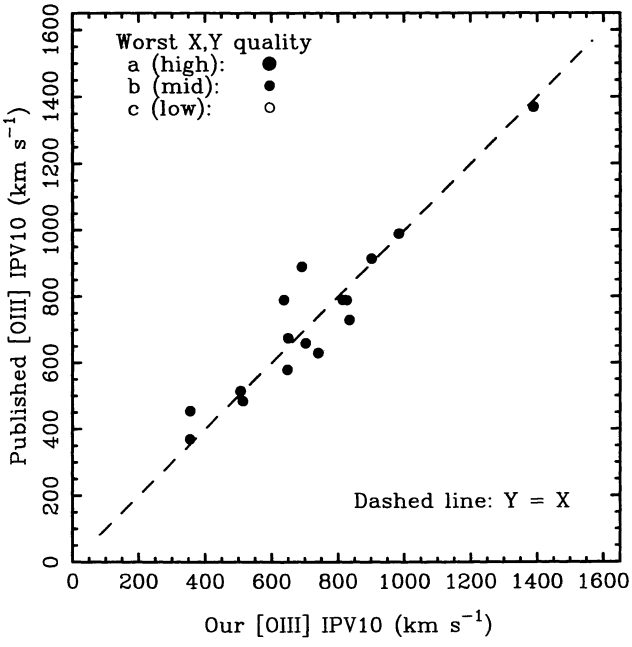

FIG. 10*d*

FIG. 10.—Emission-line width measurements for the data presented in this paper compared with published values. The lowest data-quality rating is indicated by the kind of point plotted. (*a*) FWHM; (*b*) FW20; (*c*) IPV20; and (*d*) IPV10. Overall, agreement is good, although there is a slight trend toward higher values of FWHM and FW20 for the narrower lines. This is consistent with the imperfect nature of quadrature subtraction as a resolution correction for the FWHM and FW20 parameters.

Table 3 gives the resolution-corrected line-width parameters for the [O III] profiles shown in Figure 8 (cols. [6]–[9]), and the [S III] profiles shown in Figure 9 (cols. [10]–[13]). Since many of the objects have been observed previously, often at higher resolution, we have combined our [O III] measurements with published values (taken principally from W92a), to give a final, adopted set of [O III] profile width parameters (cols. [2]–[5]). Data of equal quality are averaged; otherwise the data of the higher quality are taken. For this reason, most of the final adopted values come directly from W92a (note that

TABLE 4

REDSHIFTS: [O III], [S III], STARS, AND H I

	Name	[OIII] Med.	[OIII] C80	[SIII] C80	Stars Ca T	Stars Mg b	Stars Combined	Pub.	Ref.	HI cz	HI Profile	Ref.
	(1)	(2)	(3)	(4)	(5)	(6)	(7)	(8)	(9)	(10)	(11)	(12)
1	NGC 513	5772 ± 4	5779 ± 12	5908 ± 75	5825 ± 18	5831 ± 7	5830 ± 7	...	...	...	...	...
2	NGC 788	4061 ± 5	4062 ± 10	...	...	4047 ± 12	4047 ± 12	...	...	...	...	...
3	NGC 1052	1307 ± 19	1394 ± 55	...	...	1450 ± 15	1450 ± 15	...	...	1507 ± 5	1PA:	9
4	NGC 1068	...	...	981 ± 40	1149 ± 8	...	1149 ± 8	1227	28,11	1137 ± 3	2PS-WR:	9
5	NGC 1275	...	...	5240 ± 95	5253 ± 44	...	5253 ± 44	...	...	...	...	...
6	NGC 1320	2739 ± 2	2733 ± 13	2749 ± 28	2805 ± 9	2782 ± 11	2796 ± 16	...	...	...	...	...
7	NGC 1358	4008 ± 6	4006 ± 10	...	...	4050 ± 13	4050 ± 13	4018	24	...	...	...
8	NGC 1386	881 ± 6	822 ± 17	...	...	873 ± 15	873 ± 15	845	10	...	...	...
9	NGC 1566	...	...	...	...	...	...	1594	30	1496 ± 5	2PS-WB:	9
10	NGC 1667	...	...	...	...	...	...	4587	28	4547 ± 75	–	15
11	NGC 2110	2249 ± 6	2252 ± 12	...	...	2335 ± 20	2335 ± 20	...	...	...	...	...
12	NGC 2273	1929 ± 2	1939 ± 10	–	1880 ± 16	1895 ± 7	1893 ± 6	...	...	1840 ± 4	2PS	9
13	NGC 2841	...	...	–	649 ± 13	...	649 ± 13	635	24	638 ± 3	2PS	9
14	NGC 2992	2245 ± 5	2312 ± 13	...	2339 ± 18	2330 ± 10	2332 ± 9	2368	28	2314 ± 13	2PA	9,20,1
15	NGC 3031	...	...	–	−39 ± 9	...	−39 ± 9	−35	24	−34 ± 4	2PS	9,20
16	NGC 3185	1229 ± 4	1234 ± 10	...	...	1239 ± 8	1239 ± 8	...	...	1230 ± 4	2PS:	9
17	NGC 3227	1024 ± 3	1043 ± 17	1093 ± 25	1167 ± 9	1139 ± 12 r	1167 ± 9	1139	28	1157 ± 12	2PA	9
18	NGC 3362	8274 ± 3	8273 ± 15	...	...	8294 ± 15	8294 ± 15	...	...	8324 ± 10	2PS	9,4,16
19	NGC 3516	...	...	...	...	...	...	2638	28	2503 ± 75	–	3
20	NGC 3786	2707 ± 5	2690 ± 12	...	2699 ± 13	2715 ± 15	2706 ± 10	...	...	2723 ± 4	2PA:	9
21	NGC 3982	1155 ± 2	1173 ± 8	...	...	1132 ± 6	1132 ± 6	...	...	1109 ± 6	2PS	9
22	NGC 3998	985 ± 38	991 ± 25	...	1089 ± 25	1045 ± 18	1060 ± 15	1009 ± 23	29	1040 ± 50	1PS:	17
23	NGC 4051	622 ± 5	642 ± 18	657 ± 22	714 ± 8	693 ± 11 r	714 ± 8	...	...	725 ± 5	2PS	9
24	NGC 4117	981 ± 8	973 ± 20	...	...	984 ± 9	984 ± 9	...	...	...	...	...
25	NGC 4151	...	...	966 ± 17	1006 ± 18	...	1006 ± 18	959	28	995 ± 3	2PS	9
26	NGC 4339	...	...	...	...	1268 ± 8	1268 ± 8	1280 ± 18	29	...	...	...
27	NGC 4388	2507 ± 2	2462 ± 10	...	...	2515 ± 20	2515 ± 20	2608	28	2517 ± 10	2PS	9,15
28	NGC 4579	1334 ± 32	1435 ± 28	...	...	1533 ± 7	1533 ± 7	1533	32	1519 ± 6	2PS	9
29	NGC 4593	2447 ± 4	2463 ± 13	...	2544 ± 20	2461 ± 14 r	2544 ± 20	...	...	2492 ± 6	2PS	9
30	NGC 4941	1139 ± 4	1142 ± 10	–	1138 ± 9	1123 ± 8	1130 ± 6	...	...	1111 ± 7	2PS	9
31	NGC 5194	...	...	461 ± 25	459 ± 7	...	459 ± 7	474 ± 23	31	463 ± 3	2PA	9
32	NGC 5252	6865 ± 7	6857 ± 25	...	...	6918 ± 19	6918 ± 19	...	...	6946 ± 17	2PA:	2
33	NGC 5273	1078 ± 4	1090 ± 12	...	...	1090 ± 7	1090 ± 7	...	...	1100 ± 85	1PA:	5,1
34	NGC 5347	2295 ± 7	2334 ± 13	...	...	2398 ± 8	2398 ± 8	2428	28	2386 ± 20	2PS-WR:	21
35	NGC 5427	2733 ± 7	2753 ± 12	...	...	2729 ± 7	2729 ± 7	...	...	2621 ± 20	CPX	22,25
36	NGC 5548	4991 ± 2	5013 ± 12	...	...	5051 ± 29 r	–	...	...	5149 ± 14	1PA	9,20,1
37	NGC 5929	2550 ± 3	2593 ± 15	...	2511 ± 22	2490 ± 8	2492 ± 8	...	...	2561 ± 15	2PS	14
38	NGC 5940	10098 ± 22	10117 ± 25	–	10338 ± 73 r	10174 ± 33 r	10174 ± 33	...	...	10208 ± 6	2PS	9
39	NGC 5953	2009 ± 6	2049 ± 12	–	1994 ± 8	1995 ± 7	1995 ± 5	2009	28	1935 ± 10	1PA	19,1
40	NGC 6104	8319 ± 7	8306 ± 10	–	8447 ± 30 r	8447 ± 24	8447 ± 24	...	...	...	...	...
41	NGC 6482	...	...	–	3956 ± 23	...	3956 ± 23	3950	8	...	...	...
42	NGC 6702	...	...	...	...	4740 ± 14	4740 ± 14	...	...	...	...	...
43	NGC 6703	...	...	–	2374 ± 12	...	2374 ± 12	2370 ± 26	8	...	...	...
44	NGC 6814	...	...	1580 ± 27	1564 ± 12	...	1564 ± 12	...	...	1563 ± 4	2PS	9
45	NGC 7212	...	...	7930 ± 50	8011 ± 21	...	8011 ± 21	...	...	...	...	...
46	NGC 7213	1562 ± 12	1669 ± 45	...	...	1790 ± 10	1790 ± 10	...	...	1792 ± 27	2PS:	15,23
47	NGC 7319	6762 ± 4	6782 ± 10	6771 ± 45	6706 ± 22	6695 ± 27	6702 ± 17	...	...	6611 ± 8	1PS:	9
48	NGC 7603	8726 ± 14	8767 ± 18	–	8915 ± 37	8829 ± 29	8862 ± 61	...	...	8736 ± 20	–	27
49	NGC 7672	4037 ± 14	4031 ± 30	–	4069 ± 20	4010 ± 22	4042 ± 42	...	...	4045 ± 20	2PS:	16
50	NGC 7682	...	...	5109 ± 18	5117 ± 12	...	5117 ± 12	...	...	5120 ± 4	2PA	9
51	NGC 7743	1629 ± 6	1649 ± 13	...	...	1671 ± 8	1671 ± 8	...	...	1662 ± 30	2PS:	14
52	MKN 1	...	...	4784 ± 40	4754 ± 18	...	4754 ± 18	...	...	4855 ± 12	1PA	16
53	MKN 3	...	...	4092 ± 50	4019 ± 17	...	4019 ± 17	4077	28	3955 ± 15	CPX	20,13,1
54	MKN 6	...	...	...	–	...	–	...	...	5850 ± 10	1PS:-ab	9
55	MKN 10	8751 ± 4	8753 ± 13	...	...	8769 ± 23	8769 ± 23	...	...	8753 ± 25	2PS	13,1
56	MKN 78	11037 ± 2	10958 ± 22	...	11038 ± 19	11099 ± 16	11074 ± 43	11092	28	...	...	...
57	MKN 176	7936 ± 6	7981 ± 13	...	...	7997 ± 14	7997 ± 14	...	...	8214 ± 30	2PA:	13,33,1
58	MKN 270	3137 ± 3	3127 ± 17	...	...	3101 ± 9	3101 ± 9	...	...	...	...	...
59	MKN 348	4505 ± 3	4521 ± 13	4537 ± 15	4543 ± 12	4545 ± 15	4544 ± 9	4797	28	4535 ± 15	1PS	20,13,1
60	MKN 372	...	...	...	–	...	–	...	...	...	...	...
61	MKN 506	...	...	–	–	...	–	...	...	12900 ± 50	2PS:	9,5,1
62	MKN 533	...	...	8673 ± 32	8645 ± 23	...	8645 ± 23	...	...	8777 ± 10	1PA-ab	9,18,1
63	MKN 573	...	...	5166 ± 13	5150 ± 11	...	5150 ± 11	...	...	...	...	...
64	MKN 590	...	...	–	7988 ± 20	...	7988 ± 20	...	...	7910 ± 25	CPX	9,13,1
65	MKN 622	6915 ± 20	6946 ± 60	...	...	7036 ± 10	7036 ± 10	...	...	6964 ± 30	CPX	9,20,1
66	MKN 686	4251 ± 4	4279 ± 13	...	4238 ± 15	4264 ± 9	4257 ± 8	...	...	4225 ± 20	2PS:	9,20,1
67	MKN 766	3855 ± 2	3872 ± 13	...	...	–	–	...	...	...	...	...
68	MKN 917	7259 ± 5	7283 ± 15	7335 ± 22	7343 ± 17	7339 ± 15	7341 ± 11	...	...	7317 ± 24	1PA:	9,12,1
69	MKN 1018	12762 ± 6	12778 ± 15	...	...	12779 ± 20	12779 ± 20	...	...	...	...	...
70	MKN 1040	...	...	4973 ± 17	4999 ± 22	...	4999 ± 22	...	...	4993 ± 7	2PS	9

TABLE 4—*Continued*

	Name	[OIII] Med.	[OIII] C80	[SIII] C80	Stars Ca T	Stars Mg b	Stars Combined	Pub.	Ref.	HI cz	HI Profile	HI Ref.
	(1)	(2)	(3)	(4)	(5)	(6)	(7)	(8)	(9)	(10)	(11)	(12)
71	MKN 1066	3523 ± 5	3567 ± 15	3625 ± 28	3619 ± 13	3628 ± 16	3623 ± 10	...	...	...	...	...
72	MKN 1126	3145 ± 6	3155 ± 8	...	...	3170 ± 15	3170 ± 15	...	...	3191 ± 11	2PA	9
73	MKN 1157	4498 ± 4	4501 ± 12	4524 ± 23	4528 ± 12	4527 ± 12	4528 ± 8	...	...	4554 ± 14	2PS	9,13,1
74	AKN 79	...	...	–	5225 ± 14	...	5225 ± 14	...	...	...	...	...
75	AKN 347	6820 ± 5	6834 ± 13	...	...	6798 ± 18	6798 ± 18	...	...	...	...	...
76	IC 5063	3432 ± 6	3422 ± 23	...	...	3410 ± 10	3410 ± 10	...	...	3380 ± 16	2PA	9,7
77	III ZW 55 N	...	...	...	–	...	–	7705	28	...	...	...
78	MCG 8-11-11	...	...	...	6118 ± 33 r	...	–	...	...	6147	...	20
79	F 341	4896 ± 5	4903 ± 10	...	...	4817 ± 15	4817 ± 15	...	...	...	...	...
80	ARP 107 A	10366 ± 3	10367 ± 13	...	...	10382 ± 14	10382 ± 14	...	...	10446	...	6
81	UGC 3223	4671 ± 6	4675 ± 15	...	...	4698 ± 18	4698 ± 18	...	...	...	...	...
82	UGC 3995 A	4746 ± 6	4749 ± 12	...	...	4721 ± 10	4721 ± 10	...	...	4747 ± 50	CPX	9
83	UGC 6100	8852 ± 5	8871 ± 40	...	...	8832 ± 17	8832 ± 17	...	...	8718 ± 30	2PA:	9,20,1
84	3C 120	...	...	...	–	...	–	10013	26	9900 ± 50	...	...
85	PKS 2152-69	8440 ± 6	8495 ± 25	...	...	8450 ± 30	8450 ± 30	...	...	...	...	...

Col. (1): Name. Cols. (2)–(3): [O III] profile median and C80 redshifts and their errors. Col. (4): [S III] C80 redshift. Cols. (5)–(6): Ca II triplet and Mg *b* redshifts and their errors. Col. (7): Combined stellar redshift. Cols. (8)–(9): Published stellar redshift and reference. Cols. (10)–(12): H I 21 cm redshift, profile type (see text), and reference. (*Note:* All redshifts are heliocentric *cz* and are expressed in km s^{-1}.)

REFERENCES.—(1) Error estimated from H I profile; (2) Axon et al. 1995; (3) Balkowski et al. 1972; (4) Bicay & Giovanelli 1986; (5) Bieging & Biermann 1983; (6) Bushouse 1987; (7) Danziger, Goss, & Wellington 1981; (8) Davies et al. 1987; (9) de Vaucouleurs et al. 1991 (RC3); (10) Dressler & Sandage 1983; (11) Dressler 1984; (12) Giovanelli & Haynes 1985; (13) Heckman, Balick, & Sullivan 1978; (14) Huchtmeier 1982; (15) Huchtmeier & Richter 1989; (16) Hutchings 1989; (17) Knapp, van Driel, & van Woerden 1985; (18) Mirabel 1982; (19) Mirabel & Sanders 1988; (20) Mirabel & Wilson 1984; (21) Peterson 1979; (22) Peterson & Shostak 1974; (23) Reif et al. 1982; (24) Schechter 1983; (25) Shostak 1978; (26) Smith, Heckman, & Illingworth 1990; (27) Sulentic & Arp 1983; (28) Terlevich, Diaz, & Terlevich 1990; (29) Tonry & Davis 1981; (30) van der Kruit & Freeman 1984; (31) White et al. 1983; (32) Whitmore & Kirshner 1981; (33) Williams & Rood 1987.

the W92a compilation had already included the values from the AAT data, usually as quality "a").

Figure 10 compares our new [O III] line widths with those from the literature, mostly taken from W92a (excluding the AAT duplicate data, and Mrk 78, which has a peculiar double profile). Reasonably good agreement is found for all parameters, with rms scatter ~10%. There is some tendency, however, for our values of FWHM and FW20 to be slightly high for the narrowest lines. This is consistent with the imperfect nature of the resolution corrections. For the narrowest lines, quadrature subtraction systematically overestimates the corrected values of FWHM and FW20 (e.g., Whittle 1985; Veilleux 1991b). Interestingly, no such offsets are seen for the IPV10 and IPV20 parameters, as expected from the analysis of resolution corrections by Whittle (1985).

6. REDSHIFTS

In addition to line widths, our data provide a number of measures of nuclear redshift, both gaseous and stellar. Table 4 includes our measurements of C80 and C_{med} for [O III] and C80 for [S III] (cols. [2]–[4]), as well as stellar velocities from

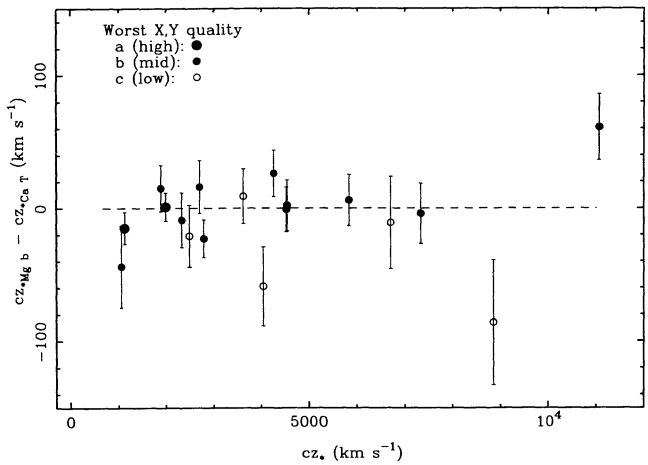

FIG. 11.—Difference between Mg *b* and Ca II triplet stellar velocities, plotted against redshift. The lowest data-quality rating is indicated by the kind of point plotted. There is excellent agreement, with most values falling within their estimated errors.

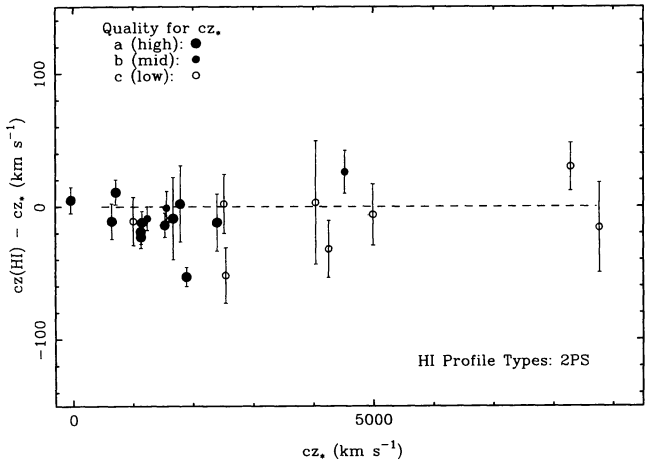

FIG. 12.—Difference between our stellar velocities and published H I 21 cm velocities for 2PS H I profiles (see § 6), plotted against redshift. The data-quality rating for cz_* is indicated by the kind of point plotted. There is good agreement, with most values falling within their estimated errors.

TABLE 5

SEYFERT GALAXY ROTATION AND INCLINATION

	Name	Type	ΔV_{HI}	ΔV_{opt}	ΔV_{rot}	ΔV^c_{rot}	i	Refs.	Refs.	Refs.
			km s^{-1}				deg.	ΔV_{HI}	ΔV_{opt}	i
	(1)	(2)	(3)	(4)	(5)	(6)	(7)	(8)	(9)	(10)
1	NGC 513	2.0	...	...	...	...	63a	...	...	5
2	NGC 1275	1.5	...	...	...	...	...	...	...	...
3	NGC 3362	2.0	215a	...	215a	334a	40a	12	...	5
4	NGC 3982	2.0	234a	...	234a	468c	30a	5	...	5
5	NGC 4117	2.0	...	...	...	...	63b	...	...	5
6	NGC 4941	2.0	319a	...	319a	372a	59a	10,7	...	5
7	NGC 5194	2.5	195a	170a	183a	534c	20b	6	9	9
8	NGC 5347	2.0	144a	...	144a	234b	38b	14	...	5
9	NGC 5427	1.9	430r	162b	162b	306b	32a	15	2	15
10	NGC 5940	1.2	208a	...	208a	608c	~0	3,13	...	5
11	NGC 5953	2.0	261r	...	–	–	35r	3	...	5
12	NGC 6104	2.0	...	...	...	...	...	...	...	...
13	NGC 7672	2.0	225b	...	225b	336b	42a	12	...	5
14	MKN 686	2.0	373c	...	373c	519d	46b	13,3	...	5
15	MKN 917	2.0	230c	...	230c	614e	22a	3,8	...	5
16	ARP 107 A	2.0	399r	...	–	–	...	4	...	...
17	UGC 3223	1.2	...	...	...	...	58b	...	...	5
18	UGC 3995 A	2.0	464r	...	–	–	64r	11,3	...	5,11
19	UGC 6100	2.0	375c	...	375c	490c	50a	13	...	5
20	3C 120	1.0	...	300c	300c	362d	56b	...	1	1

NOTE.—Table 5 follows the format of Table 2 in W92a for additional objects not included in that earlier sample.

Col. (1): Name. Col. (2): Seyfert type. Col. (3): Galaxy rotation amplitude from H I observations. Col. (4): Galaxy rotation amplitude from optical observations. Col. (5): Adopted galaxy rotation amplitude. Col. (6): Adopted inclination-corrected rotation amplitude. Col. (7): Galaxy inclination (in degrees; 0 = face-on). Cols. (8)–(11): References for data in col. (3)–(7). (*Note:* Units are km s^{-1} for cols. [3]–[5]. Quality factors [a = good, b = fair, c = poor, r = reject] are defined in more detail in Table 1 of W92a.)

REFERENCES.—(1) Baldwin et al. 1980; (2) Blackman 1982; (3) Bottinelli, Gouguenheim, Fouqué, & Paturel 1990; (4) Bushouse 1987; (5) de Vaucouleurs et al. 1991 (RC3); (6) Fisher & Tully 1981; (7) Giovanelli & Haynes 1983; (8) Giovanelli & Haynes 1985; (9) Goad, De Veny, & Goad 1979; (10) Huchtmeier 1982; (11) Huchtmeier & Richter 1989; (12) Hutchings 1989; (13) Mirabel & Wilson 1984; (14) Peterson 1979; (15) Peterson & Shostak 1974.

the Ca II triplet and Mg *b* regions (cols. [5]–[6]; note that all velocities are given as heliocentric cz). Highly unreliable values, due to low signal-to-noise ratio or contamination by emission, are marked "r" for "reject." If both Ca II triplet and Mg *b* values are usable, a weighted mean defines a "combined" value which is given in column (7). Columns (8) and (9) contain published absorption-line velocities and their reference. Figure 11 shows the difference between the velocities measured in the Ca II triplet and in the Mg *b* regions. Agreement is good, with mean $\sim -7 \pm 8$ km s^{-1} and rms scatter ~ 32 km s^{-1} ($\sim 2 \pm 7$ km s^{-1} and ~ 25 km s^{-1}, excluding quality "c" measurements), consistent with our error estimates for the individual measurements.

To help compare our measurements with other estimates of the galaxy systemic velocity, we have gathered H I data from the literature. The heliocentric H I velocity (line center, with error) and reference are given in columns (10) and (12). Most H I values were taken from de Vaucouleurs et al. (1991, hereafter RC3); these were originally compiled by Bottinelli et al. (1990). Cross-checking these values using the compilation of Huchtmeier & Richter (1989) suggests that the RC3 errors are frequently smaller than those given in the original observational papers, even for single measurements. In a number of cases, therefore, we have given what we feel to be more realistic errors, using the original published values when available or our own estimates from published H I profiles.

Since reliable H I systemic velocities can only be obtained from relatively isolated undistorted galaxies, we have attempted to classify the H I profile shapes for as many objects as possible, using published H I profiles. Only symmetric two-peaked profiles are likely to give clean estimates of systemic velocity. We have built on the profile classification scheme described by Heckman, Balick, & Sullivan (1978), namely, 2PS and 1PS for double-peaked and single-peaked symmetric profiles; 2PA and 1PA for double-peaked and single-peaked asymmetric profiles; CPX for complex profiles; -ab designates H I in absorption; -WR and -WB designate red and blue wings. A colon indicates an uncertain classification, and a dash indicates that no H I profile was available. Our classifications are given in column (11).

Figure 12 compares our "adopted" stellar velocity with the H I systemic velocities, for H I profiles classified as 2PS. Over-

TABLE 6

SEYFERT MORPHOLOGY AND LUMINOSITY

	Name	Type	T	DC, IAC	B_T	Δm_A	Δm_K	Δm_i	Δm_G	B_T^c	M_B Total	Δm_{Bul}	M_B Bulge	Refs. Type	Refs. B_T	Refs. DC,IAC
	(1)	(2)	(3)	(4)	(5)	(6)	(7)	(8)	(9)	(10)	(11)	(12)	(13)	(14)	(15)	(16)
1	NGC 513	SAb	3.0 a	1,2	13.90 b	(0.00)	0.04	0.24	0.21	13.41 b	−22.04 b	−1.54	−20.49 b	5	2	5
2	NGC 1275	Epec	−5.0 c	4,5	12.64 a	−0.04	0.08	0.00	0.75	11.85 a	−23.35 a	0.00	−23.35 c	2,6	2	5
3	NGC 3362	SABc	5.0 a	2,2	13.48 a	0.00	0.05	0.08	0.05	13.31 a	−22.87 a	−2.54	−20.33 a	2	2	5
4	NGC 3982	Sbc,SABb:	3.5 a	2,1	11.86 a	0.00	0.01	0.04	0.00	11.81 a	−20.19 a	−1.74	−18.45 a	6,2	2	5
5	NGC 4117	S0:	−2.3 b	1,3	14.04 a	(0.00)	0.02	0.24	0.00	13.78 a	−19.13 a	−0.57	−18.55 b	2	2	1
6	NGC 4941	SABab,Sab	2.0 a	1,1	11.90 a	0.00	0.01	0.20	0.01	11.68 a	−20.20 a	−1.23	−18.96 a	2,6	2	5
7	NGC 5194	SAbc pec	4.0 a	3,4	8.95 a	0.00	0.00	0.02	0.00	8.93 a	−21.29 a	−1.97	−19.32 a	3	3	1
8	NGC 5347	SBb,SBab pec	2.0 a	1,1	13.40 a	(0.00)	0.02	0.07	0.00	13.30 a	−20.51 a	−1.23	−19.27 a	6,2	2	5
9	NGC 5427	SAc pec	5.0 a	2,5	11.93 a	0.00	0.01	0.05	0.09	11.78 a	−22.07 a	−2.54	−19.53 a	2	2	5
10	NGC 5940	SBab	2.0 b	3,2	14.32 a	−0.10	0.11	0.00	0.10	14.22 a	−22.49 a	−1.23	−21.26 b	2	2	1
11	NGC 5953	SAa: pec	1.0 c	5,3	13.06 a	−0.01	0.02	0.06	0.10	12.88 a	−20.49 a	−1.02	−19.47 c	2	6	7
12	NGC 6104	S?	(1)	4,2	14.21 a	(0.00)	(0.10)	(0.14)	0.00	13.97 a	−22.27 a	(−1.02)	(−21.26)	2	2	1
13	NGC 7672	Sb	3.0 a	2,3	14.70 b	(0.00)	0.03	0.09	0.11	14.47 b	−20.11 b	−1.54	−18.57 b	2	2	5
14	MKN 686	SABa	1.0 b	3,1	13.58 a	−0.03	0.05	0.11	0.00	13.45 a	−21.38 a	−1.02	−20.36 b	5	2	5
15	MKN 917	SBa	1.0 a	1,2	14.60 a	−0.02	0.09	0.02	0.37	14.14 a	−21.74 a	−1.02	−20.73 a	2	2	5
16	ARP 107 A	Sc,S?	(1)	4,5	14.40 b	−0.01	(0.13)	(0.14)	0.03	14.11 b	−22.58 b	(−1.02)	(−21.56)	6,2	4	8,7
17	UGC 3223	SBa	1.0 b	2,1	13.83 a	−0.06	0.06	0.19	0.43	13.21 a	−21.68 a	−1.02	−20.66 b	2	2	1
18	UGC 3995 A	Sc	5.0 b	2,1	13.28 a	(0.00)	0.03	0.25	0.09	12.91 a	−22.08 a	−2.54	−19.54 b	2	2	5
19	UGC 6100	SAab	2.0 a	2,2	14.30 a	(0.00)	0.09	0.13	0.00	14.08 a	−22.24 a	−1.23	−21.01 a	2	2	5
20	3C 120	S0:	−2.0 b	1,1	14.30 a	−0.37	0.15	0.18	0.57	13.78 a	−22.73 a	−0.61	−22.12 b	3	3	1

NOTE.—Follows the format of Table 3 in W92a for additional objects not included in that earlier sample.

Col. (1): Name. Col. (2): Revised Hubble type, following de Vaucouleurs 1959. More than one type given if sources disagree. Col. (3): Hubble stage (T). Col. (4): Disturbance class (DC) and interaction class (IAC). Col. (5): Total magnitude in *B*. Cols. (6)–(9): Magnitude corrections for nuclear nonstellar continuum and emission-line flux (Δm_A), redshift (Δm_K), internal absorption to face-on (Δm_i), and Galactic absorption (Δm_G). Col. (10): Total corrected magnitude in *B*. Col. (11): Total corrected absolute magnitude in *B*, using distances from Table 4, col. (3). Col. (12): Magnitude correction to remove disk light, estimated from col. (3). Col. (13): Bulge absolute magnitude in *B*. Cols. (14)–(16): References to data in cols. (2)–(5). Note that the reference sequence in col. (14) follows the type sequence in col. (2) if more than one type is given. Quality factors (a = good, b = fair, c = poor, r = reject) are defined in more detail in Table 1 of W92a. (*Note:* Luminosities are calculated using $H_0 = 50$ km s^{-1} Mpc^{-1} and $q_0 = 0.0$. Quality factors [a = good, b = fair, c = poor, r = reject] are defined in more detail in Table 1 of W92a.)

REFERENCES.—(1) This paper, from PSS O and/or E prints; (2) de Vaucouleurs et al. 1991 (RC3); (3) de Vaucouleurs et al. 1976 (RC2); (4) Keel et al. 1985; (5) Nelson & Whittle 1995; (6) Sandage & Tammann 1981 (RSA); (7) Whittle 1992a, from Arp 1966; (8) Whittle 1992a, from PSS O and/or E prints.

all, the agreement is good, with mean $\sim -7 \pm 5$ km s^{-1} and rms difference ~ 22 km s^{-1}, confirming the basic integrity of our stellar velocity measurements. Interestingly, there are a few genuinely discrepant points (e.g., NGC 2273) which may indicate unrelaxed H I and/or a dusty nucleus which prevents a clean stellar measurement.

7. SUPPLEMENT TO THE W92a COMPILATION

Since our overall purpose is to explore the importance of the nuclear gravitational potential in Seyfert galaxies, we plan to combine our measurements of stellar kinematics with the W92a compilation of Seyfert host galaxy properties and nuclear active properties. Although many of our sample are found in the W92a compilation, we observed an additional 20 objects whose active and host properties now need to be added as a supplement to the original database. Tables 5, 6, and 7 closely follow Tables 2, 3, and 4 in W92a, and that paper should be consulted for a detailed discussion of the parameters and their quality ratings. Briefly, Table 5 includes Seyfert type (col. [2]); observed H I line width $\Delta V_{\rm H\,I}$ (col. [3]); observed optical major-axis rotation amplitude $\Delta V_{\rm opt}$ (col. [4]); the combination of $\Delta V_{\rm opt}$ and $\Delta V_{\rm H\,I}$, $\Delta V_{\rm rot}$ (col. [5]); the inclination-corrected rotation amplitude $\Delta V_{\rm rot}^c$ (col. [6]); and the inclination i (col. [7]); references are given for H I line width, optical rotation, and inclination (cols. [8], [9], and [10]). Table 6 includes Hubble type, T class, disturbance class (DC), and interaction class (IAC) (cols. [2], [3], and [4]); total blue magnitude, B_T, with corrections for nonstellar light Δm_A, redshift Δm_K, internal absorption Δm_i, and Galactic absorption Δm_G, to give a corrected total magnitude, B_T^c (cols. [5]–[10]); the total absolute blue magnitude, $M_{\rm tot}$, a type-dependent correction to remove the disk contribution, $\Delta m_{\rm bul}$, and the resulting absolute blue magnitude of the bulge, $M_{\rm bul}$ (cols. [11]–[13]); references are given for Hubble type, B_T, DC, and IAC (cols. [14]–[16]). Table 7 includes heliocentric redshift and distance, corrected for Virgocentric flow (cols. [2] and [3]); radio continuum flux and luminosity at 1415 MHz (cols. [4] and [5]); radio morphology: L = linear, D = diffuse, A = ambiguous, U = unresolved, S = slightly resolved (col. [6]); fluxes for [O III] λ5007 and Hβ, and luminosity for [O III] λ5007 (cols. [7]–[9]); references for redshift, radio properties, and emission-line fluxes, including a note of the aperture size, L = large (10″–15″), M = medium (6″–8″), S = small (2″–4″), and other common names (col. [10]–[13]). All distances and luminosities are calculated using $H_0 = 50$ km s^{-1} Mpc^{-1} and $q_0 = 0$.

In Table 8 we present general information on non-Seyfert galaxies for which we have obtained spectroscopic data. These were observed primarily to provide a check on our kinematic

TABLE 7

SEYFERT RADIO AND EMISSION-LINE LUMINOSITIES

	Name	cz_{HC} km s^{-1}	D_{VC} Mpc	S_{1415} mJy	log L_{1415} W Hz^{-1}	Radio Morph	F_{5007} ×10^{-14}	$F_{H\beta}$ ×10^{-14}	log L_{5007} erg s^{-1}	Refs. cz	Refs. S_{1415},R.M.	Refs. (Ap) $F_{5007,H\beta}$	Other Names
	(1)	(2)	(3)	(4)	(5)	(6)	(7)	(8)	(9)	(10)	(11)	(12)	(13)
1	NGC 513	5950	121.3	59 c	23.02	...	...	...	...	7	9	...	AKN 41, U 953
2	NGC 1275	5260	108.4	170 b	23.38	L	50 a	14 b	41.85	7	22	2,1,18 (L)	3C 84, Perseus, A
3	NGC 3362	8320	169.6	11.6 a	22.61	...	6.8 c	0.70 c	41.38	7	10	5 (S)	U 5857
4	NGC 3982	1280 g	25.0	5.1 b	20.58	U	15 c	0.50 c	40.06	21	25	17 (?)	U 6918
5	NGC 4117	1320 g	38.0	2.8 b	20.69	S	...	...	...	21	25	...	U 7112
6	NGC 4941	1110	23.7	14.2 a	20.98	S	22 b	1.3 b	40.17	7	25	23 (M)	...
7	NGC 5194	460 g	11.0	3.6 a	19.72	S	9.4 b	...	39.14	12	11	13 (S)	ARP 85, U 8493
8	NGC 5347	2385	57.6	3.4 c	21.13	U	...	...	...	7	20,25	...	U 8805
9	NGC 5427	2615 p	58.4	2.90 a	21.08	...	7.3 c	0.90 c	40.48	3	14	16 (M)	ARP 271A
10	NGC 5940	10565 g	215.7	8.5 a	22.69	...	3.5 a	9.7 a	41.30	21	10	19 (M)	U 9876
11	NGC 5953	1940 g	47.1	54 a	22.16	L?-D?	8.2 a	2.70 a	40.34	12	4	16 (S)	ARP 91A, U 9903
12	NGC 6104	8380	174.4	...	...	...	...	...	...	7	...	...	U 10309
13	NGC 7672	4045	81.9	7.1 b	21.76	L	...	...	...	15	25	...	MCG 2-59-45
14	MKN 686	4175 g	91.6	1.5 b	21.18	U	12 b	5.1 b	41.09	21	25	8 (L)	N 5695, U 9421
15	MKN 917	7265	148.4	...	...	...	11 b	1.3 b	41.47	7	...	6 (S)	MCG 5-53-9, U 12149
16	ARP 107 A	10425	213.7	<1.5 u	<21.92	...	6.9 b	0.51 b	41.59	7	14	16 (M)	VV 233, MCG 5-26-24
17	UGC 3223	4725	94.1	...	...	...	4.8 b	8.5 b	40.71	7	...	24 (S)	A 0456+04
18	UGC 3995 A	4750	99.0	...	...	...	...	...	...	7	...	...	A 0741+29
19	UGC 6100	8720	180.9	...	...	...	...	...	...	7	...	...	IRAS 10587+4555
20	3C 120	9920	197.2	280 c	24.12	L	38 a	30 bv	42.26	28	26,27	1,18 (L)	II Zw 14, U 3087

NOTE.—Follows the format of Table 4 in W92a for additional objects not included in that earlier sample.

Col. (1): Name. Col. (2): Heliocentric redshift, *cz*, in km s^{-1}. Pair or group redshifts are indicated by "p" or "g." Col. (3): Distance in Mpc using redshift and Virgocentric infall model. Col. (4): 1415 MHz radio flux in mJy. Col. (5): $\log_{10}$ 1415 MHz rest-frame radio luminosity in W Hz^{-1}. Col. (6): Radio morphology: U = unresolved; S = slightly resolved; L = linear; D = diffuse; A = ambiguous. Multiple entries are given if morphology is different on different scales. Cols. (7) and (8): [O III] λ5007 and Hβ emission-line fluxes in ergs s^{-1} cm^{-2} × 10^{-14}. Col. (9): $\log_{10}$ [O III] λ5007 luminosity in ergs s^{-1} using distances from col. (3). No reddening corrections have been applied. Cols. (10)–(12): References for cols. (2)–(8). Aperture size for emission-line fluxes given in col. 12: S = small (2″–4″); M = medium (6″–8″); and L = large (10″–15″). Col. (13): Other common names. (*Note:* Luminosities are calculated using $H_0 = 50$ km s^{-1} Mpc^{-1} and $q_0 = 0.0$ and radio spectral index $\alpha = -0.7$ [$F_\nu \propto \nu^\alpha$]. Quality factors [a = good, b = fair, c = poor, r = reject] are defined in more detail in Table 1 of W92a.)

REFERENCES.—(1) Adams & Weedman 1975; (2) Anderson 1970; (3) Blackman 1982; (4) Condon et al. 1990; (5) Dahari 1985; (6) Dahari & De Robertis 1988; (7) de Vaucouleurs et al. 1991 (RC3); (8) Doroshenko & Terebizh 1981; (9) Dressel & Condon 1978; (10) Edelson 1987; (11) Ford et al. 1985; (12) Geller & Huchra 1983; (13) Goodrich 1989; (14) Hummel, van der Hulst, & Keel 1987; (15) Hutchings 1989; (16) Keel et al. 1985; (17) Kinman 1983; (18) Lacy et al. 1982; (19) Morris & Ward 1988; (20) Neff & Hutchings 1992; (21) Nolthenius 1993; (22) Pedlar et al. 1990; (23) Stauffer 1982; (24) Stirpe 1990; (25) Ulvestad & Wilson 1989; (26) Unger et al. 1987; (27) Walker, Benson, & Unwin 1987; (28) Whittle 1992a.

TABLE 8

BASIC DATA FOR NON-SEYFERT GALAXIES

Name (1)	Activity Class (2)	Type (3)	B_T (4)	M_B (5)	cz_{HC} (km s^{-1}) (6)
NGC 1052	LINER	E4	11.41	−20.90	1507
NGC 2841	LINER	SAb	10.09	−19.61	638
NGC 3031	LINER	SAab	7.89	−20.03	−34
NGC 3998	LINER	SA0	11.61	−20.51	1040
NGC 4339	Normal	E0	12.26	−19.88	1281
NGC 4579	LINER	SABb	10.48	−21.51	1519
NGC 6482	LINER	E:	12.35	−22.82	3922
NGC 6702	Normal	E:	13.23	−22.13	4712
NGC 6703	Normal	SA0$^-$	12.32	−21.85	2365
NGC 7213	LINER	SAa:	11.01	−21.64	1792
NGC 7743	LINER	SB0$^+$	12.38	−20.98	1792
PKS 2152−69	LINER	SA0$^-$	14.3	−21.77	8440

Col. (1): Name. Col. (2): Activity class. Col. (3): Hubble type. Col. (4): Total magnitude in *B*. Col. (5): Total corrected absolute magnitude in *B* using distances estimated from redshifts given in col. (6) or from group velocities (not given) from Nolthenius 1993. Col. (6): Heliocentric redshift *cz*.

technique. The Hubble type, blue apparent magnitude, and redshift (cols. [3], [4], and [6]) were taken from RC3. The absolute magnitude (col. [5]) was calculated in a few cases using distances determined from group velocities (not given).

Overall, our sample data set includes information on a wide range of properties: kinematics of ionized gas in the NLR (Tables 3 and 4); nuclear stellar kinematics (Tables 2 and 4); host galaxy properties such as rotation amplitude, luminosity, morphological type, and inclination (Tables 5 and 6); and active nuclear properties such as NLR [O III] λ5007 luminosity, total (NLR + BLR) Hβ luminosity, radio continuum luminosity, and radio morphology (Table 7). Together these provide a powerful data set with which to study the interdependence of nuclear activity and host properties of Seyfert galaxies.

8. SAMPLE CHARACTERISTICS

Although a more complete analysis will be given in Paper II (Nelson & Whittle 1995), here we give a brief description of our sample properties, compare it with the sample of W92a, and note the principal selection effects.

Our total sample of 85 objects includes 73 Seyfert galaxies, of which 66 yielded usable stellar velocity dispersions. The breakdown by quality for σ_* is 22:30:14:7 for a:b:c:r. A histogram of log FWHM(stars) ($2.35 \times \sigma_*$) is shown in Figure 13*a* for the 66 Seyfert galaxies, with dashed, dotted, and solid lines used to distinguish qualities "a," "b," and "c," respectively. The distribution has a median of 2.51 (323 km s^{-1}) and standard deviation 0.14. For comparison, Figure 13*b* shows the distribution of [O III] FWHM for the same sample, with median 2.47 (296 km s^{-1}) and standard deviation 0.23. The similarity of the medians supports the notion that the gas velocities are principally gravitational, while the broader [O III] distribution is consistent with additional factors, giving both a high line width tail for a few objects and a possible slight shift to lower velocities for the bulk of the sample. The [O III] FWHM distribution for our sample is similar to the W92a sample (median 2.50 = 316 km s^{-1} and standard deviation 0.20).

The distributions of most parameters listed in Tables 5–7 for our sample of 66 Seyfert galaxies are very similar to those of the W92a sample of Seyferts (see Figs. 1–15 and Table 5 in W92a). For example, the distributions of total and bulge absolute magnitudes are essentially identical. There are, however, a few differences, most of which stem from our avoidance of faint host galaxies and strong type 1 Seyferts with difficult spectra (see §§ 2 and 3). For example, the distribution of redshifts

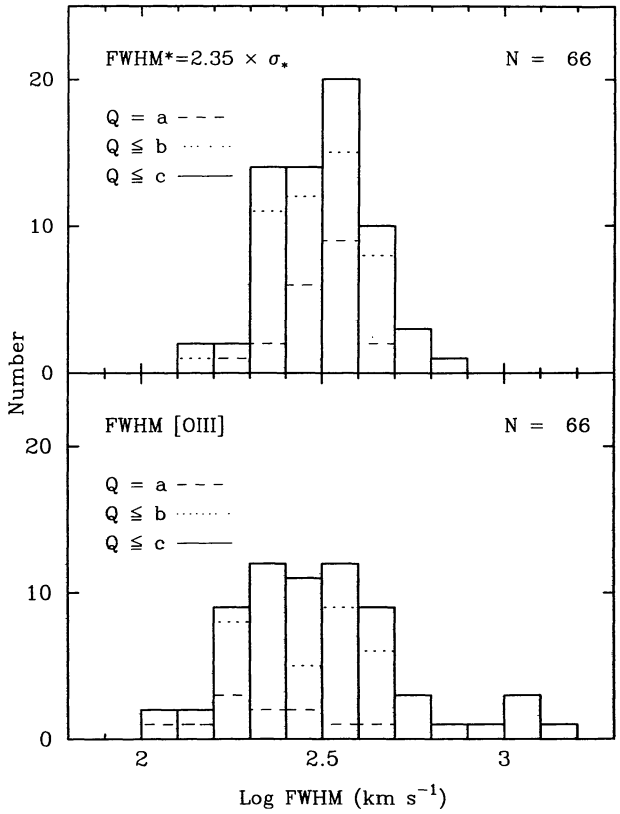

FIG. 13.—Histograms of FWHM$_*$ = 2.35 × σ_* (*top*) and [O III] λ5007 FWHM (*bottom*), plotted for the 66 galaxies with σ_* qualities "c" or better. Data of quality "a," "b," and "c" are represented by the dashed, dotted, and solid lines, respectively. Note the similar means, with somewhat broader distribution and high tail for the emission-line widths.

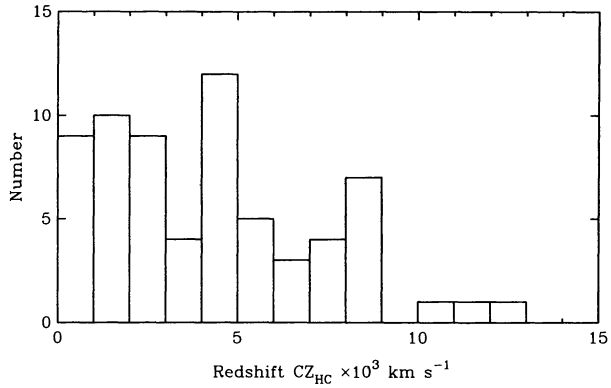

FIG. 14.—Histogram of heliocentric redshift plotted for the 66 galaxies with σ_* qualities "c" or better.

for our sample (Fig. 14) has a somewhat lower median than for W92a (4020 km s^{-1} and 6135 km s^{-1}, respectively). Similarly, our sample has apparently brighter host galaxies (median B_T^c = 13.29 compared with 14.00 for W92a). We again note the change in Seyfert content, with the fraction of Seyfert 1–1.5 galaxies dropping from 48% in W92a to 24% in the present sample. Consequently, properties related to the level of nuclear activity are also changed somewhat, with slightly lower mean values of Hβ and [O III] luminosity, radio luminosity, and nuclear nonthermal corrections to galaxy luminosity.

It is interesting to note the relative ease or difficulty of obtaining stellar kinematic measurements for the Seyfert 1 galaxies in both wavelength regions, given the problems outlined in §§ 2 and 3. For the galaxies we observed, the percentage of type 1 Seyferts (1–1.5) and type 2 Seyferts (1.8–2.5) yielding stellar dispersions of quality a:b:c:r are 5%:25%:30%:40% (type 1 Seyferts, N = 20), 42%:38%:14%:6% (type 2 Seyferts, N = 50). Clearly, even with our tendency to pick "easy" type 1 Seyferts, they still present a more challenging observation than type 2 Seyferts. We also note that it is the Ca II triplet region which has been most helpful in getting the Seyfert 1 dispersions. Of the seven Seyferts with quality "r" for the Mg *b* observation, six are type 1 or 1.5, and, of these, three were recovered using Ca II triplet observations. For this reason, most Seyfert 1 galaxies were observed in the Ca II triplet region.

9. SUMMARY

We have presented in this paper measurements of the stellar velocity dispersions using the cross-correlation method for a large sample of Seyfert galaxies. Two spectral regions were used, centering on the Ca II triplet absorption features in the near-infrared and the Mg *b* absorption lines in the visual. The strong emission lines and featureless continuum emission in these objects create a number of complications for the standard technique. We have also measured widths and redshifts for the [O III] λ5007 and [S III] λ9069 emission lines. We have presented a supplement to the W92a compilation of NLR and host galaxy properties for 20 objects not included in the earlier sample.

The data presented in this paper are the basis for an investigation of the relationship between the gravitational potential and the characteristics of Seyfert galaxies. Our measurements of the stellar and gaseous kinematics will be used in Paper II to address issues relating to the acceleration mechanisms for emission-line gas, the relationship between the active luminosities and the host potential, and the differences between the bulges of Seyferts and normal galaxies.

We would like to thank Matthew Colless and George Efstathiou for providing the basic cross-correlation routines, and Martin Ward for his assistance with the INT observations. We thank the PATT and TAC allocation committees for continuing to support this project, and also the staffs at the AAT, INT, and KPNO for their assistance and support. Thanks also to Richard Gelderman and Richard Patterson for their comments and help with the data reduction and analysis.

APPENDIX
NOTES ON INDIVIDUAL OBJECTS

NGC 513.—We consider the [S III] λ9069 line profile to be unreliable because of atmospheric absorption and noisy data. However, an approximate redshift has been estimated and is given in Table 4.

NGC 788.—[O III] λ4959 was used in preference to [O III] λ5007, which was saturated in the IPCS data.

NGC 1068.—Three Ca II triplet observations were made, two with the KPNO 2.1 m telescope and one with the INT, with modest differences in σ_*: INT, 145 ± 22 km s^{-1} at P.A. 70°; KPNO, 165 ± 12 km s^{-1} at P.A. 75° and 178 ± 16 km s^{-1} at P.A. 140°. The KPNO value at P.A. 75° is given in Table 2, since it has the highest signal-to-noise ratio and is close to the mean of the three measurements.

NGC 1275.—Although the Ca II triplet features in our spectrum are rather noisy and shallow, our value for σ_* agrees reasonably well with the value from Smith, Heckman, & Illingworth (1990) (σ_* = 272 ± 61 km s^{-1} and 246 ± 18 km s^{-1}, respectively).

NGC 1386.—Our Mg *b* value of σ_* = 120 ± 30 km s^{-1} is significantly lower than that of Dressler & Sandage (1983), who measure σ_* = 195 ± 16 km s^{-1} using a similar aperture. Analysis of independent spectra along our slit give consistently low values. Comparing NGC 1386 with NGC 1358 (plotted next to each other in Fig. 3) clearly suggests that NGC 1386 has the narrower lines, and yet we find σ_* = 185 ± 20 km s^{-1} for NGC 1358 (supported by Schechter 1983, σ_* = 161 ± 20 km s^{-1}), which is similar to the Dressler & Sandage value for NGC 1386. We therefore adopt our measurement for σ_* in preference to the value from Dressler & Sandage.

NGC 2273.—The [S III] line was too close to the end of the spectrum to derive an accurate value of C80, particularly with the additional uncertainties introduced by charge transfer errors (see § 3). The profile and widths are otherwise reliable.

NGC 2992.—Our values of σ_* = 168 ± 25 km s^{-1} (Ca II triplet) and σ_* = 155 ± 15 km s^{-1} (Mg *b*) agree well but disagree with σ_* = 108 km s^{-1} from Terlevich et al. (1990). Because this difference is rather large, we choose to adopt the mean of our own values.

NGC 3185.—This object has one of the lowest velocity dispersions in the sample, with σ_* = 61 ± 20 km s^{-1}. This is 62% of the instrumental resolution, which is above the 50% threshold at which systematic errors may be introduced (see § 4.6).

NGC 3227.—The Mg *b* lines are corrupted by [Fe VI] λ5177 and [Fe VII] λ5158. We therefore adopt the Ca II triplet measurement of σ_*.

NGC 3982.—This object has one of the lowest velocity dispersions in the sample, with σ_* = 62 ± 20 km s^{-1}. This is 83% of the instrumental resolution, which is well above the 50% threshold at which systematic errors may be introduced (see § 4.6).

NGC 3998.—This LINER galaxy has the largest value of σ_* (319 km s^{-1}) in the sample.

NGC 4051.—Correction for weak Ca II triplet in emission (see Fig. 3*a*) was required prior to cross-correlation analysis. Since the Mg *b* lines are corrupted by [Fe VI] λ5177 and [Fe VII] λ5158, we adopt the Ca II triplet measurement of σ_*.

NGC 4151.—On nucleus, the Ca II triplet lines are very weak, and to improve their strength we omitted the central spatial channel. Even so, we reject our formally measured value of σ_* = 119 km s^{-1} as too unreliable, and adopt instead the value of σ_* = 178 km s^{-1} from Terlevich et al. (1990). We adopt quality "c" based on comments in private communication (Terlevich 1994).

NGC 4388.—We reject our formally measured value of σ_* = 74 ± 34 km s^{-1} because of noisy data, and adopt instead the value from Terlevich et al. (1990). Terlevich (1994) has indicated that the data are good, and so we adopt quality "b."

NGC 4593.—On nucleus, the Ca II triplet lines are very weak, and to improve their strength we omitted the central spatial channel. The Mg *b* lines are corrupted by [Fe VI] λ5177 and [Fe VII] λ5158, and we therefore adopt the Ca II triplet value for σ_*.

NGC 4941.—The [S III] line was too close to the end of the spectrum to derive an accurate value of C80, particularly with the additional uncertainties introduced by charge transfer errors (see § 3). The profile and widths are otherwise reliable.

NGC 5194.—The wings of the [S III] line were considered unreliable because of the effects of atmospheric absorption bands. Consequently, IPV10 and IPV20 values have not been given in Table 3.

NGC 5347.—The [O III] line is significantly broader than Hβ.

NGC 5548.—The Mg *b* lines are contaminated by [Fe VI] λ5177 and [Fe VII] λ5158, and we therefore reject the value of σ_*.

NGC 6104.—This object is a ring galaxy, with a condensation on the ring. Our observations are of this condensation.

Mrk 3.—A strong, broad [Fe II] λ8617 feature makes measurement of σ_* using the Ca II triplet difficult. Nevertheless, our two independent Ca II triplet spectra give σ_* values which agree well (295 ± 40 km s^{-1} from the KPNO 2.1 m telescope and 276 ± 56 km s^{-1} from INT; we quote the mean in Table 2).

Mrk 6.—Persson (1988) detected the Ca II triplet in emission at $cz = 3000$ km s^{-1} and in absorption at $cz = 5575$ km s^{-1}. Our spectra show the Ca II triplet emission but not the absorption, probably because of our lower quality data.

Mrk 78.—The [O III] emission line is broad and double-peaked. At a redshift of $\sim$11,000 km s^{-1} the Ca II triplet lines lie in the region of strong atmospheric absorption above 8900 Å. In spite of this, we find reasonable agreement between our Ca II triplet and Mg *b* values for σ_* (197 ± 25 and 169 ± 25 km s^{-1}, respectively). Terlevich (1994) has communicated to us an error in their published dispersion value for this object. The corrected value is 150 km s^{-1}. Our adopted value is 172 ± 18 km s^{-1}, close to the Mg *b* measurement.

Mrk 176.—Terlevich et al. (1990) find the stellar redshift to be very different from the emission-line redshift. They suggest that this results from an error in the cross-correlation method arising from the low signal-to-noise ratio in their spectrum (Terlevich 1994). We therefore adopt our Mg *b* velocity dispersion and redshift, $\sigma_* = 202 \pm 22$ km s^{-1} and $cz_* = 7997 \pm 14$ km s^{-1}.

Mrk 348.—Although our Mg *b* and Ca II triplet values of σ_* agree well (117 ± 18 km s^{-1} and 120 ± 22 km s^{-1}, respectively), they differ significantly from the value measured by Terlevich et al. (1990) (185 km s^{-1}). Since their quoted redshift is also $\sim$250 km s^{-1} different from ours (and the [O III] redshift), we chose to adopt the weighted mean of just our own observations.

Mrk 622.—The value for FWHM given in W92a refers, mistakenly, to the Hα, [N II], and [O II] lines, taken from Table 5 of Shuder & Osterbrock (1981). However, Shuder & Osterbrock comment in the text that the [O III] profile is approximately rectangular and much broader, $\sim$1050 km s^{-1}. Our observations confirm these statements and find [O III] FWHM $\sim$ 1160 km s^{-1}. (This error is detailed as a note added in manuscript in W92a.)

Mrk 766.—The Mg *b* lines are contaminated by [Fe VI] λ5177 and [Fe VII] λ5158, and we therefore reject the value of σ_*.

Mrk 1066.—We find that the [O III] and [S III] profiles are rather different. Possible explanations include slightly offset apertures sampling different physical regions or a superposition of regions of different excitation and kinematics.

III Zw 55 N.—Terlevich (1994) has indicated errors of 10%–15%. We therefore assign quality "a."

F341.—[O III] λ4959 was used in preference to [O III] λ5007, which was saturated in the IPCS data.

UGC 6100.—The [O III] emission line is rotationally broadened, and so the measured line widths are given lower quality in Table 3.

REFERENCES

Adams, T. F., & Weedman, D. W. 1975, ApJ, 199, 19
Anderson, K. S. 1970, ApJ, 162, 743
Axon, D. J., Sparks, W. B., Pedlar, A., Unger, S. W., Guerrine, N., Giovanelli, R., & Whittle, D. M. 1995, in preparation
Baldwin, J. A., Carswell, R. F., Wampler, E. J., Smith, H. E., Burbidge, E. M., and Boksenberg, A. 1980, ApJ, 236, 388
Balkowski, C., Bottinelli, L., Gouguenheim, L., & Heidmann, J. 1972, A&A, 21, 303
Bertola, F., Bettoni, D., Rusconi, L., & Sedmak, G. 1984, AJ, 89, 356
Bicay, M. D., & Giovanelli, R. 1986, AJ, 91, 705
Bieging, J. H., & Biermann, P. 1983, AJ, 88, 161
Blackman, C. P. 1982, MNRAS, 200, 407
Boksenberg, A., Shortridge, K., Fosbury, R. A. E., Penston, M. V., & Savage, A. 1975, MNRAS, 172, 285
Bottinelli, L., Gouguenheim, L., Fouqué, P., & Paturel, G. 1990, A&AS, 82, 391
Bushouse, H. A. 1987, ApJ, 320, 49
Busko, I. C., & Steiner, J. E. 1988, MNRAS, 232, 525
Condon, J. J., Helou, G., Sanders, D. B., & Soifer, B. T. 1990, ApJS, 73, 359
Dahari, O. 1985, AJ, 90, 1772
Dahari, O., & De Robertis, M. M. 1988, ApJS, 67, 249
Danziger, I. J., Goss, W. M., & Wellington, K. J. 1981, MNRAS, 196, 845
Davies, R. L., Burstein, D., Dressler, A., Faber, S. M., Lynden-Bell, D., Terlevich, R. J., & Wegner, G. 1987, ApJS, 64, 581
De Robertis, M. M., & Osterbrock, D. E. 1984, ApJ, 286, 171
———. 1986a, ApJ, 301, 98
———. 1986b, ApJ, 301, 727
de Vaucouleurs, G. 1959, in Handbuch der Physik, Vol. 53, ed. S. Flügge (Berlin: Springer), 275
de Vaucouleurs, G., de Vaucouleurs, A., & Corwin, H. G., Jr. 1976, The Second Reference Catalogue of Bright Galaxies (Austin: Univ. Texas Press) (RC2)
de Vaucouleurs, G., de Vaucouleurs, A., Corwin, H. G., Jr., Buta, R. J., Paturel, G., & Fouqué, P. 1991, The Third Reference Catalogue of Bright Galaxies (New York: Springer) (RC3)
Doroshenko, V. T., & Terebizh, V. Yu. 1981, Astrofizika, 17, 667
Dressel, L., & Condon, J. 1978, 36, 531
Dressler, A. 1984, ApJ, 286, 97
Dressler, A., & Sandage, A. 1983, ApJ, 265, 664
Edelson, R. A. 1987, ApJ, 313, 651
Feldman, F. R., Weedman, D. W., Balzano, V. A., & Ramsey, L. W. 1982, ApJ, 256, 427
Filippenko, A. V., & Sargent, W. L. W. 1985, ApJS, 57, 503
———. 1988, ApJ, 339, 134
Fisher, J. R., & Tully, R. B. 1981, ApJS, 47, 139
Ford, H. C., Crane, P. C., Jacoby, G. H., Laurie, D. G., & van der Hulst, J. M. 1985, ApJ, 293, 132
Geller, M. J., & Huchra, J. P. 1983, ApJS, 52, 61
Giovanelli, R., & Haynes, M. P. 1983, AJ, 88, 881
———. 1985, AJ, 90, 2445
Glaspey, J. W., Eilek, J. A., Fahlman, G. G., & Auman, J. R. 1976, ApJ, 203, 335
Goad, J. W., De Veny, J. B., & Goad, L. E. 1979, ApJS, 39, 439
Goodrich, R. W. 1989, ApJ, 340, 190
Heckman, T. M., Balick, B., & Crane, P. C. 1980, A&AS, 40, 295
Heckman, T. M., Balick, B., & Sullivan, W. T., III. 1978, ApJ, 224, 745
Heckman, T. M., Miley, G. K., & Green, R. F. 1984, ApJ, 281, 525
Heckman, T. M., Miley, G. K., van Breugel, W. J. M., & Butcher, H. R. 1981, ApJ, 247, 403
Huchtmeier, W. K. 1982, A&A, 110, 121
Huchtmeier, W. K., & Richter, O.-G. 1989, A General Catalogue of H I Observations of Galaxies (New York: Springer)
Hummel, E., van der Hulst, J. M., & Keel, W. C. 1987, A&AS, 70, 517
Hutchings, J. B. 1989, AJ, 98, 524
Kaneko, N. 1986, A Catalogue of Seyfert Galaxies and Related Objects, unpublished
Keel, W. 1983, ApJ, 269, 466
Keel, W. C., Kennicutt, R. C., Jr., Hummel, E., & van der Hulst, J. M. 1985, AJ, 90, 708
Kinman, T. 1983, MNRAS, 202, 53
Knapp, G. R., van Driel, W., & van Woerden, H. 1985, A&A, 142, 1
Koski, A. T. 1978, ApJ, 223, 56
Lacy, J. H., et al. 1982, ApJ, 256, 75
Laurikainen, E., & Moles, M. 1988, AJ, 96, 470
Malkan, M. A., & Filippenko, A. V. 1983, ApJ, 275, 477
Mirabel, I. F. 1982, ApJ, 260, 75
Mirabel, I. F., & Sanders, D. B. 1988, ApJ, 335, 104
Mirabel, I. F., & Wilson, A. S. 1984, ApJ, 277, 92
Morris, S. L., & Ward, M. J. 1988, MNRAS, 230, 639

Neff, S. G., & Hutchings, J. B. 1992, AJ, 103, 1746
Nelson, C. H., & Whittle, M. 1995, in preparation (Paper II)
Nolthenius, R. 1993, ApJS, 85, 1
Pedlar, A., Ghataure, H. S., Davies, R. D., Harrison, B. A., Perley, R., Crane, P. C., & Unger, S. W. 1990, MNRAS, 246, 477
Persson, S. E. 1988, ApJ, 330, 751
Peterson, S. D. 1979, ApJS, 40, 527
Peterson, S. D., & Shostak, G. S. 1974, AJ, 79, 767
Phillips, M. M., Charles, P. A., & Baldwin, J. A. 1983, ApJ, 266, 485
Rafanelli, P., Osterbrock, D. E., & Pogge, R. W. 1990, AJ, 99, 53
Reif, K., Mebold, U., Goss, W. M., van Woerden, H., & Siegman, B. 1982, A&AS, 50, 451
Sandage, A., & Tammann, G. A. 1981, A Revised Shapley-Ames Catalog of Bright Galaxies (Washington, DC: Carnegie Institution of Washington) (RSA)
Schechter, P. L. 1983, ApJS, 52, 425
Shostak, G. S. 1978, A&A, 68, 321
Shuder, J. M., & Osterbrock, D. E. 1981, ApJ, 250, 55
Simkin, S. M. 1974, A&A, 31, 129
Smith, E. P., Heckman, T. M., & Illingworth, G. D. 1990, ApJ, 356, 399
Stauffer, J. R. 1982, ApJ, 262, 66
Stirpe, G. M. 1990, A&AS, 85, 1049
Sulentic, J. A., & Arp, H. 1983, AJ, 88, 489
Terlevich, E. 1994, private communication
Terlevich, E., Diaz, A. I., & Terlevich, R. 1990, MNRAS, 242, 271
Tonry, J., & Davis, M. 1979, AJ, 84, 1511
Tonry, J., & Davis, M., 1981, ApJ, 246, 666
Ulvestad, J. S., & Wilson, A. S. 1989, ApJ, 343, 659
Unger, S. W., Lawrence, A., Wilson, A. S., Elvis, M., & Wright, A. E. 1987, MNRAS, 228, 521
Unger, S. W., Pedlar, A., Axon, D. J., Harrison, B. A., & Graham, D. A. 1988, MNRAS, 234, 745
van der Kruit, P. C., & Freeman, K. C. 1984, ApJ, 278, 81
Veilleux, S. 1991a, ApJS, 75, 357
———. 1991b, ApJS, 75, 383
Véron-Cetty, M. P., & Véron, P. 1987, ESO Sci. Rep. 5 A Catalogue of Quasars and Active Nuclei (Garching: ESO)
Vrtilek, J. M., & Carleton, N. P. 1985, ApJ, 294, 106
Walker, R. C., Benson, J. M., & Unwin, S. C. 1987, ApJ, 316, 546
White, S. D. M., Huchra, J., Latham, D., & Davis, M. 1983, MNRAS, 203, 701
Whitmore, B. C., & Kirshner, R. P. 1981, ApJ, 250, 43
Whitmore, B. C., McElroy, D. B., & Tonry, J. L. 1985, ApJS, 59, 1
Whittle, M. 1985, MNRAS, 213, 1
———. 1992a, ApJS, 79, 49 (W92a)
———. 1992b, ApJ, 387, 109 (W92b)
———. 1992c, ApJ, 387, 121 (W92c)
Whittle, M., Haniff, C. A., Ward, M. J., Meurs, E. J. A., Pedlar, A., Unger, S. W., Axon, D. J., & Harrison, B. 1986, MNRAS, 222, 189
Whittle, M., Pedlar, A., Meurs, E. J. A., Unger, S. W., Axon, D. J., & Ward, M. J. 1988, ApJ, 326, 125
Williams, B. A., & Rood, H. J. 1987, ApJS, 63, 265